

Geometrical Optimization of Dimpled Double-Pipe Heat Exchangers for Nanofluid-based Natural Circulation Loops Operating at Lower Temperatures

Submitted to the Graduate School of Natural and Applied Sciences
in partial fulfillment of the requirements for the degree of

Doctor of Philosophy

in Mechanical Engineering

by

Nur Çobanoğlu

ORCID 0000-0002-5092-7897

July, 2023

This is to certify that we have read the thesis **Geometrical Optimization of Dimpled Double-Pipe Heat Exchangers for Nanofluid-based Natural Circulation Loops Operating at Lower Temperatures** submitted by **Nur obanođlu**, and it has been judged to be successful, in scope and in quality, at the defense exam and accepted by our jury as a DOCTORAL THESIS.

APPROVED BY:

Advisor: **Assoc. Prof. Dr. Ziya Haktan Karadeniz**
İzmir Kâtip elebi University
İzmir İnstitute of Technology

Committee Members:

Prof. Dr. Alpaslan Turgut
Dokuz Eylül University

Prof. Dr. Orhan Ekren
Cranfield University

Assoc. Prof. Dr. Sercan Acarer
İzmir Kâtip elebi University

Assoc. Prof. Dr. Patrice Estellé
University of Rennes 1

Date of Defense: July 11, 2023

Declaration of Authorship

I, **Nur Çobanoğlu**, declare that this thesis titled **Geometrical Optimization of Dimpled Double-Pipe Heat Exchangers for Nanofluid-based Natural Circulation Loops Operating at Lower Temperatures** and the work presented in it are my own.

I confirm that:

- This work was done wholly or mainly while in candidature for the Doctoral degree at this university.
- Where any part of this thesis has previously been submitted for a degree or any other qualification at this university or any other institution, this has been clearly stated.
- Where I have consulted the published work of others, this is always clearly attributed.
- Where I have quoted from the work of others, the source is always given. This thesis is entirely my own work, with the exception of such quotations.
- I have acknowledged all major sources of assistance.
- Where the thesis is based on work done by myself jointly with others, I have made clear exactly what was done by others and what I have contributed myself.

Date: 11.07.2023

Geometrical Optimization of Dimpled Double-Pipe Heat Exchangers for Nanofluid-based Natural Circulation Loops Operating at Lower Temperatures

Abstract

Excessive use of global energy sources causes negative environmental impacts and a reduction in the available energy resources. Therefore, energy efficiency is the main scope of engineering studies. Since household refrigeration accounts for a large portion of the energy consumption rate in buildings, several innovative techniques have been developed to improve the energy efficiency of vapor compression refrigeration systems. Suction line heat exchangers are considered one of these techniques and they are used to avoid the presence of liquid at the compressor and to prevent sweating on the suction line, as well as increasing enthalpy difference together with superheating the refrigerant at the compressor inlet.

Here, a single-phase natural circulation mini loop (SPNCmL) with double pipe heat exchangers (DPHX) at cooling and heating-ends, has been proposed as an alternative to suction line heat exchangers which requires more attention to control the heat exchange process. Locating DPHXs at the low-pressure side and high-pressure sides of a conventional refrigeration cycle forms a thermal bridge with connecting these by vertical legs of the SPNCmL and provides precise control of the heat transfer with a flexible design.

As a continuation work of an industrial project, in which the performance of a natural circulation loop-assisted deep freezer was evaluated, this study aims to investigate the effect of nanofluid-based SPNCmL using dimpled DPHXs on the performance of the refrigeration cycle. Considering the energy-efficient effects of passive heat transfer improvement techniques and nanofluids on the performance improvement of DPHXs, their combination is aimed to be investigated here. Within this scope, a 3D steady numerical model is used to investigate the performance of SPNCmLs with DPHXs for different geometrical parameters (eccentricity, dimple pitch length, and dimple depth), and thermodynamic analysis of the SPNCmL-assisted refrigeration cycle is conducted by using Engineering Equation Solver (EES).

Utilization of SPNCmL in the refrigeration system results in COP enhancement up to 98% with a reduction of compressor power by 45% if the heating-end is located after condenser (“C-out”, compressor discharge temperature of 70°C, compressor speed of 1200 rpm and low- and high-pressures of 45/450 kPa). However, locating the heating-end before the condenser (“C-in”) at these conditions provides only a 58% enhancement in COP. Moreover, the amount of the maximum transferrable heat is found as 38 W for both “C-out” and “C-in” for the case for both cases of “C-in” and “C-out” at compressor discharge temperature of 70°C, compressor speed of 4500 rpm and low- and high-pressures of 60/600 kPa. At this point, COP improvement is found as 47% and 80% for “C-in” and “C-out”, respectively.

After the preliminary analysis of the system’s main geometry design (pipe diameter of 5.15 mm and AR of 0.8), effects of nanofluids, dimpled surface technology, and eccentricity were investigated individually for the cooling-end which is located at the suction line. Then, the effects of dimples’ height and pitch length as well as eccentricity on the SPNCmL performance have been evaluated for each working fluid. Results of this study show that utilization of dimpled surface technology at the inner pipe of the DPHX decreases the Nusselt number and effectiveness of the SPNCmL. Moreover, as the pitch length decreases which means the number of dimples increases, the Performance Evaluation Criteria (PEC) decreases. However, using nanofluids with lower viscosity values has higher Nusselt numbers and PEC values, but smaller effectiveness. A reduction in eccentricity also decreases the PEC values with pressure drops. The dimples’ height has no significant effect on the pressure drop in SPNCmL

but decreases the PEC values slightly. To conclude, utilization of only nanofluids with lower viscosity values instead of combining them with dimpled surface technology improved the SPNCmLs heat transfer performance, and thus their heat transfer capability in refrigeration systems resulting in higher COP values.

Keywords: Natural Circulation Loops, Nanofluids, Coefficient of Performance, Refrigeration Systems, Dimpled Surface Technology, Geometrical Optimization

Düşük Sıcaklıklarda Çalışan Nanoakışkan Bazlı Doğal Taşınım Döngüleri için Gamzeli Çift Borulu Isı Değiştiricilerin Geometrik Optimizasyonu

ÖZ

Küresel enerji kaynaklarının aşırı kullanımı, olumsuz çevresel etkilere ve mevcut enerji kaynaklarının azalmasına neden olmaktadır. Bu nedenle enerji verimliliği mühendislik çalışmalarının ana konusudur. Ev tipi soğutma, binalardaki enerji tüketim oranının büyük bir kısmını oluşturduğundan, buhar sıkıştırmalı soğutma sistemlerinin enerji verimliliğini artırmak için yenilikçi teknikler geliştirilmiştir. Emiş hattı ısı eşanjörleri bu tekniklerden biri olarak kabul edilmektedir ve kompresör girişinde soğutucu akışkanın aşırı ısınması ile birlikte entalpi farkının artırılmasının yanı sıra kompresörde sıvı bulunmasını önlemek ve emiş hattında terlemeyi önlemek için kullanılmaktadırlar.

Burada, soğutucu ve ısıtıcı uçlarında çift borulu ısı eşanjörlerine (ÇBIE) sahip bir tek fazlı mini doğal taşınım döngüsü (TFmDTD), ısı değişim sürecini kontrol etmek için daha fazla dikkat gerektiren emiş hattı ısı eşanjörlerine alternatif olarak önerilmektedir. ÇBIE'lerin geleneksel soğutma çevriminin düşük ve yüksek basınç hattına yerleştirilmesi ve bunların SPNCmL'nin düşey ayakları ile bağlanması bir ısı köprüsü oluşturmakta ve esnek bir tasarımla ısı transferinin hassas kontrolünü sağlamaktadır.

Doğal taşınım döngüsü destekli bir derin dondurucunun performansının değerlendirildiği endüstriyel bir projenin devamı niteliğindeki bu çalışma, çukurlu ÇBIE'ler kullanan nanoakışkan bazlı TFmDTD'nin soğutma çevrimi performansı üzerindeki etkisini araştırmayı amaçlamaktadır. Pasif ısı transferi iyileştirme teknikleri ve nanoakışkanların ÇBIE'lerin performans iyileştirmesi üzerindeki enerji verimli etkileri dikkate alınarak, bunların kombinasyonunun araştırılması amaçlanmıştır. Bu kapsamda, ÇBIE'li TFmDTD'lerin performansını farklı geometrik parametreler (merkezden kaçıklık, gamze hatvesi uzunluğu ve gamze derinliği) için araştırmak için 3B kararlı sayısal model kullanılmış ve TFmDTD destekli soğutma çevriminin termodinamik analizi Engineering Equation Solver (EES) kullanılarak yapılmıştır.

TFmDTD'nin soğutma sisteminde kullanılması, ısıtıcı ucunun kondenserden sonra yer alması durumunda, kompresör gücünde %45 azalmayla birlikte %98'e kadar COP artışı ("C-out", 70°C kompresör çıkış sıcaklığı, 1200 rpm kompresör hızı ve 45/450 kPa düşük- ve yüksek basınç değerleri) sağlamıştır. Ancak, bu koşullarda ısıtıcı ucunun kondenserden önce yerleştirilmesi ("C-in") COP'de yalnızca %58'lik bir artış sağlamıştır. Ayrıca en yüksek aktarılabilir ısı miktarı hem "C-out" hem de "C-in" için 38 W olarak bulunmuştur (70°C kompresör çıkış sıcaklığı, 4500 rpm kompresör hızı ve 60/600 kPa düşük- ve yüksek basınç değerleri). Bu noktada COP iyileştirmesi "C-in" ve "C-out" için sırasıyla %47 ve %80 olarak bulunmuştur.

Sistemin esas geometri tasarımının ön analizinden sonra (boru çapı 5,15 mm ve AR 0,8), emiş hattında bulunan soğutucu ucu için nanoakışkanların, gamzeli yüzey teknolojisinin ve merkezden kaçıklığın etkileri ayrı ayrı incelenmiştir. Ardından, gamze derinliğinin ve gamze hatvesi uzunluğunun yanı sıra merkezden kaçıklığın TFmDTD performansı üzerindeki etkileri her bir çalışma akışkanı için değerlendirilmiştir. Bu çalışmanın sonuçları, ÇBIE'nin iç borusunda gamzeli yüzey teknolojisi kullanımının Nusselt sayısını ve TFmDTD'nin etkinliğini azalttığını göstermektedir. Ayrıca hatve uzunluğu azaldıkça yani gamze sayısı arttıkça Performans Değerlendirme Kriterleri (PEC) düşmektedir. Bununla birlikte, daha düşük viskozite değerlerine sahip nanoakışkanların kullanılması, daha yüksek Nusselt sayılarına ve PEC değerlerine, ancak daha düşük etkinliğe sahiptir. Merkezden kaçıklıktaki azalma, basınç düşümü ile birlikte PEC değerlerini de düşürmektedir. Gamzelerin derinliğinin basınç düşümü üzerinde önemli bir etkisi yoktur ancak PEC

değerlerini biraz düşürmektedir. Sonuç olarak, gamzeli yüzey teknolojisi ile birleştirmek yerine tek başına daha düşük viskozite değerlerine sahip nanoakışkanların kullanılması, TFmDTD'lerin ısı transfer performansını ve dolayısıyla soğutma sistemlerinde daha yüksek COP değerleri ile sonuçlanan ısı transfer kabiliyetini iyileştirmiştir.

Anahtar Kelimeler: Doğal Taşınım Döngüsü, Nanoakışkan, Performans Katsayısı, Soğutma Sistemleri, Gamzeli Yüzey Teknolojisi, Geometrik Optimizasyon

To my grandmother, M nire obanođlu...

Acknowledgment

Completing this thesis, a product of more than five years' work, I would like to gratefully acknowledge many people who have greatly inspired and supported me during my PhD study at İzmir Kâtip Çelebi University and the writing of this thesis.

First and foremost, I'm deeply indebted to my supervisor, Assoc. Dr. Ziya Haktan Karadeniz, for his endless support, time, patience and encouragement. I am truly motivated by him and his enthusiastic work in many fields, and with this motivation during my PhD, I have had the opportunity to conduct several side projects in which I look forward to continuing to work with him also in the next phase of my career. He has been an amazing supervisor throughout this whole process, I've learned so much from him. I hope to be as inspiring and empathetic a supervisor as he has been to me.

I would also like to extend my deepest gratitude to Prof. Dr. Alpaslan Turgut. In addition to his huge support during my PhD, his guidance has not only helped me to survive in academia but also he has broadened my academic horizons.

I would like to extend my thanks to my committee members, namely, Prof. Dr. Orhan Ekren for his invaluable contributions and support, to Assoc. Dr. Sercan Acarer for his insightful suggestions, and to Assoc. Dr. Patrice Estellé for his constructive advice.

Many special thanks to Priv.-Doz. Dr.-Ing. habil. Matthias H. Buschmann for his support and encouragement during my PhD.

I would also like to thank Assist. Dr. Serkan Doğanay, Alper Mete Genç and Halil Doğacan Koca for their help with my thesis and their friendship.

I would like to express my biggest appreciation to Assoc. Dr. Elif Begüm Elçioğlu for her guidance, all her support and encouragement, and to Prof. Dr. Ömür Şaylıgil for her huge moral support during this journey.

This thesis was carried out in the priority area of “Computational Science and Engineering” within the scope of 100/2000 Doctorate Program by the Council of Higher Education. Therefore, I’m extremely grateful to the Council of Higher Education for their financial support. I’d also like to thank The Scientific and Technological Research Council of Türkiye for its financial support under 2211-A National PhD Scholarship Program. Moreover, I acknowledge that this thesis is a continuation work of TUBİTAK TEYDEB 1505 Project with Grant No: 5180042.

It would be difficult to have reached this point without the consistent emotional support of my friends and family. I feel lucky to have a large group of loved ones to whom I express my appreciation. I cannot name all who have been with me during this process, but I would like to start with my parents, Nurdan Çobanoğlu and Uğur Çobanoğlu, and my brother Can Çobanoğlu. I do not know how to thank them enough for their support, inspiration, and all they have done for me. Many thanks for being always there for me. I also wish to thank my aunt, Aydan Şimşek who is always checking in with me. Last thanks should go to my lovely cats, Juliet-Cotto, Safinaz, Tekir and Sabri for adding meaning to my life in this process.

Table of Contents

Declaration of Authorship	ii
Abstract	iii
Öz	vi
Acknowledgment	x
List of Figures	xv
List of Tables.....	xix
List of Abbreviations.....	xx
List of Symbols	xxii
1 Introduction	1
1.1 Suction Line Heat Exchangers.....	1
1.2 Natural Circulation Loops.....	2
1.2.1 Natural Circulation Loops as Suction Line Heat Exchangers	4
1.3 Double Pipe Heat Exchangers	5
1.4 Aim of This Thesis.....	7
2 Refrigeration Cycle	9
2.1 Thermodynamic Model.....	9
2.2 Performance of SPNCmL Assisted Refrigeration Cycle	12
3 Numerical Model	20
3.1 Numerical Model of SPNCmL	20
3.1.1 Governing Equations	20
3.1.2 Preliminary Study on the Geometrical Parameters of SPNCmL.....	22
3.1.3 Geometry of the SPNCmL	23

3.1.4	Boundary Conditions of the Numerical Model	26
3.1.5	Grid Structure	26
3.1.6	Key Parameters.....	30
3.1.6.1	Eccentricity	30
3.1.6.2	Nanofluids	31
3.1.6.3	Dimpled Surface Technology with Nanofluids	32
3.2	Thermophysical Properties	33
3.3	Mesh Independency	37
3.4	Performance Parameters	37
3.5	Local Heat Transfer Coefficient	41
4	Validation	42
4.1	Validation of the SPNCmL.....	42
4.2	Validation for Natural Convection Heat Transfer	51
4.3	Validation of Eccentric Double Pipe Heat Exchanger.....	53
5	Results and Discussions.....	55
5.1	Results of Preliminary Study	55
5.2	Results of Key Parameters	56
5.2.1	Eccentricity	56
5.2.2	Nanofluids	61
5.2.3	Combination of Dimpled Surface Technology and Nanofluids	71
5.3	Performance of SPNCmL with Dimpled DPHX	82
5.3.1	The Effect of Eccentricity.....	82
5.3.2	The Effect of Dimple Height	91
5.3.3	Local Heat Transfer Performance.....	106
5.3.4	The Overall System Performance.....	109
6	Conclusions	112
	References	114

Appendix	124
Appendix A Publications from the Thesis.....	125
Curriculum Vitae	126

List of Figures

Figure 2.1 Schematic presentation of SPNCmL assisted refrigeration cycle. The heating end of the SPNCmL (a) at condenser inlet (C-in) and (b) condenser outlet (C-out)	10
Figure 2.2 Performance map of (a) “C-in” case [1] and (b) “C-out” case.....	14
Figure 2.3 Comparison of enhancements in COP values for both “C-in” and “C-out” case.....	14
Figure 2.4 Maximum Q_{NCL} values in SPNCmL assisted refrigeration cycle.	15
Figure 2.5 Compressor power consumption of the system as a function discharge temperature [1]	17
Figure 2.6 T-s and P-h diagrams of the SPNCmL assisted refrigeration cycles for (a) “C-in” case and (b) “C-out” case	18
Figure 3.1 Schematic presentation and dimensions of the SPNCmL [1]	23
Figure 3.2 Schematic presentation and dimensions of the SPNCmL with DPHX...	25
Figure 3.3 Design parameters of the SPNCmL with DPHX	26
Figure 3.4 Mesh structure of the system.....	27
Figure 3.5 Mesh distribution in the cooling-end of the SPNCmL for all cases.....	28
Figure 3.6 Mesh distribution in the heating-end of the SPNCmL for all cases.....	29
Figure 3.7 The boundary conditions and dimensions of the annular pipe.....	30
Figure 3.8 The thermophysical properties of base fluid and nanofluids in low temperature [4]	32
Figure 3.9 System schematic and dimensions of the DPHX	33
Figure 3.10 The change of thermophysical properties with temperature.	35
Figure 3.11 Mesh independency analysis for smooth inner piped DPHX working with WEG.....	37
Figure 4.1 Schematic presentation of the SPNCmL in the models and its dimensions in the validation study	43

Figure 4.2	Effect of time step on the solution of the transient 3D model in terms of (a) T_{\max} and (b) ΔT_{heater}	44
Figure 4.3	Effect of heat storage on dynamic behavior of the system in developing flow phase.	46
Figure 4.4	Time dependent variation of Co number for M-Ins model having different mesh numbers and time steps.....	47
Figure 4.5	Effect of Co number on temperatures for different mesh numbers and time steps.....	48
Figure 4.6	Effect of Co number on T^* distributions in the developing flow phase.	49
Figure 4.7	Effect of Co number on V^* distributions in the developing flow phase.	49
Figure 4.8	Validation of M-FF and M-Ins models with experimental results [30] for operating conditions	50
Figure 4.9	Validation of the numerical model on the investigation of the local and average heat transfer coefficients for single-phase and simultaneously developing laminar flow [2].....	51
Figure 4.10	Axial temperature and velocity distributions in the horizontal circular tube for hydrodynamically developed and thermally developing flow [3].....	52
Figure 4.11	The local Nu number along horizontal circular tube representing SPNCmL's heating end.....	53
Figure 4.11	The local Nu number along horizontal circular tube representing SPNCmL's heating end.....	54
Figure 5.1	Preliminary results in terms of (a) ΔT_{heater} , (b) T_{\max} , (c) effectiveness and (d) heat transfer capability (Q [W]).....	56
Figure 5.2	Time dependent heat transfer for different eccentricity values.....	57
Figure 5.3	Axial T^{**} and V^{**} distribution for E0 and E054 cases at $t = 110$ s	58
Figure 5.4	T^{**} distribution in middle cross-section (AA) of the DPHX	59
Figure 5.5	V^{**} distribution in middle cross-section (AA) of the DPHX.....	60
Figure 5.6	The variation of Nu number with Re	61
Figure 5.7	Time dependent variation of heat transfer [4].....	62
Figure 5.8	Cross-sectional T^{**} distributions at the times (a)15 s, (b) 30 s, (c) 45s and (d) 60 s with its (e) legend and the locations.....	63

Figure 5.9 Cross-sectional V^{**} distributions at the times (a)15 s, (b) 30 s, (c) 45s and (d) 60 s with its (e) legend.....	65
Figure 5.10 Axial distributions of the T^{**} and V^{**} along the annular duct.....	68
Figure 5.11 Variation of Nu with Re	70
Figure 5.12 Variation of Δp and PEC with Re (circle and square markers indicate the Δp and PEC respectively.).....	71
Figure 5.13 T^{**} distributions at the critical cross-sections for (a) WEG, (b) WEG+OA+SDS and (c) NF01.....	72
Figure 5.14 V^{**} distributions at the critical cross-sections for (a) WEG, (b) WEG+OA+SDS and (c) NF01.....	75
Figure 5.15 Axial T^{**} and V^{**} distributions for (a) WEG, (b) WEG+AS+SDS, (c) NF01.....	78
Figure 5.16 Pressure drop (Δp) and heat transfer (Nu) characteristics of DPHX.....	81
Figure 5.17 PEC_1 and PEC_2 values of DPHX.....	82
Figure 5.18 The change of temperatures (a) T_{max} and (b) ΔT_{heater} , and (c) effectiveness with number of dimples.....	83
Figure 5.19 The change of Nu with Ra for different eccentricity values for smooth and P10 cases.....	83
Figure 5.20 The axial T^* distribution for (a) WEG, (b) WEG+OA+SDS, (c) NF01.....	85
Figure 5.21 The T^* distribution at cooling-end for different eccentricity values.....	88
Figure 5.22 The T^* distribution at heating-end for different eccentricity values.....	89
Figure 5.23 The axial V^* distribution for (a) WEG, (b) WEG+OA+SDS, (c) NF01.....	91
Figure 5.24 The change of Nu with Re for different eccentricity values for smooth and P10 cases.....	94
Figure 5.25 The change of Nu with Ri for different eccentricity values for smooth and P10 cases.....	94
Figure 5.26 The change of temperatures (a) T_{max} and (b) ΔT_{heater} , and (c) effectiveness with number of dimples for different dimple heights.....	95
Figure 5.27 The change of Nu with Ra for different dimple heights at E054 for smooth and P10 cases.....	96
Figure 5.28 The change of Nu with Ri for different dimple heights at E054 for smooth and P10 cases.....	96

Figure 5.29 The axial T^* distribution of (a) WEG, (b) WEG+OA+SDS, (c) NF01 for different dimple heights	98
Figure 5.30 The axial V^* distribution of (a) WEG, (b) WEG+OA+SDS, (c) NF01 for different dimple heights	101
Figure 5.31 The T^* distribution at cooling-end for different dimple heights.....	104
Figure 5.32 The T^* distribution at heating-end for different dimple heights.....	105
Figure 5.33 Local Nu distribution for different eccentricity values	107
Figure 5.34 Local Nu distribution for different dimple heights	108
Figure 5.35 Local Nu distribution for different working fluids.....	109
Figure 5.35 PEC_2 values for both ends	110

List of Tables

Table 3.1	Main findings of key parameters to investigate the performance of SPNCmL with DPHXs.....	24
Table 3.2	The mesh element numbers of all the cases investigated for SPNCmL..	27
Table 3.3	Coefficients of the polynomials in Equations (3.9-3.13).	36
Table 4.1	Thermophysical properties of Cu pipe and elastomeric rubber as insulation material	45
Table 4.2	Comparison between numerical results and Manglik and Fang [5].....	54
Table 5.1	The Nu and Re numbers for different dimples' heights at cooling- and heating ends.....	97
Table 5.2	The pressure drop and PEC values of all cases.	111

List of Abbreviations

3D	Three-dimensional
AR	Aspect Ratio of SPNCmL
ASHRAE	American Society of Heating, Refrigerating and Air-Conditioning Engineers
C	Cooling-end
CM	Coarse Mesh
COP	Coefficient of Performance
Cu	Copper
DPHX	Double-Pipe Heat Exchanger
EES	Engineering Equation Solver
FM	Fine Mesh
FF	Fluid Flow
GWP	Global Warming Potential
H	Heating-end
HP	High-pressure
IEA	International Energy Agency
L	Loop
LMTD	Logarithmic mean temperature difference
LP	Low-pressure
N	Normalized
NCL	Natural Circulation Loop
NF	Nanofluid
PEC	Performance Evaluation Criteria

PL	Pitch Length
SLHX	Suction-Line Heat Exchanger
SPNCL	Single-Phase Natural Circulation Loop
SPNCmL	Single-Phase Natural Circulation mini Loop
TPNCL	Two-Phase Natural Circulation Loop
WEG	Water-Ethylene Glycol Mixture (50:50)
WEG+OA+SDS	Mixture of Water-Ethylene Glycol (50:50) with Oleic acid and Sodium Dodecyl Sulfonate

List of Symbols

v_{suc}	Specific volume of the refrigerant at the suction-line [m ³ /kg].
η_c	Isentropic efficiency of the compressor
ρ	Density [kg/m ³]
μ	Dynamic viscosity [kg/m s]
δ	Kronecker delta
τ	Stress tensor
ϵ	Aspect ratio of eccentric pipes
ε	Effectiveness
β	Thermal expansion coefficient [1/K]
ϕ	Concentration
A	Area [m ²]
Co	Courant number
c_p	Specific heat at constant pressure [J/kg K]
D	Diameter [m]
e*	Eccentricity
F	Force [N]
g	Gravitational acceleration [m/s ²]
Gr	Grashof number
Gz	Graetz Number
h	Enthalpy [m ² /s ²]
H	Height [m]
k	Thermal conductivity [W/m K]

L	Length [m]
L^+	Dimensionless duct length
\dot{m}	Mass flow rate [kg/s]
N	Rotational speed of the compressor [rpm]
Nu	Nusselt number
p	Pressure [Pa]
PL	Pitch length [m]
Ra	Rayleigh number
Ri	Richardson number
Re	Reynolds number
\dot{Q}_H	Heating capacity [W]
\dot{Q}_L	Cooling capacity [W]
r^*	Pipe diameter ratio
\vec{r}_{ref}	Reference location [m]
Re	Reynolds number
s	Specific entropy [kJ/kg K]
S_M	Source of momentum [kg m ² /s ²]
t	Time [s]
T	Temperature [K]
T^*	Dimensionless temperature for SPNCmL
\mathbf{U}	Velocity vector [m/s]
U	Overall heat transfer coefficient [W/m ² K]
V_{disp}	Displacement volume of the compressor [cm ³]
V	Velocity [m/s]
V^*	Dimensionless velocity for SPNCmL
\dot{W}_{in}	Compressor power [W]

Chapter 1

Introduction

Reduction of global energy resources and negative environmental effects due to the increase in energy demand requires effective use of available energy. Therefore, energy efficiency is becoming the main scope of engineering studies. According to International Energy Agency (IEA) World Energy Outlook 2022, buildings correspond to 30% of final energy consumption in 2021 and household appliances comprise more than half of total electricity consumption already today with an increase of nearly 4% in 2021 [6,7]. As the population grows, the stock of household appliances is also rising. Considering that household energy appliances account for a large share of total household electricity consumption, developing efficient solutions to improve the energy efficiency of household refrigerators is essential [1,8].

However, recent studies reported that household refrigerators have the potential of energy saving by up to 30-40% [9], and global final energy use for residential refrigerators and freezers covered by mandatory minimum energy performance standards is up to 81% in 2021 [10]. With the aim of improving energy efficiency and decreasing energy consumption, variable capacity compressors (VCC) and capacity control [11], vacuum insulation panels (VIP) [12], phase change materials [13], peltier effect systems [14], and suction line heat exchangers or internal heat exchangers [15] are used in the vapor compression systems.

1.1 Suction Line Heat Exchangers

Household refrigerators and freezers are generally equipped with a capillary tube as an expansion device due to its advantages of low cost and simplicity. The capillary tube is generally stuck with the suction line (concentric or lateral configuration) to

avoid the presence of liquid at the compressor and to prevent sweating on the suction line (compressor inlet) [16], as well as increasing enthalpy difference together with superheating the refrigerant at compressor inlet [17]. In addition to this mission of the capillary tube as a part of a counter-flow suction-line heat exchanger (SLHX), it is generally used to control the refrigerant and drops the high pressure of refrigerant in the condenser to the low pressure in the evaporator.

SLHXs can also be used in refrigeration cycles with expansion devices. Here, subcooling with SLHXs can prevent the flash gas formation at the expansion device as well as superheating provides full evaporation of the refrigerant in the suction line before the compression process [15].

However, the interdependence of this process requires more attention to control the heat exchanging and expansion process simultaneously, for the systems with the capillary tube as the expansion device, and only the heat exchanging process for the systems with the expansion device. This would lead to a more complex system design and operation especially if there is a VCC installation on the refrigeration cycle [1]. Therefore, using a heat exchanger with a secondary working fluid could be an alternative way to conduct this process precisely.

1.2 Natural Circulation Loops

Natural circulation loops (NCLs) can be used in refrigeration systems as an alternative to SLHXs. As passive heat transfer systems, NCLs have been used in the energy sector such as solar thermal systems, nuclear reactors and electronic chip cooling applications [18,19].

In NCLs, buoyancy force due to the density difference is the driving mechanism of heat transfer without any external power sources. There are two types of NCLs: Single-phase NCLs (SPNCLs) and Two-phase NCLs (TPNCLs or thermosyphons). Density difference is due to the temperature gradient in SPNCLs while phase-change in TPNCLs [20].

SPNCLs have the advantages of simplicity, reliability, easy control, and enhanced safety compared to TPNCLs [20]. SPNCLs' performance in heat transfer applications

depends on many parameters such as geometry (shape, inclination angle, hot and cold ends' positions, aspect ratio, and pipe diameter), working fluid, and operating conditions also have an impact on SPNCL performance and stability. Recent studies show that miniaturizing the SPNCLs' (mini SPNCLs or SPNCmLs) dimensions also affects system performance and improves stability [21]. Although geometry is considered the primary factor affecting loop performance, the effects of working fluids are widely studied. Water is the most used working fluid, and it is followed by liquid metals and molten salts.

The performance improvement in the heat transfer systems is generally related to thermophysical properties obtained by adding nanoparticles into conventional heat transfer fluids, as introduced as nanofluids [22]. Utilization of nanofluids has improved the performance [23–26] and stability [23,27] of SPNCLs as well as providing a short period of required time to reach a steady state [25]. Moreover, studies on nanofluid-based SPNCmLs have been increasing during the last decade. Misale et al. [28] studied the nanofluid-based SPNCmL for the first time and found that the performance of nanofluids was comparable with base fluid but Turgut and Doganay [29] found that water-based Al_2O_3 nanofluids improved the effectiveness factor which is introduced by them as a thermal performance parameter. They also investigated that effectiveness of the system increases with lower heat sink temperatures and greater inclination angles [30]. The same experimental setup [30] has been also used for the developing numerical model to conduct comparative parametric analyses to predict the performance and characteristics of SPNCmLs [31,32]. The error band of the numerical solution is reported as $\pm 10\%$. Koca et al. [33] found an insignificant change in effectiveness at high concentrations of water-based Ag nanofluids but higher effectiveness for low concentrations at high heater powers. Mohammad et al. [34] showed that water-based CuO nanofluid as a working fluid of SPNCmL increased heat transfer and mass flow rate up to 5.33% and 21.29%, respectively. Nanofluids also may have higher or lower Nusselt numbers in SPNCmLs depending on the applications [35–38]. Çobanoğlu et al. [35] used the SPNCmL as a passive heat transfer system to conduct sensitivity analysis on the definition of the thermophysical properties as measured by experiments and predicted by well-known models. It is found that viscosity has a stronger effect on the SPNCmL characteristics compared to thermal conductivity. Recently, the study [39] investigating the effects of the heater-cooler

orientation on SPNCmL performance reported that SPNCmLs with horizontal heater and cooler had the highest flow rates and Nusselt numbers but a longer time required to start circulation and reach steady-state condition. However, using a vertical heater and cooler had the highest effectiveness values.

1.2.1 Natural Circulation Loops as Suction Line Heat Exchangers

In refrigeration systems, natural circulation loops (NCLs) may be a part of the system or a whole system. Hirano et al. [40,41] applied a thermosyphon in which heat transfer was driven by a temperature difference between a heat exchange section and an evaporator in the refrigeration system. Their system consisted of two cycles: the primary cycle and the heat exchange section. The primary cycle enclosed compressor, condenser, fan motor, expansion valve and heat exchanger unit. In the heat exchange section, the heat exchanger and evaporator were placed. This system has the disadvantage of design flexibility due to the position of the compressor cabinet at the bottom section preventing the buoyancy forces. He et al. [42] benefited from the advantage of cold outdoor temperatures to provide low-cost cooling and improved energy efficiency in their thermosyphon-assisted refrigeration system. It was aimed to decrease the temperature difference between refrigerated space and outdoor ambient temperature by using thermosyphon. The evaporation section of the thermosyphon was located in the refrigerated space and the condenser of the thermosyphon was placed in the climate simulator which was located directly above the refrigerator to simulate outdoor cold temperature conditions. It was found that refrigerated space temperatures could be as low as 4.4°C when outside temperatures were as high as 0.8°C. However, utilization of this system is limited to only cold climate regions. The Sunfrost commercial refrigerator [43], which was developed in the early 1980s, involves heat pipe in the refrigeration cycle. Although the heat transfer device was mentioned as a heat pipe according to product information, actually TPNCL was used for this purpose in the system. Moreover, Garber-Slaght [44] found that utilization of thermosyphon decreases energy consumption by 16% as a result of a comparison between thermosyphon-based refrigeration system and Sunfrost commercial refrigerator.

As mentioned in the literature above, TPNCLs are generally used in refrigerators or freezers. Recently, the potential of SPNCmL as a SLHX in the household freezer was investigated numerically [1]. The heat transfer capability of the SPNCL was studied by a CFD analysis, considering the possible temperature range for the refrigeration cycle and geometrical parameters that affect the loop performance. Additionally, the effect of SPNCL on the performance of the refrigeration cycle was investigated by the performance map for different compressor suction and discharge pressures, discharge temperatures, and different compressor speeds. As a result of this study, SPNCL provides improvement of COP by 11.5% and corresponding energy consumption reduction by 15%.

In this study, a single-phase natural circulation mini loop (SPNCmL) with double pipe heat exchangers at heating and cooling-ends, has been proposed as an alternative to suction line heat exchangers in vapor compression systems. Locating double-pipe heat exchangers (DPHXs) at the low-pressure side and high-pressure sides of a conventional refrigeration cycle does not require any changes in the pipeline. The main pipe of the refrigeration cycle corresponds to the inner pipe of the DPHX and behaves as a heat sink and heat source at low- and high-pressure sides, respectively. The heat transfer between the inner pipe and the secondary heat transfer fluid (working fluid of the SPNCL) is used for subcooling and superheating processes. This also provides a more flexible design of the system compared to conventional SLHX in which heat transfer occurs between the main pipes of refrigeration cycles at the condenser outlet and compressor inlet by internal heat exchangers.

1.3 Double-Pipe Heat Exchangers

Double pipe heat exchangers (DPHXs) are widely used heat transfer systems in industrial applications such as chemical, food, oil, and gas industries [45]. The fact that they consist of two concentric (or eccentric depending on the application) tubes, which exist circular and annular flow characteristics, provides advantages of low cost, simple design and maintenance. Geometrical parameters (eccentricity, pipe diameter, pipe length), operating conditions (thermal boundary conditions) and flow characteristics (fully developed or developing flow) affect the performance of the heat

transfer system [5,46,47]. Additionally, the thermohydraulic performance of the system is also affected by the thermophysical properties of the working fluids.

The heat transfer performance of nanofluids has also been widely used as working fluids in DPHX's annulus or inner tube [4]. The review study on the convection heat transfer in annular passage depicted that nanofluids have higher heat transfer capability due to their thermophysical properties [48]. Subramanian et al. [49] found that utilization of water-based TiO₂ nanofluid in double-pipe counter-flow heat exchanger results in up to 15% heat transfer improvement by increasing concentration and Reynolds numbers. Khanlari et al. [50] obtained 37% and 12% of maximum heat transfer coefficients under turbulent flow conditions for kaolin-deionized water-based counter flow concentric tube and parallel flow concentric tube heat exchangers, respectively. Arya et al. [51] found a heat transfer improvement of 27% in an ethylene glycol-MgO nanofluid-based DPHX but pressure drop increased by 35% for the concentration of 0.3 wt.%. Shahsavar et al. [52] investigated the effect of flow characteristics of hybrid nanofluid (water-based tetramethylammonium hydroxide-coated Fe₃O₄ and gum arabic-coated carbon nanotube hybrid nanofluid) on a counter-current mini channel DPHX. The hybrid nanofluid exhibited a higher heat transfer rate and thus overall heat transfer coefficient and effectiveness in non-Newtonian condition compared to the Newtonian case. Although higher pumping power and pressure drop were obtained in Newtonian condition, it has a higher performance evaluation criterion. A study investigating the impact of nano-sized particles' shape on the thermohydraulic performance of mini channel DPHX reported that platelet-shaped water-ethylene glycol-based boehmite alumina nanofluids had better heat transfer characteristics while spherical-shaped nanofluids demonstrated higher performance index [53]. Within the concept of evaluating metallic nanofluids' (water-based Al₂O₃ and Cu nanofluids) performance in DPHX, higher enhancement in Nu number and a considerable increase in effectiveness were obtained by Cu and Al₂O₃ nanofluids, respectively [54]. Recently, Çobanoğlu et al. [4] have found that the addition of Fe₃O₄ nanoparticles in an ethylene glycol-water (50:50) mixture results in heat transfer improvement up to 13.6% of DPHX in low-temperature applications.

Omidi et al. [45] reported that combining nanofluids with passive heat transfer enhancement techniques in DPHX could be a possible solution for many heat transfer

problems in recent literature. Passive heat transfer improvement techniques (twisted tape inserts, magnetic fields, baffles, and fins) provide an improved heat transfer performance in DPHX by the orientation of flow propagation and changing heat transfer area without consuming any energy [55,56]. Compared to active techniques which include moving parts, passive techniques are cost-effective and more trustworthy. Dimpled surface technology is one of the promising passive heat transfer improvement techniques due to its advantages of low weight, small pressure drop penalty, simple fabrication, and small maintenance costs [57]. The working principle of this technique is based on golf ball aerodynamics since dimples on the golf balls decrease the flow resistance by producing a turbulent boundary layer of air that adheres to the ball's wall [58]. The possible reasons behind convective heat transfer improvement by dimpled surface technology have been explained as flow reattachment, flow impingement, and upwash flow at the downstream region of the dimples [57]. However, flow separation and recirculation in the upstream region of the dimples have been attributed as causes of reduction in heat transfer. The effective Reynolds number range for dimpled surface technology is still in debate in the literature. Garcia et al. [59] found the utilization of dimples more advantageous since it resulted in lower pressure drops at similar heat transfer coefficients compared to wire coils (effective Reynolds number range is 200-2000) for the Reynolds numbers higher than 2000. They also recommended smooth tubes for Reynolds number < 200 . However, Li et al. [60] obtained the best performance for water in the Reynolds number range 500-8000, and it was 150-2000 for the water-glycol mixture at constant heat flux conditions.

1.4 Aim of This Thesis

Considering the growing energy demand for residential refrigerators and freezers, and also their capability to fast response for energy efficient solutions, the performance of SPNCmL as a suction line heat exchanger in refrigeration systems has been investigated in this thesis. As a thermal bridge with a secondary working fluid, the individual performance of the SPNCmLs has a direct effect on the performance of the refrigeration system. The implementation of the SPNCmL to the conventional refrigeration cycle is completed by using DPHXs in both low- and high-pressure sides.

As a continuation work of an industrial project (TÜBİTAK 1505-Project (Grant No: 5180042)), in which the performance of a natural circulation loop-assisted deep freezer was evaluated both experimentally and numerically, this study aims to investigate the effect of nanofluid-based SPNCmL using dimpled DPHXs on the performance of refrigeration cycle. Literature review shows that both dimpled surface technology and nanofluids play important role in the heat transfer improvement of DPHXs, and their combination is aimed to be investigated here. Within this scope, a 3D numerical model is used to investigate DPHX performance under different geometrical parameters (eccentricity, dimple pitch length, and dimple depth), and thermodynamic analysis of the SPNCmL-assisted refrigeration cycle is conducted by Engineering Equation Solver (EES).

Chapter 2

Refrigeration Cycle

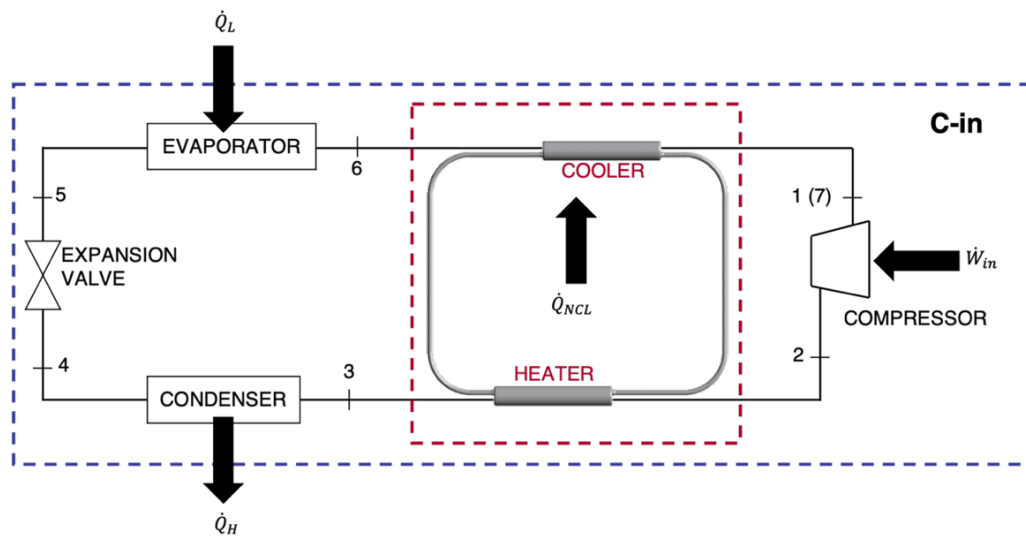
This study aims to understand how the utilization of SPNCmL affects the performance of the refrigeration cycle at the first step. Within this scope, a thermodynamic model was developed by Engineering Equation Solver (EES). Here, details of the thermodynamic model as well as the performance of SPNCmL assisted refrigeration cycle for different working conditions (compressor speeds, compressor discharge temperatures, and low- and high-pressures) have been given.

2.1 Thermodynamic Model

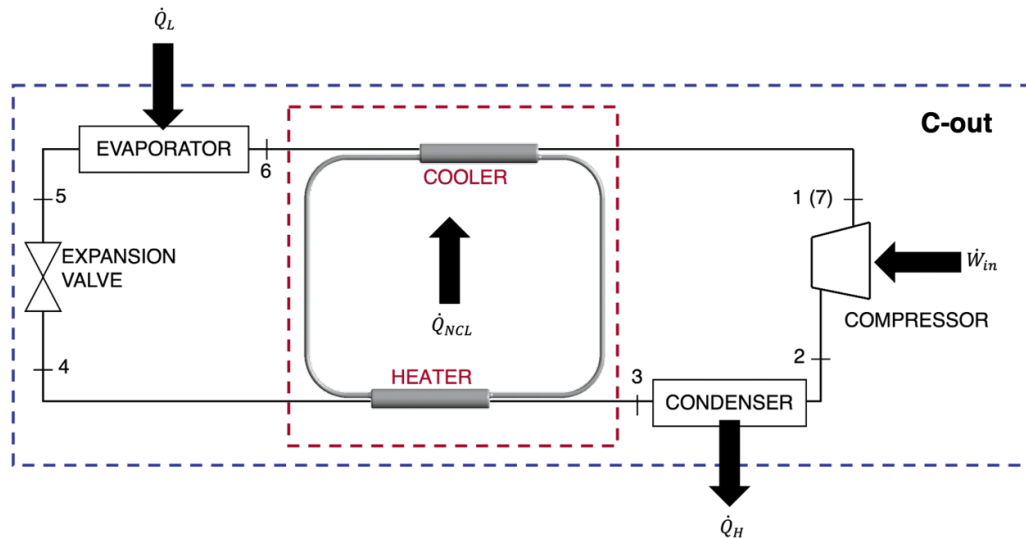
SPNCmL is aimed to be implemented as a suction line heat exchanger between the high- and low-pressure sides of the conventional refrigeration cycle (Figure 2.1). The refrigerant at the outlet of the evaporator is superheated by the cooling-end of the SPNCmL and it is subcooled by the heating-end of the SPNCmL at the high-pressure line. Generally, SLHXs are located between the condenser outlet and evaporator outlet (Figure 2.1.a) in the refrigeration cycle to provide protection for the system components by transferring heat by subcooling the refrigerant at the condenser outlet and superheating at the compressor inlet as well as providing improvement of the system performance. Moreover, this study also investigates the refrigeration cycle performance in the case of locating the heating-end before the condenser as shown in Figure 2.1.b. R600a is used as a working fluid in refrigeration system.

R600a has a very lower global warming potential (GWP) value (GWP:60) when compared to other alternative refrigerants such as hydrofluoroolefin [1]. Furthermore, according to the F-gas regulation fluorinated gases having GWP values higher than 150 have not been allowed in household refrigerators since 2015 in EU (Regulation

(EU) No 517/2014) [61]. Therefore, R600a was chosen as refrigerant here as environmental gas. From an environmental point of view, it is stated that this gas does not damage the ozone layer and contributes to global warming in a virtually negligible manner, and has a remarkable advantage over many other alternatives currently available on the market [62]. In addition to the advantage of higher efficiency (COP) and cost issues, working at low-pressure conditions is another reason behind choosing R600a as a refrigerant.



(a)



(b)

Figure 2.1: Schematic presentation of SPNCmL assisted refrigeration cycle. The heating end of the SPNCmL at (a) condenser inlet (C-in) and (b) condenser outlet (C-out)

The thermodynamic model of the proposed system has been developed by using Engineering Equation Solver (EES) [63]. The cooling performance of the system is calculated by using the energy balance equation shown in Equation (2.1).

$$\Delta\dot{E} = \dot{W}_{in} + \dot{Q}_L - \dot{Q}_H = 0 \quad (2.1)$$

Here, the heating and cooling capacities for R600a used as refrigerant are shown in Equations (2.2) and (2.3), respectively.

$$\dot{Q}_{H,C-in} = \dot{m}(h_3 - h_4); \quad \dot{Q}_{H,C-out} = \dot{m}(h_2 - h_3) \quad (2.2)$$

$$\dot{Q}_L = \dot{m}(h_6 - h_5) \quad (2.3)$$

The inlet power of the system is given by Equation (2.4);

$$\dot{W}_{in} = \dot{m}(h_2 - h_1) \quad (2.4)$$

Here, mass flow rate of the refrigeration system is found by Equation (2.5) [64].

$$\dot{m} = \frac{V_{disp} \cdot N}{60 \cdot v_{suc}} \quad (2.5)$$

Here, V_{disp} is the displacement volume of the compressor [cm^3], N is the rotational speed [rpm] and v_{suc} is the specific volume of refrigerant at the compressor suction [m^3/kg].

The cooling performance is calculated by Equation (2.6),

$$COP = \frac{\dot{Q}_L}{\dot{W}_{in}} \quad (2.6)$$

In order to develop a more realistic model, the compressor discharge temperature (T_2), which is the hottest point in the cycle, is kept constant and the effect of heat transferred by SPNCmL on the overall system efficiency is investigated [1]. The isentropic

efficiency of the compressor for constant discharge temperature is given in Equation (2.7):

$$\eta_c = \frac{h_2 - h_{1s}}{h_2 - h_1} \quad (2.7)$$

Further analysis of the performance mapping of the system is conducted by using a commercially available variable capacity compressor which has 7.2 cm³ of displacement volume and works at the speed range of 1200-4500 rpm [1], and also was used in the experiments conducted within the scope of an industrial project (TÜBİTAK 1505-Project (Grant No:5180042)). The performance of the system has been investigated for the minimum (1200 rpm), medium (2400 rpm) and maximum (4500 rpm) speeds with corresponding power consumptions of 28.2 W, 54.5 W and 105.9 W, respectively.

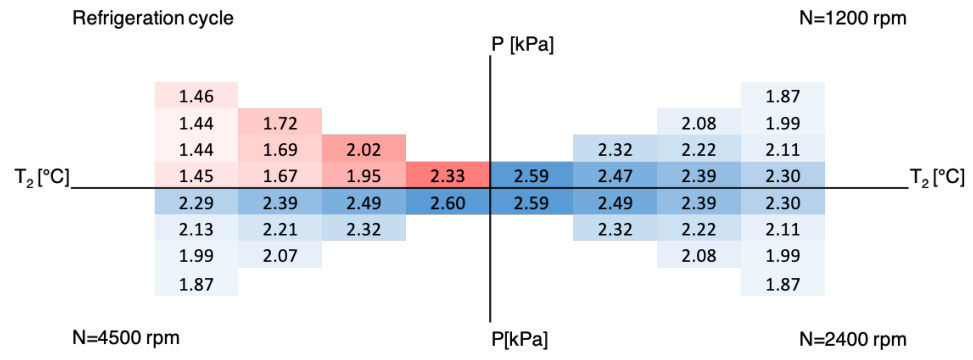
Other assumptions employed in the thermodynamic model are given as followings [1].

- Condenser and evaporator work in the system with 100% efficiency and thus condenser outlet is saturated liquid ($x_4=0$), evaporator outlet is saturated gas ($x_6=1$).
- Expansion valve in the system is isenthalpic ($h_4=h_5$).
- Low and high-side pressures are considered as LP/HP=45/450, 60/600, 75/750 and 90/900 kPa.
- Compressor discharge temperatures are varied in the range of 40-70°C.
- All the COP values are obtained for the closest conditions to the ideal cycle.

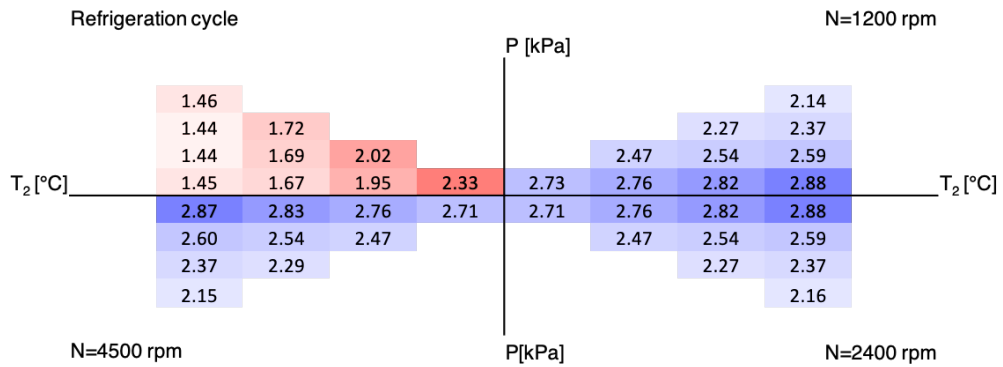
2.2 Performance of SPNCmL Assisted Refrigeration Cycle

The performance map of the SPNCmL-assisted refrigeration cycle presents the COP values of the system for given conditions. The increase of LP/HP in a narrower band

of T_2 and the inability of the system to operate at lower compressor discharge temperatures results in gaps in the performance map for all selected pressure and temperature values (Figure 2.2). In the maps, cells at the center have minimum values of T_2 (40°C) and LP/HP (45/450 kPa), and these values increase further from the center. The reddish area in both maps represents the conventional refrigeration cycle in which COP is independent of compressor speeds at different LP/HP and T_2 . In this section, COP decreases for higher T_2 at constant LP/HP and lower pressures at constant T_2 . The other three quadrants represent the SPNCmL-assisted refrigeration system and compressor speed increases in a clockwise direction. In the “C-in” case, COP drops by the increase of LP/HP and T_2 at constant compressor speeds, and the change of the COP with compressor speed is not significant at constant T_2 and LP/HP [1]. However, an increase of COP with increasing T_2 at constant LP/HP is obtained in the “C-out” case. It is a fact that the utilization of SPNCmL in the refrigeration cycle boosts the COP of the system for both cases. However, the increment in COP is much higher in the “C-out” case compared to the “C-in” case (Figure 2.3). The operating point of LP/HP=45/450 kPa and T_2 =40°C in which conventional refrigeration cycle has maximum COP value, “C-in” case improves the COP by 11% whereas 17% of enhancement is obtained for “C-out” case. Additionally, maximum enhancement is obtained at LP/HP=45/450 kPa and T_2 =70°C by 58% and 98% for “C-in” and “C-out” cases, respectively. Since the enhancement rate and COP value changes with the arrangements, temperature, and pressure ranges, the performance map provides finding an optimum COP value for different operating conditions.



(a)



(b)

Figure 2.2: Performance map of (a) “C-in” case [1] and (b) “C-out” case

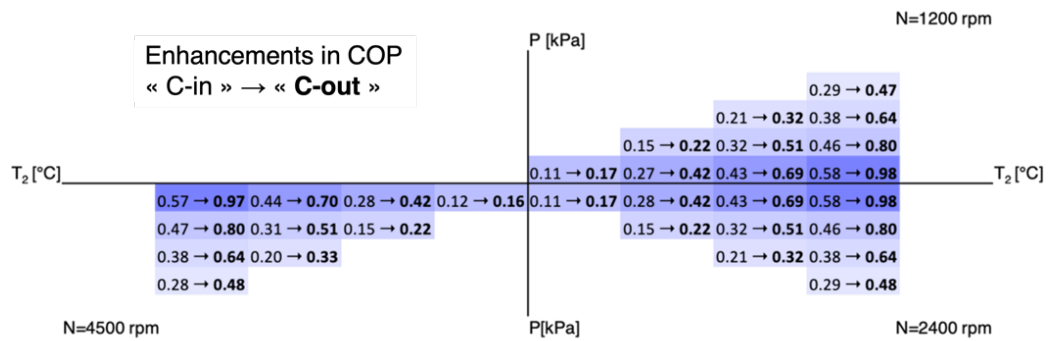


Figure 2.3: Comparison of enhancements in COP values for both “C-in” and “C-out” case

Figure 2.4 presents the maximum heat transfer values of SPNCmL in the refrigeration cycle for different compressor speeds, T_2 and LP/HP values. When the heating-end of SPNCmL is located either before (“C-in” case) or after the condenser (“C-out” case) section, the maximum Q_{NCL} does not change

significantly. Moreover, Q_{NCL} increases with compressor speed N and T_2 at constant LP/HP. The change of Q_{NCL} with LP/HP is not linear. When LP/HP=45/450 kPa and LP/HP=60/600 kPa are compared, Q_{NCL} at LP/HP=45/450 is higher than LP/HP=60/600 kPa for $T_2 = 50^\circ\text{C}$ for all compressor speeds. However, an increase of T_2 to 60°C results in comparable Q_{NCL} values for both LP/HP, and a further increase to $T_2 = 70^\circ\text{C}$ gives rise to higher Q_{NCL} value at LP/HP = 60/600 kPa compared to LP/HP = 45/450 kPa. At constant $T_2 = 70^\circ\text{C}$, an increase of LP/HP decreases the Q_{NCL} values again for all compressor speeds ($T_2 = 70^\circ\text{C}$ and $N=4500$ rpm, $Q_{NCL} = 35.1, 38, 37.6$ and 33.6 W corresponds to LP/HP=45/450, 60/600, 75/750 and 90/900 kPa, respectively).

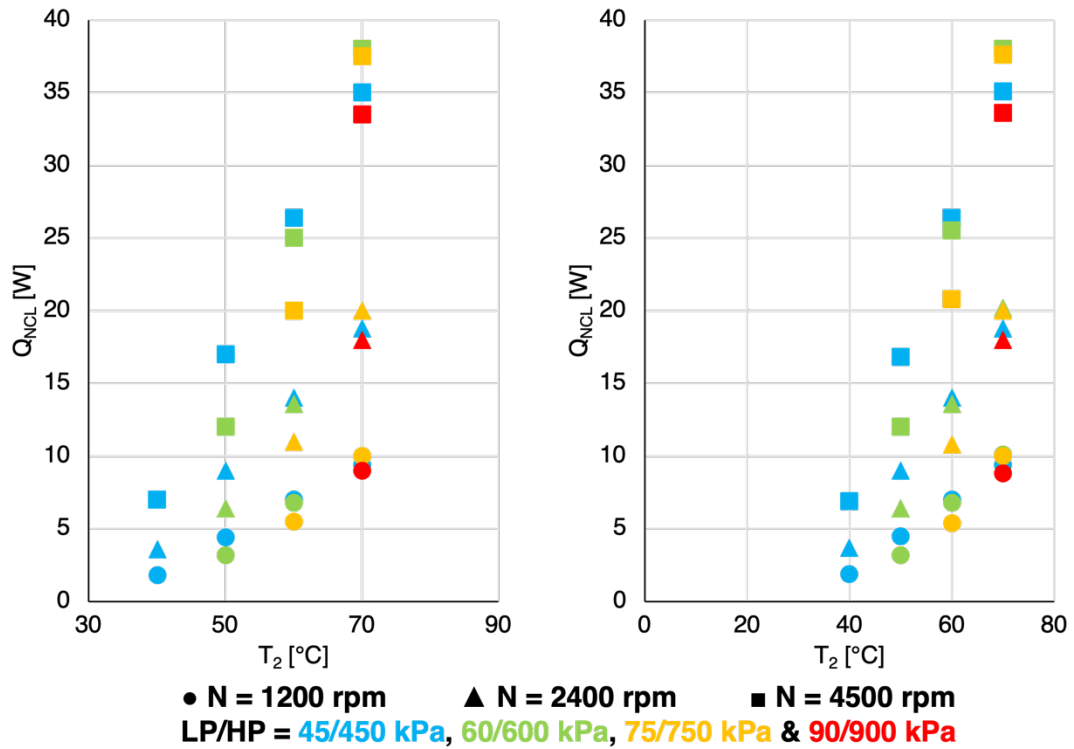


Figure 2.4: Maximum Q_{NCL} values in SPNCmL assisted refrigeration cycle

Moreover, compressor powers obtained from the thermodynamic analyses are compared with the power consumption of the real compressor at different speeds (28.2 W, 54.5 W and 105.9 W for 1200 rpm, 2400 rpm and 4500 rpm, respectively) to evaluate the importance of the thermodynamic analyses performed so far in the

application. Within this scope, Figure 2.5 presents the W_{in} of the conventional refrigeration system at different compressor speeds. Although higher compressor speeds (4500 rpm) cannot achieve the discharge temperatures $T_2 = 60^\circ\text{C}$ and $T_2 = 70^\circ\text{C}$ for conventional refrigeration cycle (No-SPNCmL), assisting the cycle with SPNCmL in both case “C-in” and “C-out” provides a reduction up to 45.5% in the required compressor work to obtain a higher T_2 and eliminates the demand to work with higher compressor speeds. Moreover, there is no significant difference in the results of W_{in} between “C-in” and “C-out” cases. In both orientations, the only condition in which SPNCmL assisted refrigeration system cannot achieve $T_2 = 70^\circ\text{C}$ is at the compressor speed of 4500 rpm and LP/HP = 90/900 kPa. For the condition of maximum COP values (for “C-in” it is $T_2 = 40^\circ\text{C}$, $N=4500$ rpm and LP/HP = 45/450 kPa; for “C-out” it is $T_2 = 70^\circ\text{C}$, $N=1200$ rpm and LP/HP = 45/450 kPa), reduction in W_{in} is equal to 13% and 45% for “C-in” and “C-out”, respectively.

Figure 2.6 presents the T-s and P-h diagrams of the “C-in” and “C-out” cases in which the maximum COP value is obtained (for “C-in” it is $T_2 = 40^\circ\text{C}$, $N=4500$ rpm and LP/HP = 45/450 kPa; for “C-out” it is $T_2 = 70^\circ\text{C}$, $N=1200$ rpm and LP/HP = 45/450 kPa). The expansion of the green line, which corresponds to the conventional refrigeration cycle, as orange lines show the improvement of the performance of the refrigeration cycle as an increase of COP values.

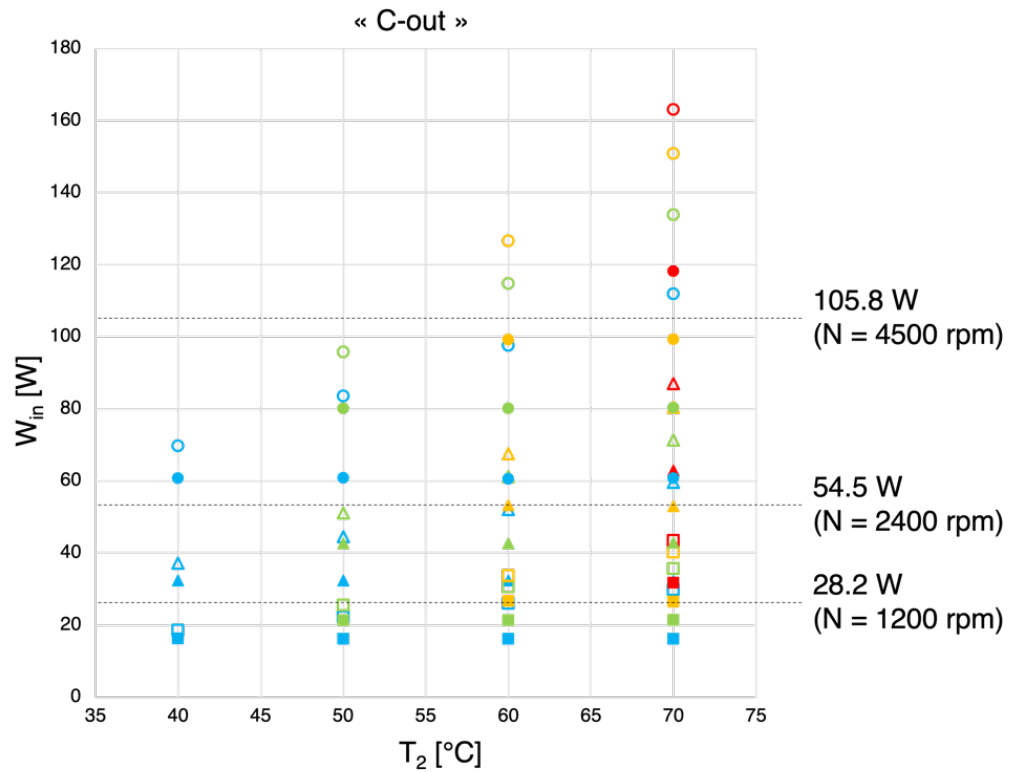
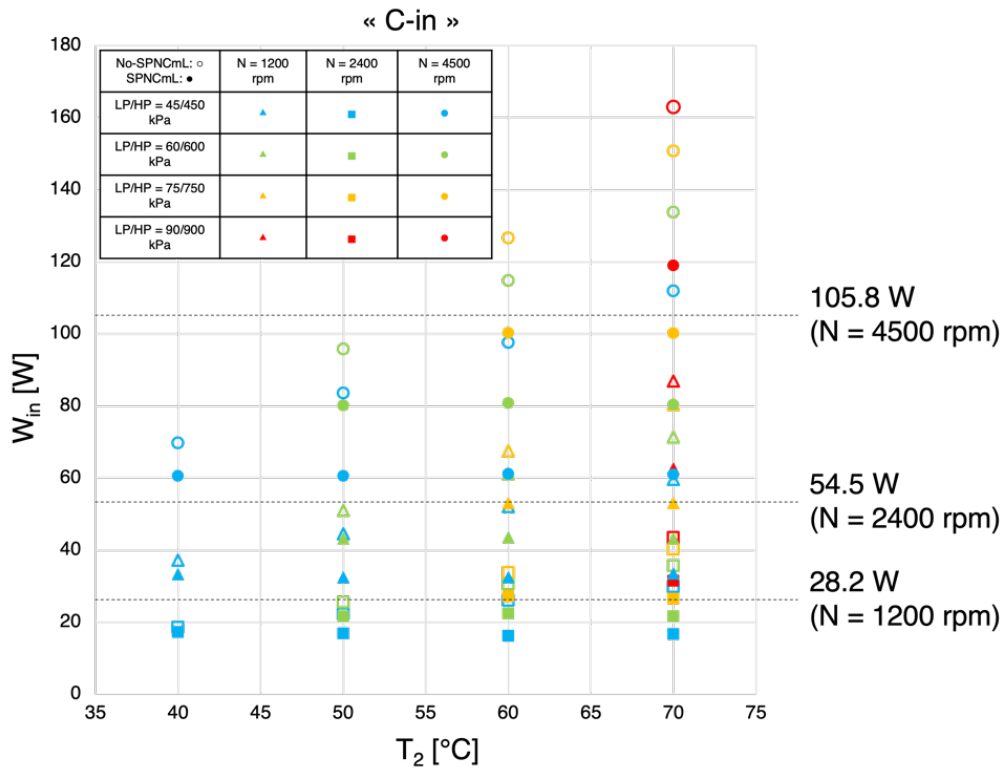
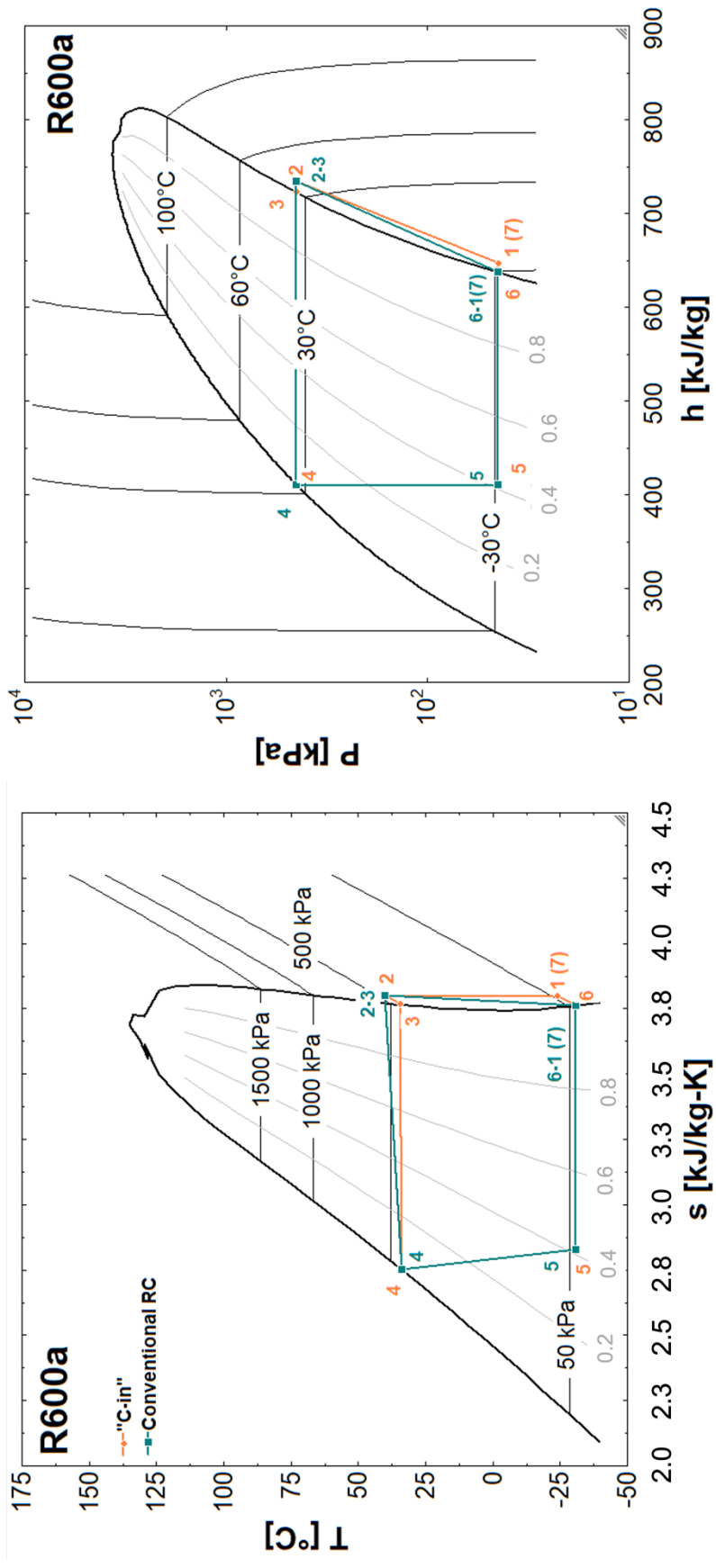
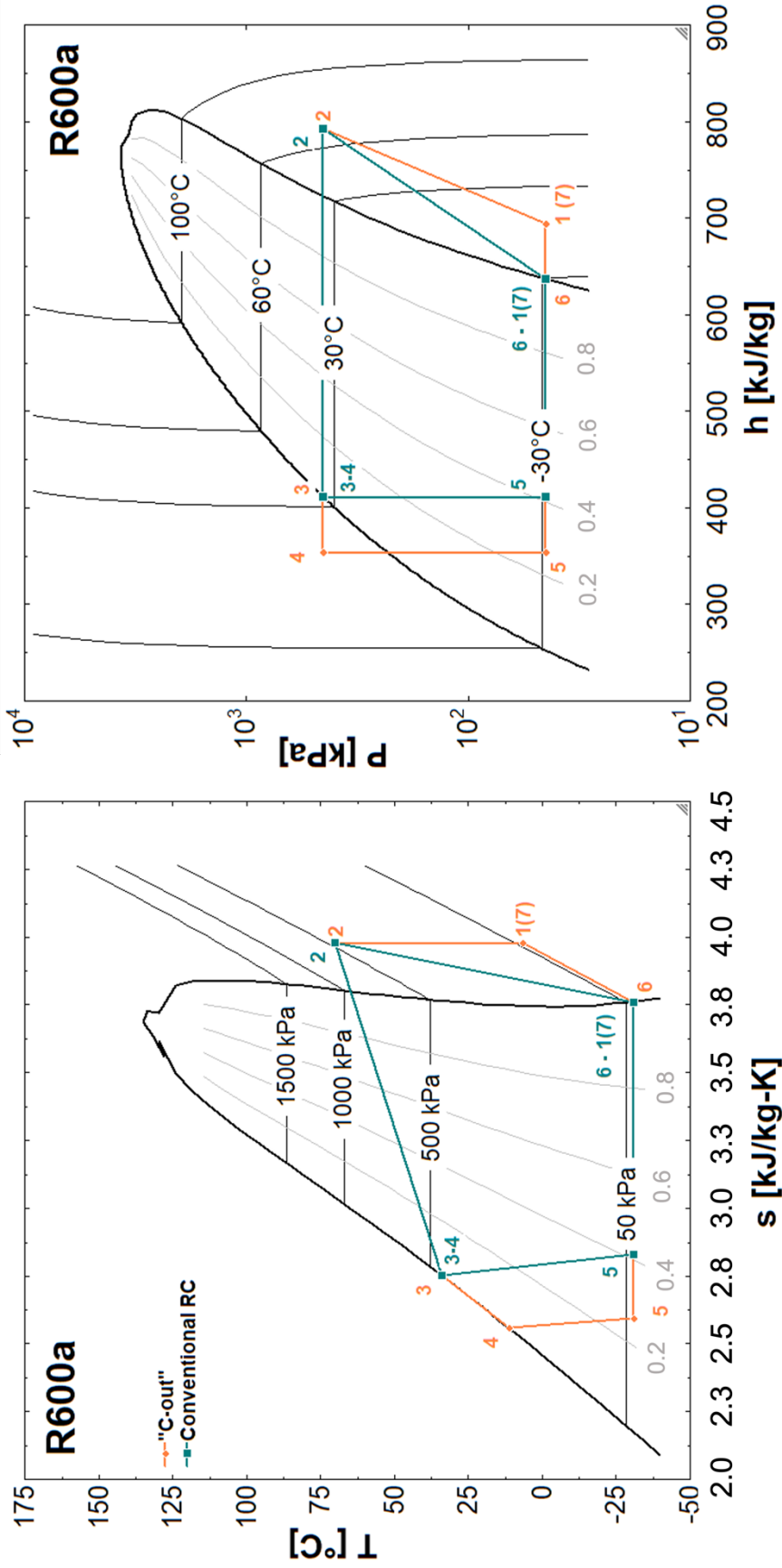


Figure 2.5: Compressor power consumption of the system as a function discharge temperature [1]



(a)

Figure 2.6: T-s and P-h diagrams of the SPNCmL assisted refrigeration cycles for (a) “C-in” case and (b) “C-out” case



(b)

Figure 2.6: (continued)

Chapter 3

Numerical Model

The thermodynamic model of the refrigeration cycle shows that utilization of the SPNCmL results in COP enhancement up to 98% with a reduction of W_{in} by 45% for the case “C-out” ($T_2 = 70^\circ\text{C}$, $N=1200$ rpm and $LP/HP = 45/450$ kPa). Moreover, the amount of the maximum transferrable heat is found as 38 W for the case for both “C-in” and “C-out” at $T_2 = 70^\circ\text{C}$, $N=4500$ rpm and $LP/HP = 60/600$ kPa. Within this scope, in this chapter, the details of the numerical model, which is used to investigate the effect of nanofluid-based SPNCmL using dimpled DPHXs on the performance of the refrigeration cycle, have been given.

3.1 Numerical Model of SPNCmL

3.1.1 Governing Equations

In this thesis, a steady-state 3D numerical model is used to understand how geometrical parameters affect the SPNCmL performance within the scope of the preliminary study and to evaluate how key parameters affect the performance of nanofluid-based SPNCmL using dimpled DPHXs. In order to investigate the heat storage effects for the overall system as well as the initial transient behavior of the heat transfer in SPNCmL’s cooling-end, and flow propagation through the annular section of the DPHX in the low-pressure side, a transient 3D numerical model is used.

Commercial software (ANSYS CFX) was used for building the geometry and solving the numerical model (a steady laminar full buoyancy model with temperature-

dependent thermophysical properties). The general form of the governing equations with the neglect of viscous dissipation can be expressed as [65]:

Mass conservation equation:

$$\frac{\partial \rho}{\partial t} + \nabla \cdot (\rho \mathbf{U}) = 0 \quad (3.1)$$

Momentum equation:

$$\frac{\partial(\rho \mathbf{U})}{\partial t} + \nabla \cdot (\rho \mathbf{U} \otimes \mathbf{U}) = -\nabla p + \nabla \cdot \tau + \mathbf{S}_{M,buoyancy} \quad (3.2)$$

τ is stress tensor and given in Equation (3.3).

$$\tau = \mu \left(\nabla \mathbf{U} + (\nabla \mathbf{U})^T - \frac{2}{3} \delta \nabla \cdot \mathbf{U} \right) \quad (3.3)$$

where μ is viscosity (kg/m s) and δ is the Kronecker delta.

Energy equation:

$$\frac{\partial(\rho h)}{\partial t} + \nabla \cdot (\rho \mathbf{U} h) = \nabla \cdot (k \nabla T) + \mathbf{U} \cdot \nabla p \quad (3.4)$$

The thermal diffusion in the streamwise/axial direction is also neglected in the calculations. In the governing equations, h is enthalpy (m^2/s^2) and \mathbf{U} is velocity vector (m/s). $\mathbf{S}_{M,buoyancy}$ denotes the source of momentum ($\text{kg m}^2/\text{s}^2$). ρ and k are the density (kg/m^3) and thermal conductivity (W/m K) of the fluid, respectively.

The full buoyant method is applied in the numerical method as given in Equation (3.5).

$$\mathbf{S}_{M,buoyancy} = (\rho - \rho_{ref}) g \quad (3.5)$$

Here, ρ_{ref} is the reference density of the working fluid, which is calculated at the average fluid temperature in the system.

The existence of the buoyancy results in hydrostatic gradient due to ρ_{ref} from the pressure in the momentum equation. This is related to absolute pressure as given in Equation 3.6.

$$p_{abs} = p + p_{ref} + \rho_{ref} \vec{g}(\vec{r} - \vec{r}_{ref}) \quad (3.6)$$

Here, \vec{r}_{ref} is the reference location and it is automatically set in the numerical model.

3.1.2 Preliminary Study on the Geometrical Parameters of the SPNCmL

In order to understand the heat transfer potential of a SPNCmL in a possible temperature range for the refrigeration cycle with CFD analysis, a preliminary study is conducted by assuming that SPNCmL has an overall uniform pipe diameter instead of DPHX in cooling- and heating-ends [1]. Different aspect ratios (AR = height/length = H/L) and inner pipe diameters at constant total pipe length (738 mm) of the SPNCmL have been investigated to evaluate the heat transfer potential of the SPNCmL.

The details of the geometry and mesh structure are given in Figure 3.1. The pipe diameters investigated were selected as the pipe diameters currently used by Klimasan Company in the production line within the scope of the TÜBİTAK TEYDEB 1505 Project (Grant No: 5180042). Finer boundary layer elements and mesh structure is employed for the cooling- and heating-ends in comparison with the rest of the system for precise modeling of heat transfer. Convergence criteria was set to 10^{-7} for the governing equations. A constant temperature boundary condition was applied at both cooling- and heating-ends. Since the refrigerant leaves the evaporator as saturated gas ($x_6=1$) evaporator outlet temperature is almost -30°C and the maximum compressor discharge temperature must be 70°C due to the compressor oil limitation, temperatures at the cooling- and heating-ends of the SPNCmL were set to -30°C and 70°C , respectively. In order to drive the natural circulation easily, cooling- and heating-ends are placed in the SPNCmL asymmetrically. The working fluid of the system was a mixture of ethylene glycol (EG) and de-ionized water (DIW) by the ratio of 50:50

(WEG), and its thermophysical properties were introduced as functions of temperatures. Further details are given in Section 3.2.

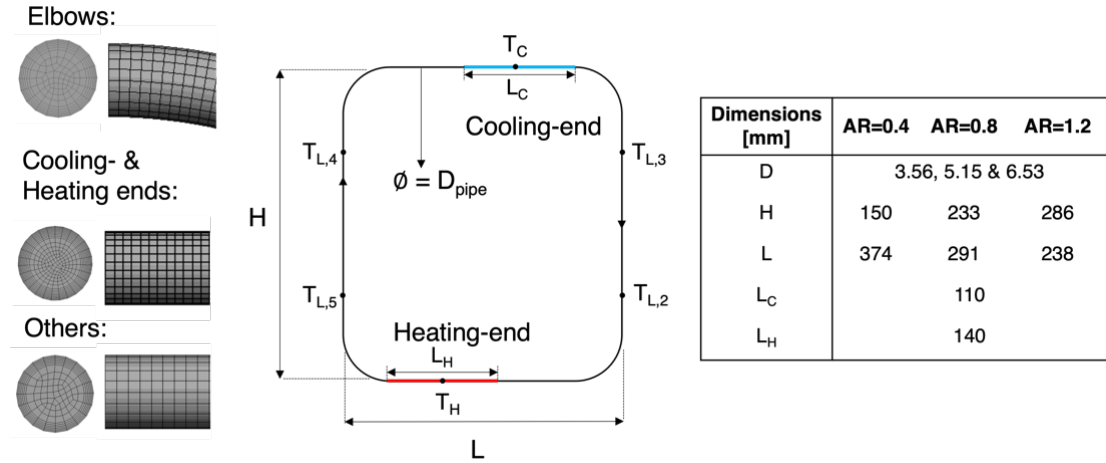


Figure 3.1: Schematic presentation and dimensions of the SPNCmL [1]

Regarding the detailed discussion of the results in the section 5.1, the main geometry is decided to be having pipe diameter of 5.15 mm and AR of 0.8.

3.1.3 Geometry of the SPNCmL

The geometry of the SPNCmL was built by using commercial software ANSYS CFX. The eccentricity of the inner pipe in the DPHX, nanofluids as working fluids, and the dimpled surface technology are the key parameters in this study. Since the main of the SLHXs is superheating the refrigerant at the suction-line, the effects of these key parameters were investigated for only the cooling-end of the SPNCmL. Table 3.1 presents the main findings from the key parameters for selecting the parameters to be investigated to evaluate SPNCmL performance. In Table 3.1, working fluids are ethylene glycol-water mixture (50:50) as WEG, WEG with surfactants (sodium dodecyl sulfonate (SDS) and oleic acid (OA) as WEG+OA+SDS; nanofluids at low concentration of 0.01, 0.05 and 0.1 vol.% are denoted as NF001, N005 and NF01, respectively. Further information about the modeling of key parameters is given in section 3.1.6 and results are presented in section 5.2.

Section 5.2.3 presents the effect of combination of dimpled surface technology and nanofluids on heat transfer performance of DPHX. It is found that dimples behave as thermohydraulic cells which capture and trap the flowing working fluid which leads higher Δp . Therefore, the height of the dimples is critical in this case. Within this scope, the effect of the dimple height diameter is also investigated.

Table 3.1: Main findings of key parameters to investigate the performance of SPNCmL with DPHXs

Key parameters	# of parameters					Comments
	1	2	3	4	5	
Eccentricity	0.32	0.39	0.54	0.61	0.69	Increase in eccentricity results in reduction of transferred heat
Working Fluids	WEG	WEG+OA+SDS	NF001	NF005	NF01	NF01 has the highest Nusselt number and heat transfer capability.
Dimples' Pitch Length [mm]	10	20	30			Pitch lengths defines the number of the dimples and thus heat transfer area.
Dimples' Diameter [mm]	0.2575	0.515	1.03			Regardless of the diameter, dimples behave as thermohydraulic cells which capture and trap the flowing working fluid.
Dimples' Height [mm]	0.35	0.50				See Section 5.3.

The main geometry of the SPNCmL and its dimensions are introduced in Figure 3.2. Similar to preliminary analysis, cooling- and heating-ends are located in the SPNCmL asymmetrically for easy start of the natural circulation. Considering the effect of buoyancy forces and thus natural convection, the inner pipe was located in the upper position of the DPHX at the low-pressure side, and it is located at the bottom position of the DPHX for the high-pressure side. The design parameters (dimples' pitch length, dimple height and eccentricity) are given in Figure 3.3. The effect of dimples' height at the constant eccentricity of 0.54 is investigated for all working fluids and pitch length. Moreover, the effect of the eccentricity on the SPNCmL performance is studied at constant dimples' height of 0.35 mm for all working fluids and pitch lengths.

From this chapter, all the cases investigated within this scope are denominated with their eccentricity, dimples' height and pitch length in order, for instance, E032-H035P10 for the case with the eccentricity of 0.32 and with dimple height of 0.35 mm and pitch length of 10 mm.

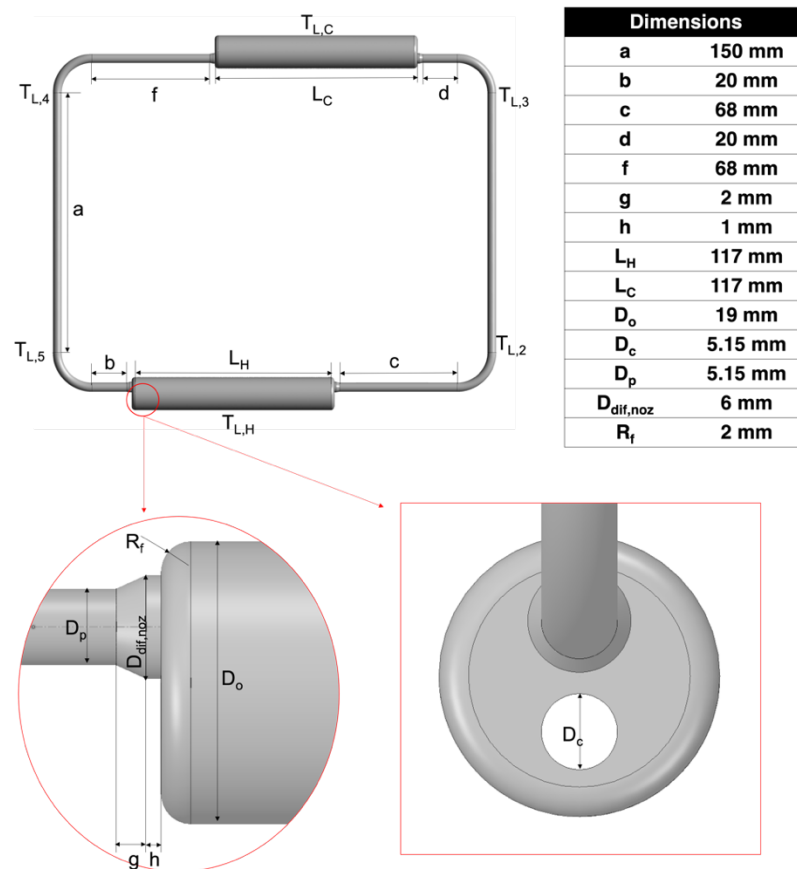


Figure 3.2: Schematic presentation and dimensions of the SPNCmL with DPHX

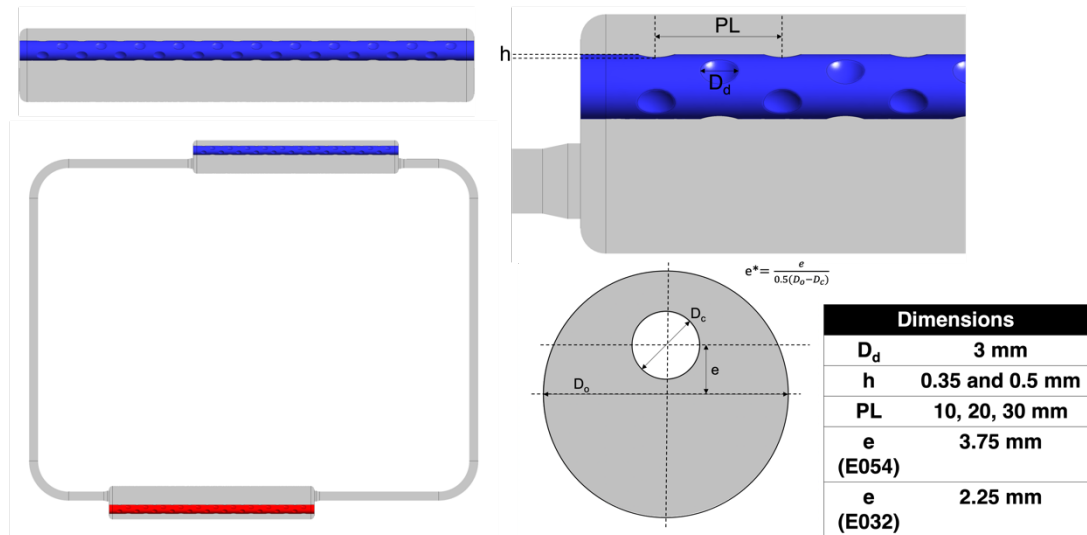


Figure 3.3: Design parameters of the SPNCmL with DPHX

3.1.4 Boundary Conditions of the Numerical Model

The inner tubes of the DPHXs are the main pipes of the refrigeration system through which R600a flows. Therefore, constant temperature boundary conditions were applied to both cooling- and heating-ends which have been located on low- and high-pressure sides of the refrigeration cycle. $T_C = 253.15$ K and $T_H = 333.15$ K were set to develop a precise simulation considering heat losses of the real conditions in which the evaporating temperature equals 247.15 K, and the maximum compressor discharge temperature must be 343.15 K due to the compressor oil limitation.

3.1.5 Grid Structure

In order to reduce computational costs, the mesh structure is generated by using finer meshes in the DPHXs and coarser meshes for the rest of the system as presented in Figure 3.4. The combination of tri and quad meshes was generated in the DPHXs in both cooling- and heating-ends, whereas quad meshes were used for all the remaining parts.

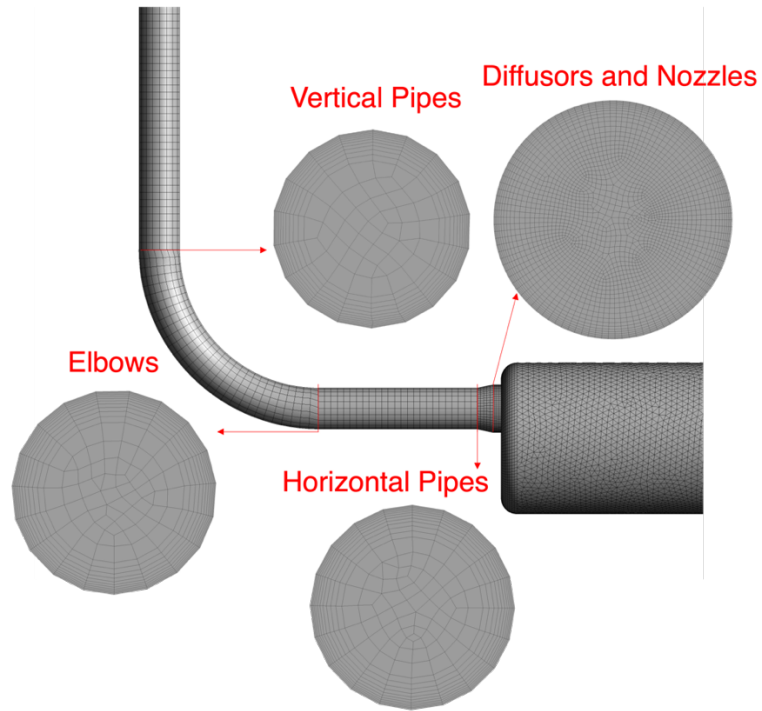
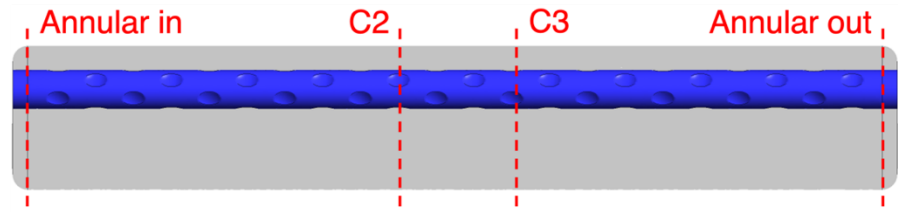


Figure 3.4: Mesh structure of the system

Since the design parameters (dimples' pitch length, dimples' height and also eccentricity) change the geometry, the mesh element number, as well as the mesh structure, changes with all cases. Table 3.2 presents the mesh element numbers for all cases, and the mesh structure of DPHXs in both cooling- and heating-ends is given in Figures 3.5 and 3.6. The element numbers are tried to be kept in the same order of magnitude.

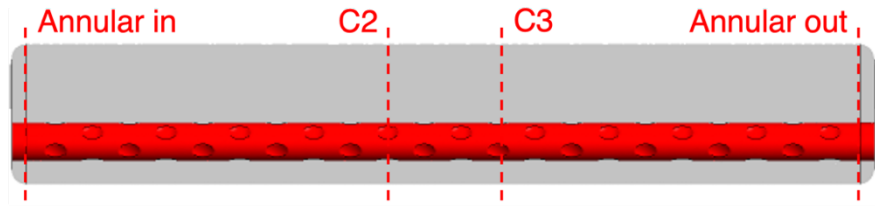
Table 3.2: The mesh element numbers of all the cases investigated for SPNCmL

Cases	E032-H035	E054-H035	E054-H050
smooth	1915129	2246965	
P10	3544746	3743593	3858304
P20	2771488	3034403	3079872
P30	2532625	2828138	2858529



Cooling-end	Annular In	C2	C3	Annular Out
E032 - Smooth				
E032 - H035P10				
E054 - Smooth				
E054 - H035P10				
E054 - H035P10				

Figure 3.5: Mesh distribution in the cooling-end of the SPNCmL for all cases.



Heating-end	Annular In	C2	C3	Annular Out
E032 - Smooth				
E032 - H035P10				
E054 - Smooth				
E054 - H035P10				
E054 - H035P10				

Figure 3.6: Mesh distribution in the heating-end of the SPNCmL for all cases.

As aforementioned in the previous paragraph, the changing geometry with design parameters changes the mesh structure and thus element numbers. Therefore, the mesh independency analysis was conducted for only the cooling-end of the SPNCmL which is located at the suction-line to superheat the refrigerant before the condenser inlet. The details are given in section 3.3.

3.1.6 Key Parameters

3.1.6.1 Eccentricity

Since flow tends to stagnate at narrower section and has maximum velocity values in wider sections [5,46,47], eccentricity has a crucial impact on flow propagation and temperature distribution in DPHXs. The effect of eccentricity on the DPHX performance for 0, 0.32, 0.39, 0.54, 0.61, 0.6,9 and 1 of eccentricity (e^*) values at the pipe diameter ratio (ratio of the inner pipe diameter to outer pipe diameter) 0.27. In the numerical model, the cases of $e^* = 0.32-0.69$ have blended with a radius of 2 mm at the inlet and outlet of the annular section. However, these blends were removed to satisfy similar inlet and outlet conditions (upstream and downstream pipes) for fully concentric and eccentric cases of $e^* = 0$ and $e^* = 1$, respectively.

In the DPHX system, the pipes through which the refrigerant passes are modeled as inner pipe at constant temperature boundary conditions ($T_C = -20^\circ\text{C}$) and at the upper region of the annuli to obtain a positive effect on the heat transfer and flow progression as shown in Figure 3.7. Considering the limitation on the freezing point of water, an ethylene glycol-water mixture (WEG) is generally used in low-temperature applications. The WEG enters the annuli with the inlet velocity $V_{in} = 0.1582$ m/s (average velocity at the value at cooling-end inlet in SPNCL design of [8]) at $T_{in} = 20^\circ\text{C}$ for 200 s with a time step of 0.05 s. Here, the thermophysical properties of the WEG (50:50) were taken from the ASHRAE [66] and introduced to the numerical model as a function of temperature.

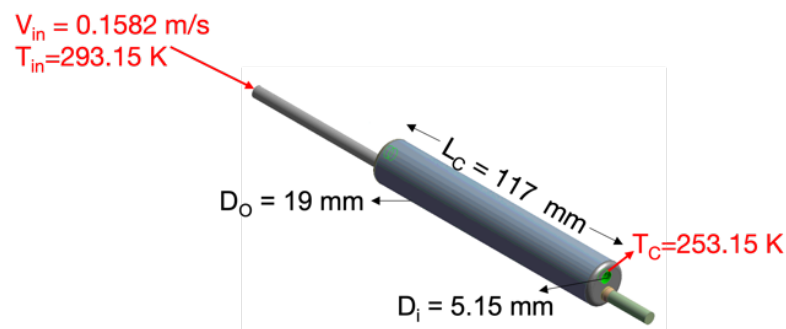


Figure 3.7: The boundary conditions and dimensions of the annular pipe

3.1.6.2 Nanofluids

In low-temperature applications, such as refrigeration systems, water-ethylene glycol mixture (WEG) is used as the working fluid of the DPHXs to improve heat transfer considering the freezing temperature limitation of water. Recently, Banisharif et al. [67] studied the thermophysical properties of WEG (50:50) based Fe_3O_4 nanofluids at low concentrations (0.01, 0.05 and 0.1 vol.%) and temperatures (253.15-293.15 K). It is found that an increase in nanoparticle concentration resulted in higher thermal conductivity and lower viscosity values which would affect the heat transfer enhancement in passive systems positively.

Considering the lower viscosity values in the passive heat transfer systems, this study investigates the potential of WEG-based nanofluids in the low-pressure side of the refrigeration system. In the proposed system, the nanofluids in the annular section are considered as secondary fluid for superheating the refrigerant which flows through the inner pipe of the DPHX.

The exact same geometry was used in the numerical model with $e^* = 0.54$ and $r^* = 0.27$. The refrigerant which has been supposed to flow through the inner pipe of the duct was introduced to the system by employing lower constant temperature boundary condition ($T_C = 253.15$ K) at the inner pipe as shown in Figure 2. The primary working fluid flows through the annuli with the inlet velocity $V_{in} = 0.1582$ m/s at $T_{in} = 293.15$ K for 250 s with a time step of 0.05 s. The inlet velocity is determined by the average velocity value at the cooling-end inlet in SPNCL [1].

Banisharif et al. [67] used a mixture of WEG (50:50) as a base fluid at 293.15 K with the amount of 0.2 wt.% in sodium dodecyl sulfonate (SDS) and 0.2 vol.% in oleic acid (OA) to disperse and stabilize Fe_3O_4 nanoparticles. WEG, WEG+OA+SDS and Fe_3O_4 nanofluid (0.01, 0.05 and 0.1 vol.%) were used as working fluids in this parametric study. The thermophysical properties, namely thermal conductivity, heat capacity, dynamic viscosity and density, presented in [67] were introduced to the numerical model as polynomials which are functions of temperature. The full description of nanofluid preparation and characterization, as well as discussion of the results, can be found in ref [67]. Besides these experimental data [67], the effective thermal expansion coefficient (β_e) of the working fluids was calculated by mixture rule (Further details

for thermal expansion coefficient are given in section 3.2 and the reference [4]). The variation of thermophysical properties with temperature and nanoparticle content is presented in Figure 3.8.

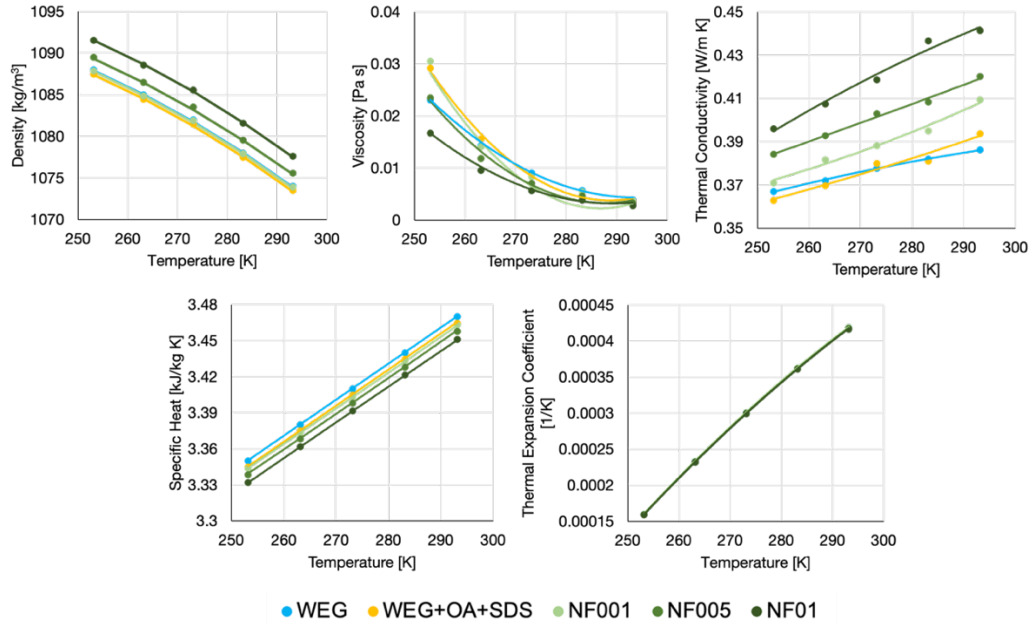


Figure 3.8: The thermophysical properties of base fluid and nanofluids in low temperature [4]

3.1.6.3 Dimpled surface technology with nanofluids

This study aims to investigate the heat transfer performance of nanofluid in the annular section of DPHXs with the inner dimpled tube for the low-pressure side of the refrigeration cycle. Considering the effect of buoyancy forces and thus natural convection, the inner pipe was located in the upper position of the annular tube. The system geometry and its dimensions are given in Figure 3.9. Three different spherical dimple diameters and three different pitch lengths were employed onto the inner pipe surface. The dimples' diameter was calculated by the dimple pipe diameter ratio ($DP = D_{dimple}/D_{in}$, $DP = 0.05, 0.1$ and 0.2). The pitch length, which is the horizontal distance between the dimples' centers, was studied for 10, 20 and 30 mm. For dimpled cases, the center of the spherical dimpled is located at the outer surface (the interface between the inner pipe and annular section) of the inner pipe and thus the height of the

dimple varies with the DP . A constant temperature boundary condition ($T_c=253.15$ K) was employed at the inner pipe and the working fluid flows through the annuli with $Re_{in}=500$ where $Re_{in} = \frac{\rho_{in} V_{in} D_p}{\mu_{in}}$ at $T_{in}=293.15$ K for 200 s with a time step of 0.1 s. All the cases are solved for laminar flow due to the Re_{in} . The thermophysical properties of the WEG, WEG+OA+SDS and NF01 are introduced in the numerical model as a function of temperatures which is valid in the temperature range from 253.15 K to 293.15 K.

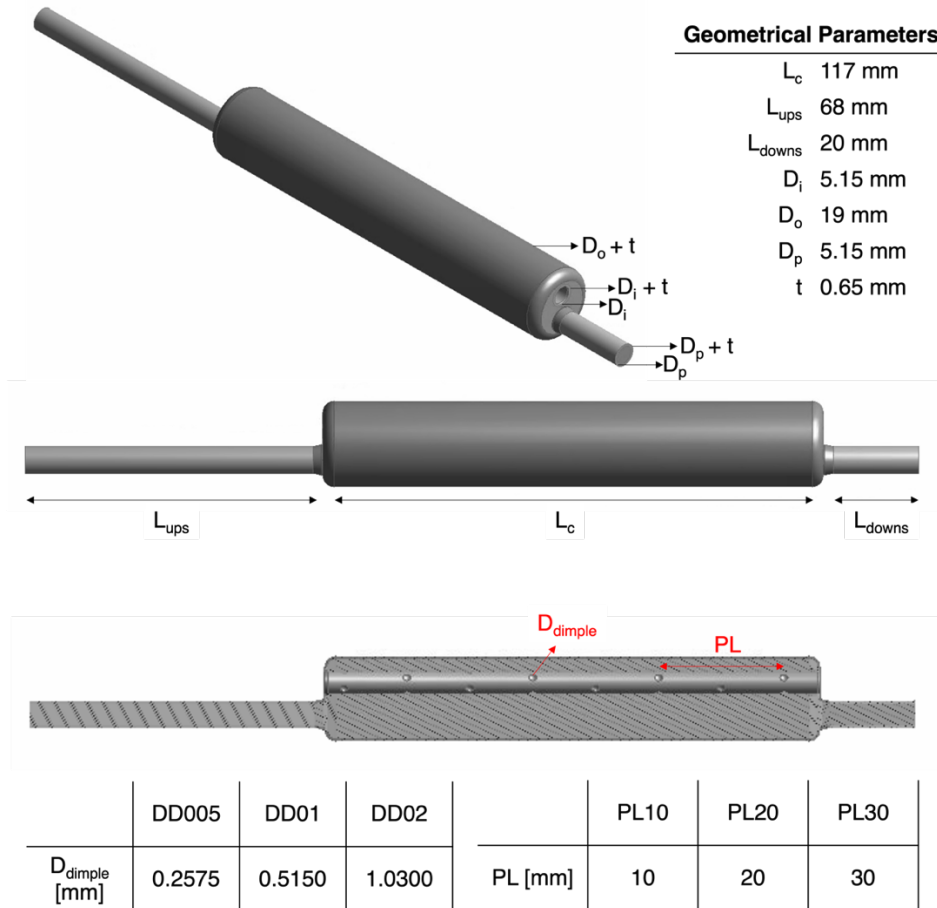


Figure 3.9: System schematic and dimensions of the DPHX

3.2 Thermophysical Properties

Recently, Banisharif et al. [67] conducted an experimental study on the thermophysical properties measurement of water-ethylene glycol (WEG) mixture (50:50) based Fe_3O_4

nanofluids at low concentration (0.01, 0.05 and 0.1 vol.%; denoted as NF001, N005 and NF01, respectively) and temperatures (253.15-293.15 K). WEG as a base fluid at 293.15 K with the amount of 0.2 wt.% in sodium dodecyl sulfonate (SDS) and 0.2 vol.% in oleic acid (OA) (which corresponds to WEG+OA+SDS in this study) to disperse and stabilize Fe₃O₄ nanoparticles. It is reported that as nanoparticle concentration increased, higher thermal conductivity and lower viscosity values were obtained, and this would affect the performance of heat transfer systems positively.

Considering the potential of these nanofluids in passive heat transfer systems, the performance of the nanofluids in the annular section of the DPHX has been investigated for the cooling-end of the SPNCmL [4]. The detail of the numerical model is given in Section 3.1.6.2 and the results are discussed in section 5.2.2. Although the nanofluid with the lowest concentration (NF001) has the smallest pressure drop value and exergy destruction with the highest PEC value, utilization of the nanofluid with the highest concentration (NF01) increases the heat transfer by 13.6% compared to WEG+OA+SDS as a base fluid. Since the DPHX is aimed to superheat the refrigerant at the low-pressure side of the refrigeration cycle, the transferred heat is considered a key parameter to continue the simulations for further investigation.

Within this scope, WEG, WEG+OA+SDS and Fe₃O₄ nanofluid (0.1 vol.%, denoted as NF01) were used as working fluids for investigating the performance of the nanofluids in the SPNCmLs with dimpled DPHXs. The thermophysical properties (thermal conductivity, heat capacity, dynamic viscosity and density) were employed as polynomials derived by temperature-dependent functions [4] to be valid in the temperature range from -30°C to 125°C. However, the mixture rule is applied to calculate the effective thermal expansion coefficient (β_e) as given in Equations (3.7) and (3.8).

$$(\rho\beta)_f = (1 - \phi_{water})(\rho\beta)_{water} + \phi_{EG}(\rho\beta)_{EG} \quad (3.7)$$

$$(\rho\beta)_e = (1 - \phi_f)(\rho\beta)_f + \phi_p(\rho\beta)_p \quad (3.8)$$

Here, ϕ is the volumetric concentration of the nanofluid and ρ is the density. Subscripts p and f denote nanoparticle and fluid, respectively. In Equation (3.7), the temperature-dependent thermal expansion coefficient of ethylene glycol [68] and tabular values of water [69] were obtained from the literature. Then, the thermal expansion coefficient of WEG calculated by Equation (3.8) was used for Fe₃O₄ nanofluids. The thermal expansion coefficient of Fe₃O₄ was taken as a constant value of 1.13×10^{-5} [70] by assuming the WEG's temperature dependency as the dominant parameter. The change in the thermophysical properties is presented in Figure 3.10, and it is seen that there is no significant difference in the thermal expansion coefficient of these three working fluids. The functions are formed based on the experimental data, but the difference between experimental data and ASHRAE values is also presented in Figure 3.10.

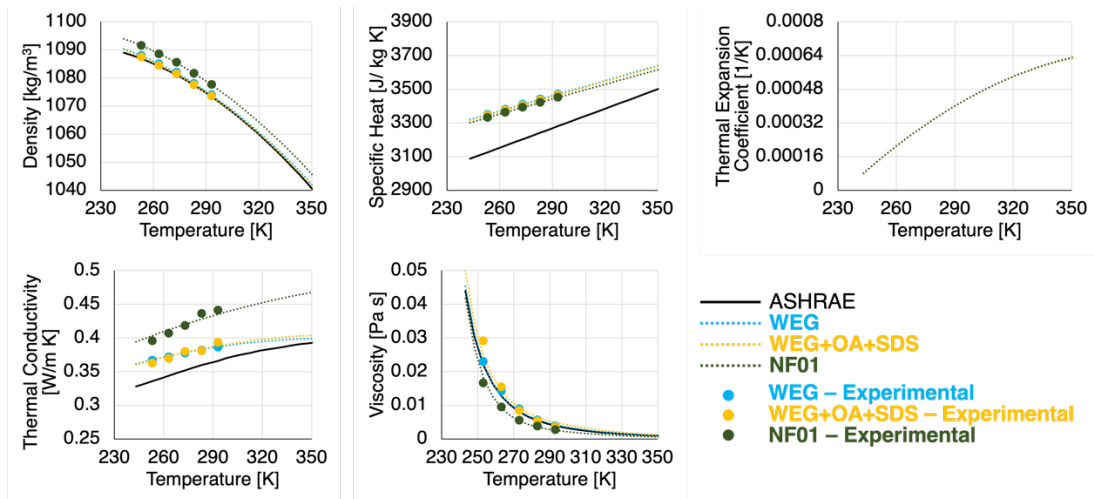


Figure 3.10: The change of thermophysical properties with temperature

All the polynomial functions introduced to numerical model are given below and the coefficients of polynomials are given in Table 3.3.

Thermal Conductivity:

$$k = a_1 T^2 + a_2 T + a_3 \quad (3.9)$$

Effective Thermal Expansion Coefficient:

$$\beta_e = b_1 T^2 + b_2 T + b_3 \quad (3.10)$$

Density:

$$\rho = c_1 T^2 + c_2 T + c_3 \quad (3.11)$$

Dynamic Viscosity:

$$\mu = d_1 e^{d_2 T} + d_3 e^{d_4 T} \quad (3.12)$$

Specific Heat:

$$c_p = (e_1 T^2 + e_2 T + e_3) 10^3 \quad (3.13)$$

Table 3.3: Coefficients of the polynomials in Equations (3.9-3.13).

<i>k</i>	<i>a</i>₁ [W/(m K³)]	<i>a</i>₂ [W/(m K²)]	<i>a</i>₃ [W/(m K)]	
WEG	-0.00000285	0.00204	0.034	
WEG+OA+SDS	-0.00000285	0.0021	0.018	
NF01	-0.0000023	0.00205	0.032	
<i>β_e</i>	<i>b</i>₁ [K⁻³]	<i>b</i>₂ [K⁻²]	<i>b</i>₃ [K⁻¹]	
WEG	-0.0000002886	0.00002223	-0.003619	
WEG+OA+SDS	-0.0000002886	0.00002223	-0.003619	
NF01	-0.0000002786	0.00002167	-0.003541	
<i>ρ</i>	<i>c</i>₁ [kg/(K² m³)]	<i>c</i>₂ [kg/(K m³)]	<i>c</i>₃ [kg/m³]	
WEG	-0.002143	0.8206	1017.5	
WEG+OA+SDS	-0.00214	0.8206	1017	
NF01	-0.002143	0.8207	1021.1	
<i>μ</i>	<i>d</i>₁ [N s/(m²)]	<i>d</i>₂ [K⁻¹]	<i>d</i>₃ [N s/(m²)]	<i>d</i>₄ [K⁻¹]
WEG	2561000000	-0.1035	8.468	-0.026
WEG+OA+SDS	2561000000	-0.103	5.468	-0.024
NF01	2561000000	-0.103	2.35	-0.0235
<i>c_p</i>	<i>e</i>₁ [J/(kg K³)]	<i>e</i>₂ [J/(kg K²)]	<i>e</i>₃ [J/(kg K)]	
WEG	-2.126E-19	0.003	2.591	
WEG+OA+SDS	2.245E-19	0.003	2.586	
NF01	-0.0000007143	0.00336	2.527	

3.3 Mesh Independency

The mesh independency analysis of the proposed model was conducted time-dependent (total time of 150 s with a time step of 0.05 s) for only smooth inner piped DPHX (cooler side) working with WEG [4]. Four different mesh numbers were investigated (M1, M2, M3 and M4 having 156247, 258423, 434597, and 612463 elements respectively). It is seen that the coarser mesh (M1 and M2) could not capture the initial unsteady heat transfer behavior between 15 and 65 s (Figure 3.11). Initially, the high heat transfer value caused by the high-temperature difference between the inlet and the inner tube decreased rapidly over time (until $t = 15$ s), and the M3 and M4 states, which have a relatively fine mesh structure, were successful in capturing the unstable behavior between 15-65 s. In order to conduct a precise evaluation of temperature and velocity distributions at the critical cross-sections with high resolution, the finest mesh structure M4 was chosen for further analysis.

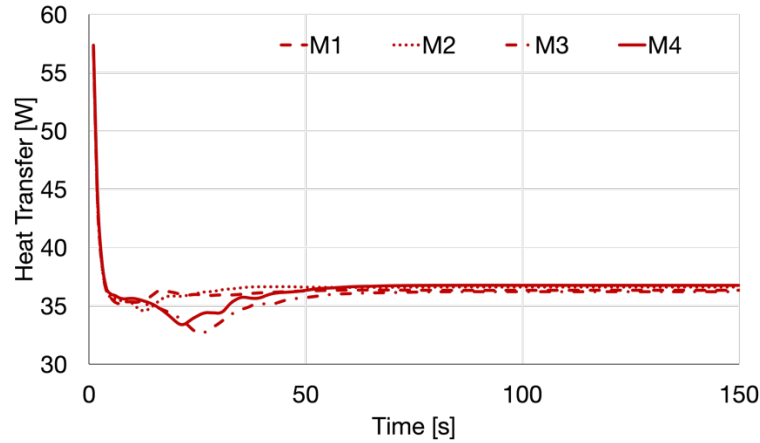


Figure 3.11: Mesh independency analysis for smooth inner piped DPHX working with WEG

3.4 Performance Parameters

The density gradient due to the temperature difference between the heating and cooling-ends is the driving mechanism of SPNCLs. Therefore, T_{max} and ΔT_{heater} can

be considered the main characteristics of SPNCmL that are used to compare different operational cases. However, it is possible to observe more information and accurate results on the performance of SPNCLs by calculating non-dimensional indicators such as ε , Nusselt number, steady-state Reynolds number and the performance evaluation criteria (PEC).

ε is defined originally for the heat exchangers, which is a ratio of the actual heat transfer to the maximum possible heat transfer. It is also used to understand SPNCL heat transfer performance. ε is defined by Equation (3.14).

$$\varepsilon = \frac{T_{L,2} - T_{L,5}}{T_{L,2} - T_c} \quad (3.14)$$

The annular flow characteristics in DPHXs have been investigated by nondimensional temperature (T^*) and velocity (V^*) distributions at critical cross-sections of the eccentric annular ducts.

$$T^* = \frac{T_s - T_c}{T_H - T_c} \quad (3.15)$$

$$V^* = \frac{V_s}{V_{max}} \quad (3.16)$$

Here, T_s and V_s are the local temperature [K] and velocity [m/s] values at these cross-sections.

Nusselt number (Nu) was used to evaluate the heat transfer performance of the system and it is given by Equation (3.17).

$$Nu = \frac{U(D_o - D_c)}{k} \quad (3.17)$$

D_o is the outer pipe diameter of the annular section. The addition of the dimples to the inner pipe surface prevents to use of a constant inner pipe diameter. Instead, D_c is derived by the wetted area of the inner pipe. The overall heat transfer coefficient (U) in Equation (3.17) is a function of the logarithmic mean temperature difference

(LMTD) and surface area of the inner pipe. The overall heat transfer coefficient was calculated by using Equation (3.18).

$$U = \frac{Q}{\pi D_c L_{DPHX} \Delta T_{LMTD}} \quad (3.18)$$

where

$$\Delta T_{LMTD} = \frac{\Delta T_1 - \Delta T_2}{\ln(\Delta T_1/\Delta T_2)} \quad (3.19)$$

$$\Delta T_1 = T_{in} - T_{DPHX} \quad (3.20)$$

$$\Delta T_2 = T_{out} - T_{DPHX} \quad (3.21)$$

Reynolds number in the DPHX is calculated by Equation (3.22).

$$Re = \frac{\rho V(D_o - D_c)}{\mu} \quad (3.22)$$

The friction factor is defined by using the model proposed for developing laminar flow in eccentric annulus [71] in Equation (3.23).

$$fRe_{\sqrt{A}} = \left[\left(\frac{3.44}{\sqrt{L^+}} \right)^2 + \left(\frac{12}{\sqrt{\epsilon} (1 + \epsilon) \left[1 - \frac{192\epsilon}{\pi^5} \tanh\left(\frac{\pi}{2\epsilon}\right) \right]} \right)^2 \right]^{1/2} \quad (3.23)$$

Here, ϵ is the aspect ratio and determined pipe diameter ratio and dimensionless eccentricity of the annulus. The pipe diameter ratio of the annular duct is in the range of 0.340-0.344 due to the dimpled inner pipe surface.

$$\epsilon = \frac{(1 + e^*)(1 - r^*)}{\pi(1 + r^*)} \quad (3.24)$$

Moreover, L^+ in Equation (3.23) is a dimensionless duct length and is given in Equation (3.25).

$$L^+ = \frac{\mu L_{DPHX}}{\dot{m}} \quad (3.25)$$

Pressure drop (ΔP) through the annular duct is defined as follows in Equation (3.26).

$$\Delta P = f \frac{L_{DPHX}}{D_o - D_c} \frac{\rho V_{in}^2}{2} \quad (3.26)$$

PEC of the system is calculated by using Nu and friction factor [49]. PEC_1 defines the effect of dimpled surface technology on the performance of DPHX for each working fluid. However, PEC_2 is defined for understanding the effect of the combination of nanofluid and dimpled inner pipe surface as defined by Equation (3.27). The base fluid is WEG+OA+SDS.

$$PEC_1 = \frac{Nu_{dimpled}}{Nu_{smooth}} \frac{1}{\left(\frac{f_{dimpled}}{f_{smooth}}\right)^{\frac{1}{3}}}, \quad PEC_2 = \frac{Nu_{nf,dimpled}}{Nu_{bf,smooth}} \frac{1}{\left(\frac{f_{nf,dimpled}}{f_{bf,smooth}}\right)^{\frac{1}{3}}} \quad (3.27)$$

Moreover, Rayleigh number is related to natural convection. When the density difference is caused by temperature difference as occurred in SPNCmLs, Rayleigh number (Ra) is defined as the ratio of the time scale for diffusive thermal transport to the time scale for convective thermal transport.

$$Ra_C = \frac{\rho \beta (T_{bulk} - T_c) (D_o - D_c)^3 g}{\mu \alpha}; \quad (3.28)$$

$$Ra_H = \frac{\rho \beta (T_H - T_{bulk}) (D_o - D_c)^3 g}{\mu \alpha}$$

Here, μ is the dynamic viscosity and α is the thermal diffusivity [m^2/s] of the working fluid. Ra is also defined by the product of Grashof number (Gr, the ratio of gravitational forces to shear stresses) and Prandtl number (Pr) as given in Equation (3.29).

$$Ra_c = Gr_c Pr_c, \quad Ra_H = Gr_H Pr_H \quad (3.29)$$

where Pr is defined in Equation (3.30).

$$Pr = \frac{c_p \mu}{k} \quad (3.30)$$

The Richardson number (Ri) defines the dominance of the natural convection over forced convection, and it is described as Equation (3.31).

$$Ri = \frac{Gr}{Re^2} \quad (3.31)$$

3.5 Local Heat Transfer Coefficient

Investigation of the local and average heat transfer coefficients for single-phase laminar flow is important to understand thermohydraulic behavior of the fluid in the developing flow phase by the fundamentals of convection. Within this scope, a local Nu number is aimed to be investigated for annular flow at both heating- and cooling-ends.

Since a constant heat flux boundary condition is employed at the heating-end in the validation section (4.2), local heat transfer coefficient is determined by Eq. (3.32).

$$h = \frac{Q}{A (T_W - T_M)} \quad (3.32)$$

Here, T_W and T_M are area-averaged wall and fluid bulk mean temperatures ($T_M = 0.5(T_o + T_i)$) at each slice, and A is the outer surface area of the cylinder.

For the main geometry investigated in this thesis, the constant temperature boundary condition is applied on both inner tube of annular sections. The heat transfer along each slide is determined by $Q = \dot{m}_{elbow\ out} c_p (T_o - T_i)$. This is also equals to convection heat transfer ($Q = hA\Delta T_{LMTD}$) which enablesto calculate h to find local Nu along heating- and cooling-ends in Results section (5.3.3).

Chapter 4

Validation

In this chapter, validation studies conducted for the numerical model have been given in detail. For SPNCmL, the heat storage effect in the initial transient and the independence of the model from the Courant number was investigated with the transient 3D numerical model. Additionally, analyses for time step and iteration number independency were also carried out. Since the heating end has a crucial role in the correct prediction of the initial transient behavior of the SPNCmL, the validation study on the natural convection heat transfer has been completed. This study also explains the reason behind the higher Nusselt numbers compared to theoretical Nusselt numbers in the literature. Finally, a validation study is conducted for the eccentricity of the double pipe heat exchanger with fully developed laminar annular duct flow for different pipe diameter ratios.

4.1 Validation of the SPNCmL

Accurate prediction of the SPNCmLs' dynamic behavior in terms of stability, thermohydraulic performance, flow propagation, and temperature distribution is crucial for the correct determination of the overall heat transfer system performance. Within this scope, the transient behavior of the SPNCmLs working with water (DIW) based Al_2O_3 nanofluids (1-3 vol.%) was validated with the well-proven experimental setup in the studies of [29,30,33] for the heater power range of 10-50 W [72].

Thermophysical properties of working fluids were introduced to the model as functions of temperature [35]. In the existing models of the effective specific heat, thermal expansion coefficient and density, temperature dependency was derived by using temperature-dependent tabular values of DIW's properties as a dominant

parameter. It is found that the specific heat of the working fluids does not change with respect to the operating temperature range. Therefore, it is assumed to be constant for each nanofluid and DIW for the simulations. Thermal conductivity and viscosity data of working fluids are obtained from experimental study [73] and defined as second-order polynomial functions in the numerical model. Further information about thermophysical properties is given in the [35].

In addition to validation, the heat storage effect of the thermal mass on the dynamic behavior of the developing flow in SPNCmL was also investigated. Firstly, only fluid flow (M-FF) is modeled was developed to investigate the dynamic behavior of the developing fluid in SPNCmLs. In the simple model, only fluid flow is studied. Later, the simple model is improved by the addition of pipe walls (M-Cu) and insulation material (M-Ins) with the aim of investigating the heat storage effect of the thermal mass. The schematic geometry of the SPNCmLs for each model with dimensions is given in Figure 4.1. Mesh and time step independency analysis of the improved model was conducted to investigate the Courant number effect on the results of the numerical study for distinguishing the numerical error. The Courant-Frederichs-Lewy condition limits the ratio of the time step (Δt) and spacing of the grid (Δx) and called as Courant number (Co) (Equation 4.1) [74,75]. It is recommended that Co should be less than or equal to 1.

$$Co = V \frac{\Delta t}{\Delta x} \leq 1 \quad (4.1)$$

Here V is magnitude of velocity [m/s].

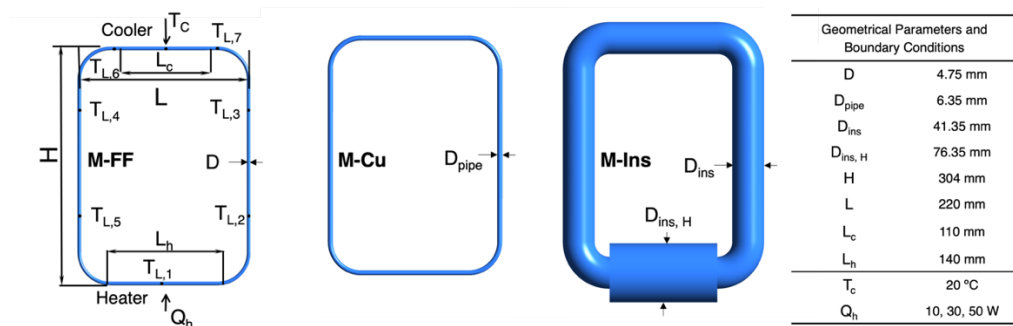


Figure 4.1: Schematic presentation of the SPNCmL in the models and its dimensions in the validation study

In the cooling end of SPNCmL, a constant temperature was defined as 293.15 K whereas constant heat flux (corresponding to 10, 30 and 50 W of heat rates for the heater surface area) was applied to the heating-end of the SPNCmL. Commercial software (ANSYS CFX) was used to build a geometry and solve the numerical model. In the previous study for this model [32], the mesh independency of the solution was investigated for three different mesh numbers (745456, 565681 and 348087 elements, respectively) by comparing the temperature difference between the heating-end's inlet and outlet, and maximum temperature which are used for comparison of numerical and experimental results. Since the difference was negligible, the coarse mesh number was used in the analyses. Finer boundary layer elements and finer meshes were employed for the heating and cooling ends compared to the rest of the system. Since there is no significant difference in the results of the steady-state numerical study [35] and steady-state phase of this study, the same mesh was also applied to the M-FF model. In this model, the independency of the solution from the time step was investigated for 0.1 s, 0.5 s, 1 s, and 5 s for the condition of DIW-based SPNCmL working with 50 W of heater power. Since the more appropriate agreement between M-FF and experimental data [30] is obtained for 0.1 s of the time step, all of the validation analyses are conducted for 0.1 s (Figure 4.2).

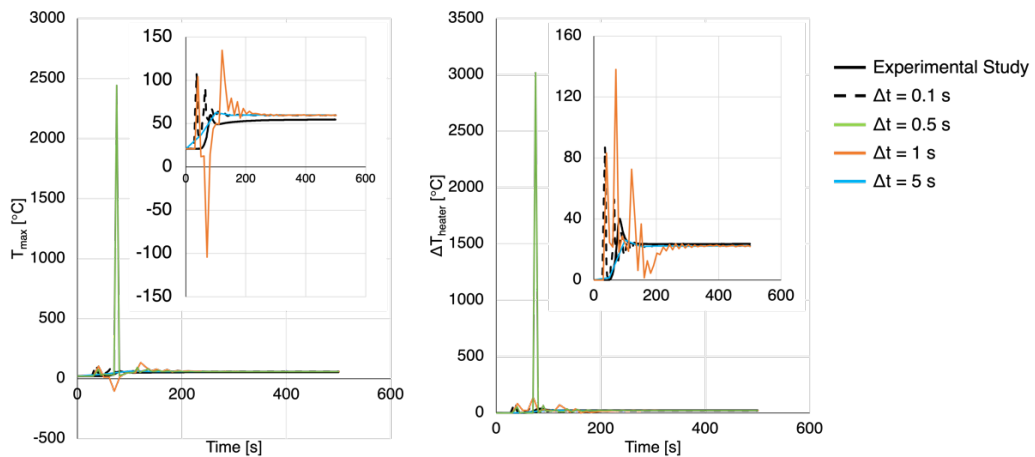


Figure 4.2: Effect of time step on the solution of the transient 3D model in terms of (a) T_{max} and (b) ΔT_{heater}

In the M-Cu model, the thermal inertia effect of the copper (Cu) pipe walls with the 6.35 mm of outer diameter was investigated. The total mesh element number of the M-Cu model was 860320. Similar to the M-FF model, heating and cooling ends have finer boundary layers and finer meshes in the M-Cu model. The constant temperature at the cooling-end and constant heat flux at the heating-end were applied to the outer pipe walls. The rest of the system was assumed to be adiabatic. The M-Cu model can be considered as an intermediate step between M-FF and M-Ins models, and only the condition of DIW based SPNCmL working at 50 W was investigated. In the M-Ins model, the geometry of the M-Cu model was covered with elastomeric rubber as insulation material. The thickness of the insulation material is obtained from the experimental setup (Figure 4.1) and thicker insulation was applied to the heating-end similar to the experimental study [29,30,33]. Moreover, the constant heat transfer coefficient ($5 \text{ W/m}^2\text{K}$) at 22°C was also applied to the outer surfaces of the insulation domain to simulate the experimental environment for the M-Ins model. Additionally, temperatures at the pipes were obtained for the M-Ins analysis instead of fluid flow in which M-FF and M-Cu. The thermophysical properties of Cu pipe and elastomeric rubber as an insulation material are given in Table 4.1. Elastomeric rubber's thermophysical properties were taken from [76].

Table 4.1: Thermophysical properties of Cu pipe and elastomeric rubber as insulation material

Thermophysical properties	Cu	Elastomeric Rubber
Thermal conductivity [W/m K]	401	0.0375
Density [kg/m^3]	8933	64
Specific heat capacity [J/kg K]	385	837

The effect of Co on the solution of the M-Ins model was investigated for different mesh element numbers (Coarse Mesh as $CM = 1222082$ and Fine Mesh as $FM = 1939823$) and time steps (0.05 and 0.1 s). Moreover, mesh independency analysis of the solution was investigated at the condition of $Co=0.2$ by adaptive time step. Data of numerical solution is collected at every 10th-time step for all models. Initial conditions

were set to zero velocities for each direction and 0 Pa of relative pressure. The initial temperature was 294.15 K.

Modeling only fluid flow (M-FF) results in oscillations of the T_{\max} and ΔT_{heater} for developing flow phase. The reason behind these oscillations is reported as unmodelled heat storage [77]. As can be seen from Figure 4.3, modeling Cu pipe over the flow has damped the oscillations in the developing flow phase of the M-FF model and results in a shift of the maximum peak value. However, the peak value in the developing flow phase is still higher compared to experimental results. Moreover, the addition of the insulation material and using the average temperature at pipe cross-section similar to experiments reduce the peak value in the developing phase.

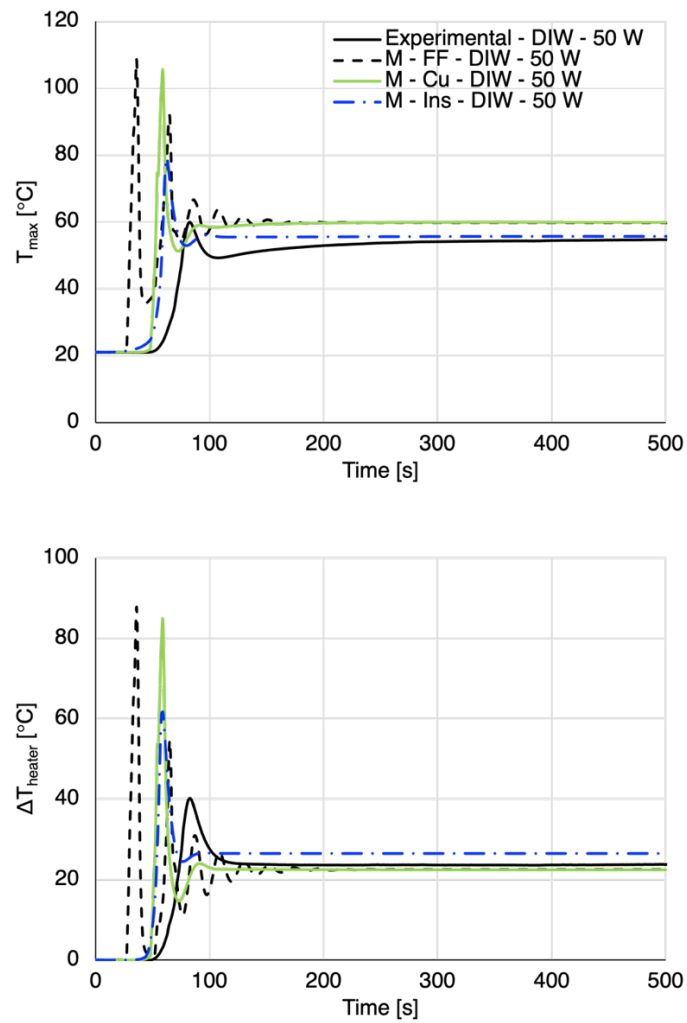


Figure 4.3: Effect of heat storage on dynamic behavior of the system in developing flow phase

Correct modeling of the developing flow phase is important for accurate prediction of the dynamic behavior of the SPNCmL from start-up to rest. Although modeling the heat storage effect of thermal mass could dampen the oscillations in the developing flow phase, the first peak value in the temperatures was still higher compared to experiments. Moreover, it is seen that the flow in the numerical study started to circulate before the experiments. Considering that circulation starts after $t=40$ s and the fluid flow reaches the steady-state condition almost $t=90$ s, the stability of the numerical model has critical importance in this period. Therefore, the effect of the Co number was investigated for different mesh numbers (CM and FM) and time steps (0.1 and 0.05 s) of the M-Ins model. As mentioned in the previous section, the Co number is used to characterize the stability of the numerical model and must be equal to or less than 1. However, it increases up to 92.8 for the M-Ins model having FM and 0.1 s of timestep and it varies in the range of $Co = 8-22$ for the steady-state phase of all conditions (Figure 4.4).

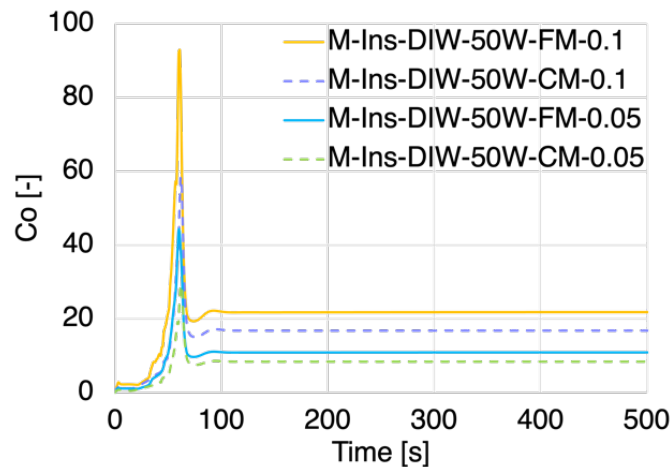


Figure 4.4: Time dependent variation of Co number for M-Ins model having different mesh numbers and time steps

Higher Co numbers require further investigations on the stability of the M-Ins model. Therefore, adaptive time step analyses to keep $Co=0.2$ were conducted for both CM and FM cases. However, Figure 4.5 shows that keeping $Co=0.2$ did not affect the peak values of temperatures and system behavior at the developing flow phase compared to previous simulations.

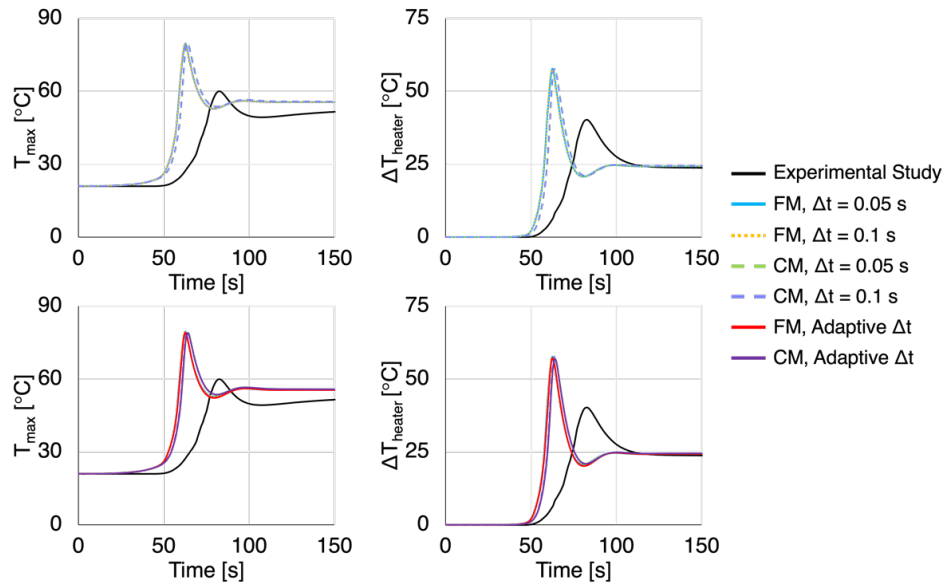


Figure 4.5: Effect of Co number on temperatures for different mesh numbers and time steps

Moreover, the effect of the Co number on T^* and V^* at the heating end was investigated for different mesh element numbers and time steps (Figure 4.6 and Figure 4.7). Since natural circulation develops at the heating-end, flow and heat transfer characteristics are important in this section. It is found that the FM case has higher T^* gradients and the change of T^* with time steps ($t=60$ s, when Co has the highest value) is significant compared to the CM case. Unlike T^* distributions, the change of Co number with mesh element sizes and time steps does not affect V^* distributions considerably.

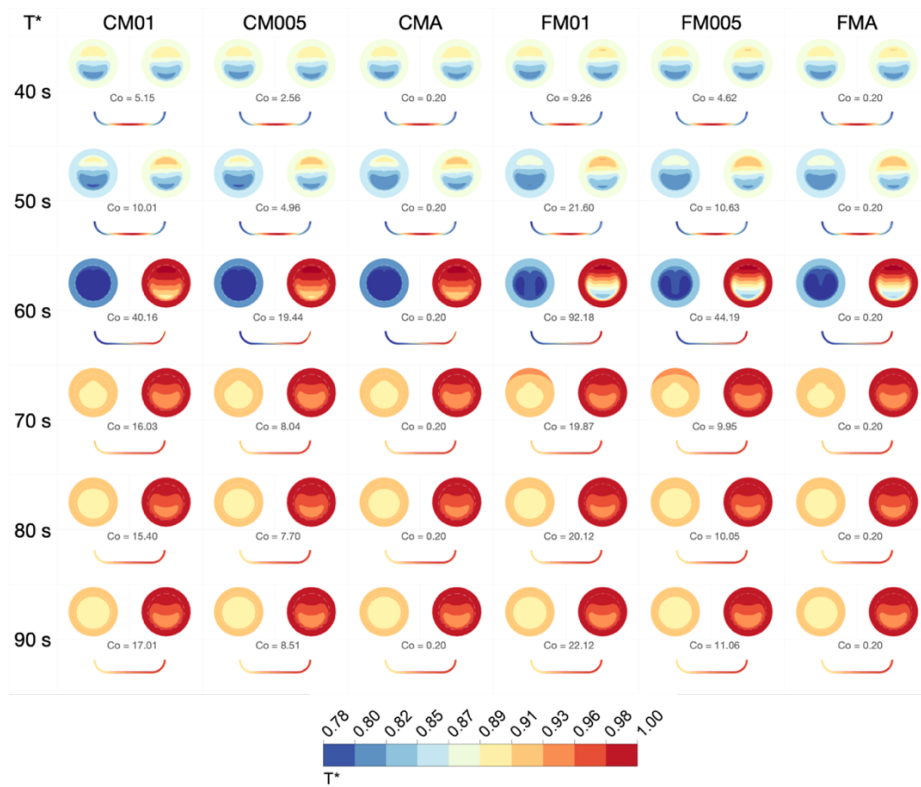


Figure 4.6: Effect of Co number on T^* distributions in the developing flow phase

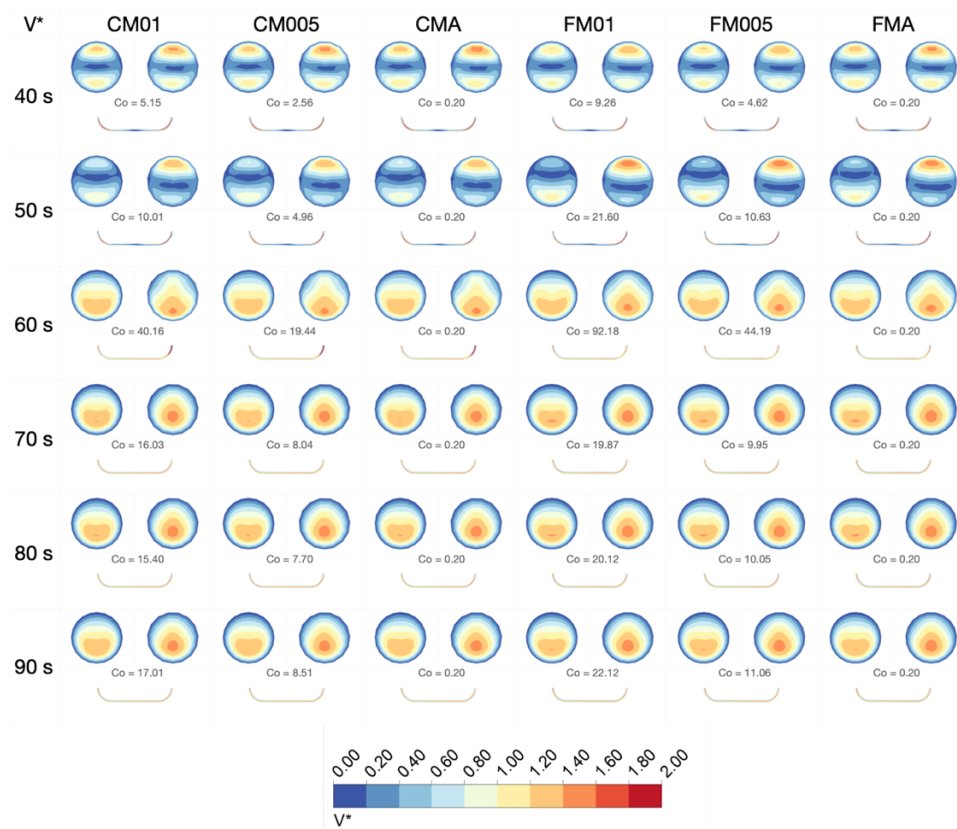


Figure 4.7: Effect of Co number on V^* distributions in the developing flow phase

Additionally, steady-state phases of both numerical models (M-FF and M-Ins) was normalized with experimental results [30] as Equations (4.2)-(4.4).

$$\varepsilon_N = \frac{\varepsilon_{\text{numerical}}}{\varepsilon_{\text{experimental}}} \quad (4.2)$$

$$T_{\text{max},N} = \frac{T_{\text{max,numerical}}}{T_{\text{max,experimental}}} \quad (4.3)$$

$$\Delta T_{\text{heater},N} = \frac{\Delta T_{\text{heater,numerical}}}{\Delta T_{\text{heater,experimental}}} \quad (4.4)$$

This validation is presented as a normalization of the numerical results with experimental data in Figure 4.8. It is clearly shown that ε can be predicted $\pm 15\%$ error margin and higher heater powers reduce the error between experimental and numerical results for ΔT_{heater} . T_{max} and ΔT_{heater} are overpredicted by up to 15% and %20 compared to experimental data, respectively. DIW data is in good agreement with the experimental results whereas nanofluids have deviations up to %20. Moreover, the higher accuracy of the M-Ins model compared to the M-FF model is shown in Figure 4.8.

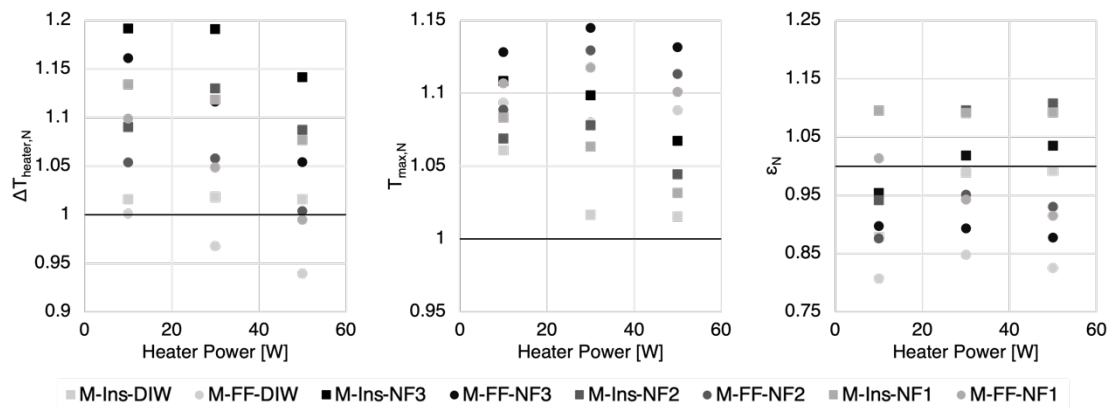


Figure 4.8: Validation of M-FF and M-Ins models with experimental results [30] for operating conditions

4.2 Validation for Natural Convection Heat Transfer

Investigation of the local and average heat transfer coefficients for single-phase laminar flow in the SPNCmL's heating end is required to understand thermohydraulic behavior of the fluid in the developing flow phase by the fundamentals of convection. Additionally, this fundamental approach would be used in further analyses on the effects of diameter ratio and eccentricity, and geometry and pattern of dimples on DPHX performance. However, correlations to predict heat transfer coefficients for single-phase laminar flow in horizontal cylindrical tubes with constant heat flux boundary condition are restricted to fully developed flow, high Prandtl numbers and constant fluid properties [2]. Meyer and Everts [2] investigated the natural convection effects on the development of the local heat transfer characteristics in smooth horizontal circular tubes with a constant heat flux boundary condition. In their experimental study, it was found that natural convection effects became significant with increasing heat flux and tube diameters, and it also decreased the thermal entry length and increased Nu numbers for simultaneously developing flow. Moreover, three different regions were defined considering local heat transfer coefficients.

The steady-state model to investigate developing flow characteristics was validated by Meyer and Evert's experimental study results for the system with a 4 mm inner pipe diameter and 8 kW/m² of constant heat flux. A good agreement between experimental and numerical results was obtained as shown in Figure 4.9.

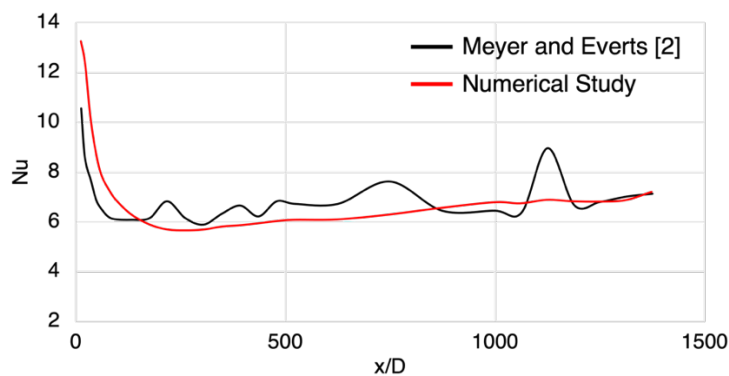


Figure 4.9: Validation of the numerical model on the investigation of the local and average heat transfer coefficients for single-phase and simultaneously developing laminar flow [2]

The local Nu number change along the SPNCmL's heating end (Gz^{-1} considering Reynolds and Prandtl numbers) was investigated for hydrodynamically developed and thermally developing flow to understand natural convection effects. In order to meet the conditions of hydrodynamically developed flow, the tube with 100 mm of length was added before the heating end, and in order to eliminate the possible effects of backflow the tube with 20 mm of length was modeled after the heating end as shown in Figure 4.10. The inlet velocity was defined as 0.02591 m/s at 301.3 K. Constant heat flux boundary condition was employed as 23.9 kW/m² corresponding to 50 W of heater power.

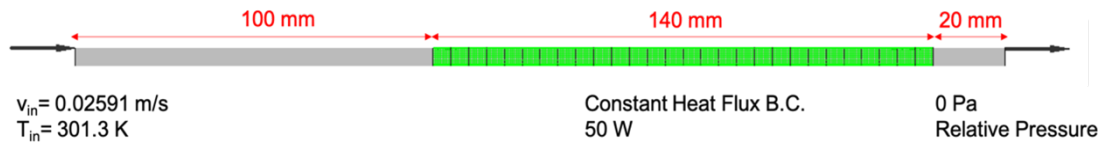


Figure 4.10: Axial temperature and velocity distributions in the horizontal circular tube for hydrodynamically developed and thermally developing flow [3]

Comparison of the change of local Nu along the heater-end with the well-known correlations of Shah and London [78], Shah [79] and Siegel [80] proposed for hydrodynamically developed and thermally developing flow was reported in [3]. In the entrance region, the numerical results were in good agreement with correlations developed by Shah [79], as shown in Figure 4.11. However, Nu started to increase after this decreasing trend ($Gz^{-1} < 0.004$). Meyer and Everts [2] explained the possible reason for this behavior by considering the natural convection effects. Higher Gr_m and lower Re result that the local Nu does not continue to decrease until the flow becomes fully developed, and then increases to reach a constant value under natural convection effects. Compared to the results of Shah and London [78], Shah [79] and Siegel [80], Nu obtained from the numerical model increased by 92% and 68% at $Gz^{-1} = 0.028$, respectively. Meyer and Everts [2] also found that natural convection effects become significant with increasing heat flux and tube diameters, and it also decreases the thermal entry length and increases the Nu numbers for simultaneously developing flow in their experimental study. The Nu is higher up to 38% in comparison to the results of Meyer and Everts [2] for 4 mm pipe diameter and 8 kW/m² constant heat

flux. Moreover, it is found that the thermal entrance length for forced convection laminar flow ($Gz^{-1} = 0.05$) is shortened for this study ($Gz^{-1} = 0.004$) due to the higher Gr_m and thus natural convection effects.

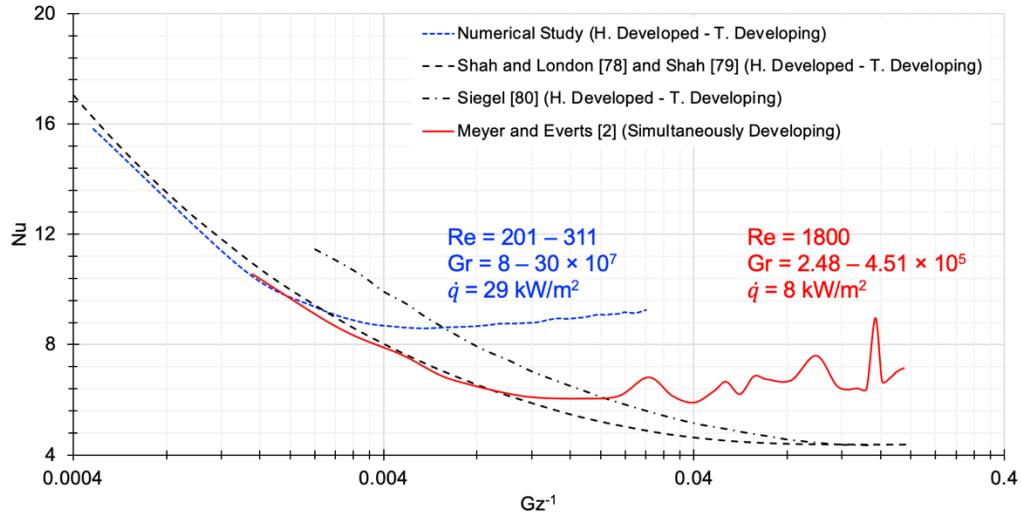


Figure 4.11: The local Nu number along horizontal circular tube representing SPNCmL's heating end

4.3 Validation of Eccentric Double Pipe Heat Exchanger

The flow in the DPHX has the characteristics of laminar flow in the annular section and it is validated by the study of Manglik and Fang [5] which investigated the effects of eccentricity and thermal boundary conditions on the fully developed laminar annular duct flow for different pipe diameter ratios as shown in Figure 4.12. The validation study is conducted for the cases of $e^* = 0$ and 0.6 at $r^* = 0.5$ ensured by 10 and 20 mm inner and outer diameters, respectively. In order to obtain fully developed laminar flow conditions, the upstream pipe with 500 mm in length was used. The length of the investigated region was 120 mm. The Reynolds number was 500 at the inlet of the annular pipe for both cases.

The comparison of the calculated Nu numbers with the ones given by Manglik and Fang [5] is presented in Table 4.2. Manglik and Fang [5] neglected the axial conduction, viscous dissipation, and effects of body forces in their study. When the

gravitational force was ignored in the numerical study, Nu numbers exhibit decreasing trend with the increase of eccentricity similar to the results of Manglik and Fang [5], but they are still higher as a result of considering the axial conduction in the numerical study. When the gravitational force is taken into account to model more realistic conditions, it is found that Nu numbers are much higher compared to theoretical study and higher eccentricity values have higher Nu numbers.

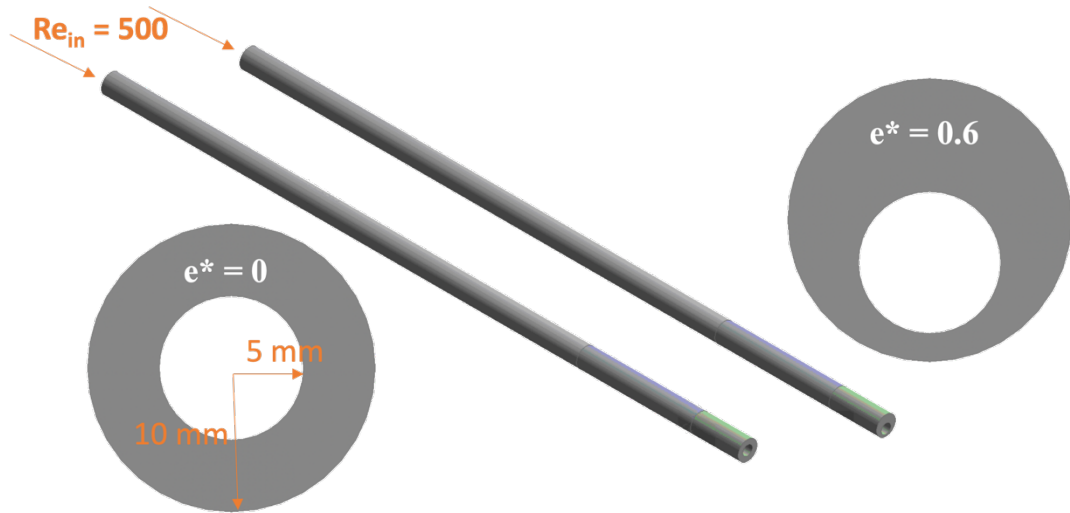


Figure 4.11: The local Nu number along horizontal circular tube representing SPNCmL's heating end

Table 4.2: Comparison between numerical results and Manglik and Fang [5]

Investigated cases at $r^* = 0.5$	Numerical Results	Manglik and Fang [5]
$e^* = 0$ / gravitational force is included	8.621	5.733
$e^* = 0.6$ / gravitational force is included	9.087	2.244
$e^* = 0$ / gravitational force is excluded	4.853	5.733
$e^* = 0.6$ / gravitational force is excluded	3.137	2.244

Chapter 5

Results and Discussions

This chapter presents the main findings of the preliminary study, which is conducted to investigate the main geometrical parameters on SPNCmL performance, and of the effect of key parameters on the DPHXs performance and the performance of nanofluid-based SPNCmL with dimpled DPHXs.

5.1 Results of Preliminary Study

This preliminary study was conducted to investigate the effects of AR and pipe diameter on the performance of the SPNCmL. Figure 5.1 shows that natural circulation did not occur in the SPNCmL with a pipe diameter of 3.56 mm for all AR, and heat transfer took place by pure conduction, instead of natural convection. The temperatures, equality of the effectiveness to 1 and the amount of transferred heat are indicators of this pure conduction situation.

For other cases, as AR and pipe diameter increase, ΔT_{heater} and T_{max} decrease (Figure 5.1.a-b). Because the increase in pipe diameter increases the total mass in the SPNCmL. In addition to larger pipe diameters, higher AR causes higher mass flow rates, and this results in lower temperatures. Figure 5.1.c shows that effectiveness, which is strongly dependent on temperatures, increases as pipe diameter and AR decreases. Figure 5.1.d shows that higher pipe diameters suppress the AR effect, but heat transfer capability increases with pipe diameters as well as AR.

Considering the higher effectiveness values for smaller pipe diameters, and insignificant change of effectiveness with AR but an increase of heat transfer capability with AR, the main geometry is decided to be having pipe diameter of 5.15 mm and AR of 0.8.

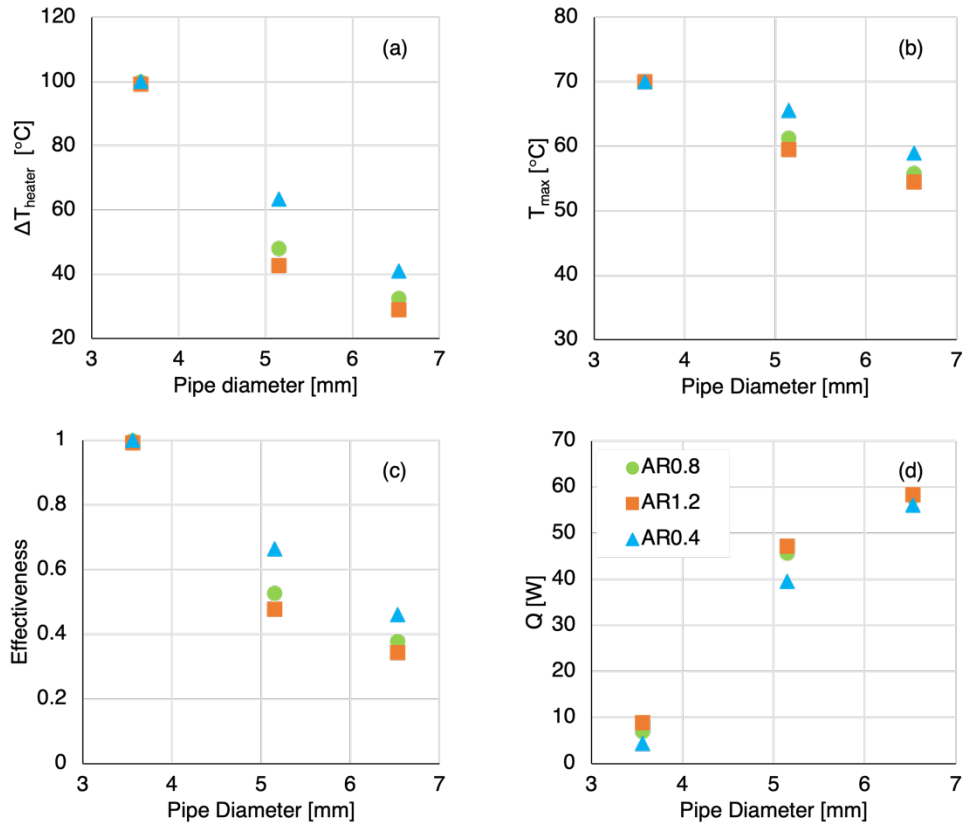


Figure 5.1: Preliminary results in terms of (a) ΔT_{heater} , (b) T_{max} , (c) effectiveness and (d) heat transfer capability ($Q [W]$)

5.2 Results of key parameters

5.2.1 Eccentricity

The effect of the eccentricity on the DPHX performance was investigated in terms of the change of heat transfer with time as presented in Figure 5.2. In Figure 5.3 and the following figures, E0, E032, E039, E054, E061, E069 and E1 indicate the eccentricity values $e^* = 0, 0.32, 0.39, 0.54, 0.61, 0.69$ and 1 , respectively. Although the higher heat transfer values were obtained because of the higher temperature differences between the inlet fluid and the inner pipe surface, a drastic reduction was observed for all cases. An increase from $e^* = 0.32$ to 0.61 results in a delay in the time required to reach a steady state. Compared to obtained tiny peaks before steady flow in these four e^* values, the flow reaches steady flow conditions right after the drastic reduction for the cases of E0,

E069 and E1. For these values, an increase of e^* causes a shorter time to reach a steady state.

In the numerical model, the cases of E032-E069 have blends with a radius of 2 mm at the inlet and outlet of the annular section. However, these blends were removed to satisfy similar inlet and outlet conditions (upstream and downstream pipes) for fully concentric and eccentric cases of E0 and E1, respectively. Figure 5.2 shows that the increase of e^* results in reduction in the heat transfer by 15% for E069 case compared to E032 with 2 mm of corresponding center-to-center distance difference ($e_{E069} - e_{E032}$). Additionally, the oscillations were observed for the E0 and E1 cases in the steady regime. The possible reason of these oscillations may be the modelling of the fully concentric (E0) geometry and eccentric (E1) geometry without blends.

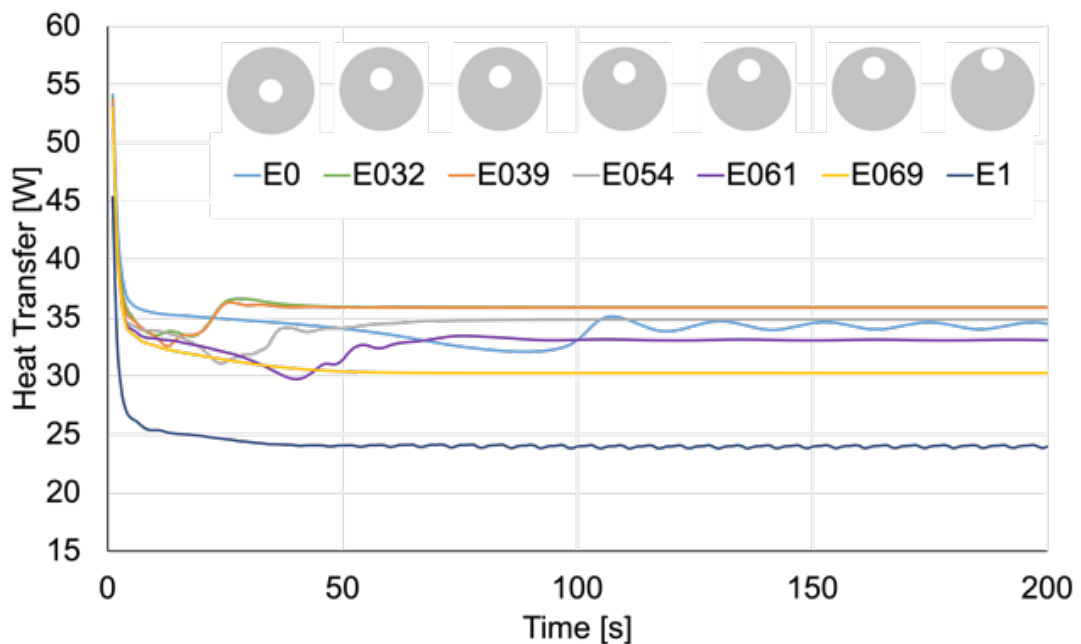


Figure 5.2: Time dependent heat transfer for different eccentricity values

Figure 5.2 also shows the unstable heat transfer behavior in the time range of 15-60 s. The heat transfer in the annular duct in this time range is evaluated in terms of T^{**} and V^{**} at the middle section of the annuli and axial cross-section for all cases as presented in Figure 5.3-5.5.

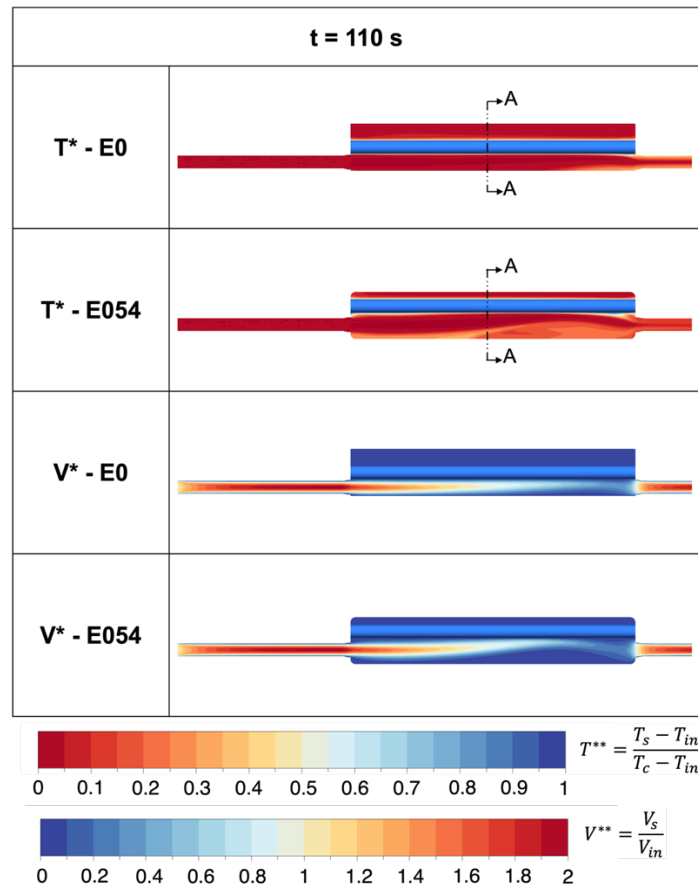


Figure 5.3: Axial T^{**} and V^{**} distribution for E0 and E054 cases at $t = 110$ s

As shown in Figure 5.3, the warm fluid enters the DPHX and flows along the wider section of the annulus without any interaction with the cooler inner pipe for the concentric case (E0). However, increasing eccentricity by moving the inner pipe up results in fluctuations in the fluid flow. This behavior is presented by an axial distribution of the T^{**} and V^{**} at $t = 110$ s, in which the transferred heat in E0 is the same as E054 at $t = 110$ s.

Figure 5.4 and Figure 5.5 show the T^{**} and V^{**} distributions at the middle cross-section (cross-section AA in Figure 5.3). Entering warmer fluid develops a warm fluid pocket below the inner pipe but increasing eccentricity results in the distribution of this fluid pocket (i.e. E069 and E1) (Figure 5.4). As time progresses, the density of the reddish area, which means higher temperature values, decreases. Here, eccentricity has a key role which causes the flow of entering fluid through the uppermost region of the annuli (Figure 5.5). This fluid motion moves the cooler fluid pocket to the wider section of the annuli and results in the mixing of warmer and cooler fluid.

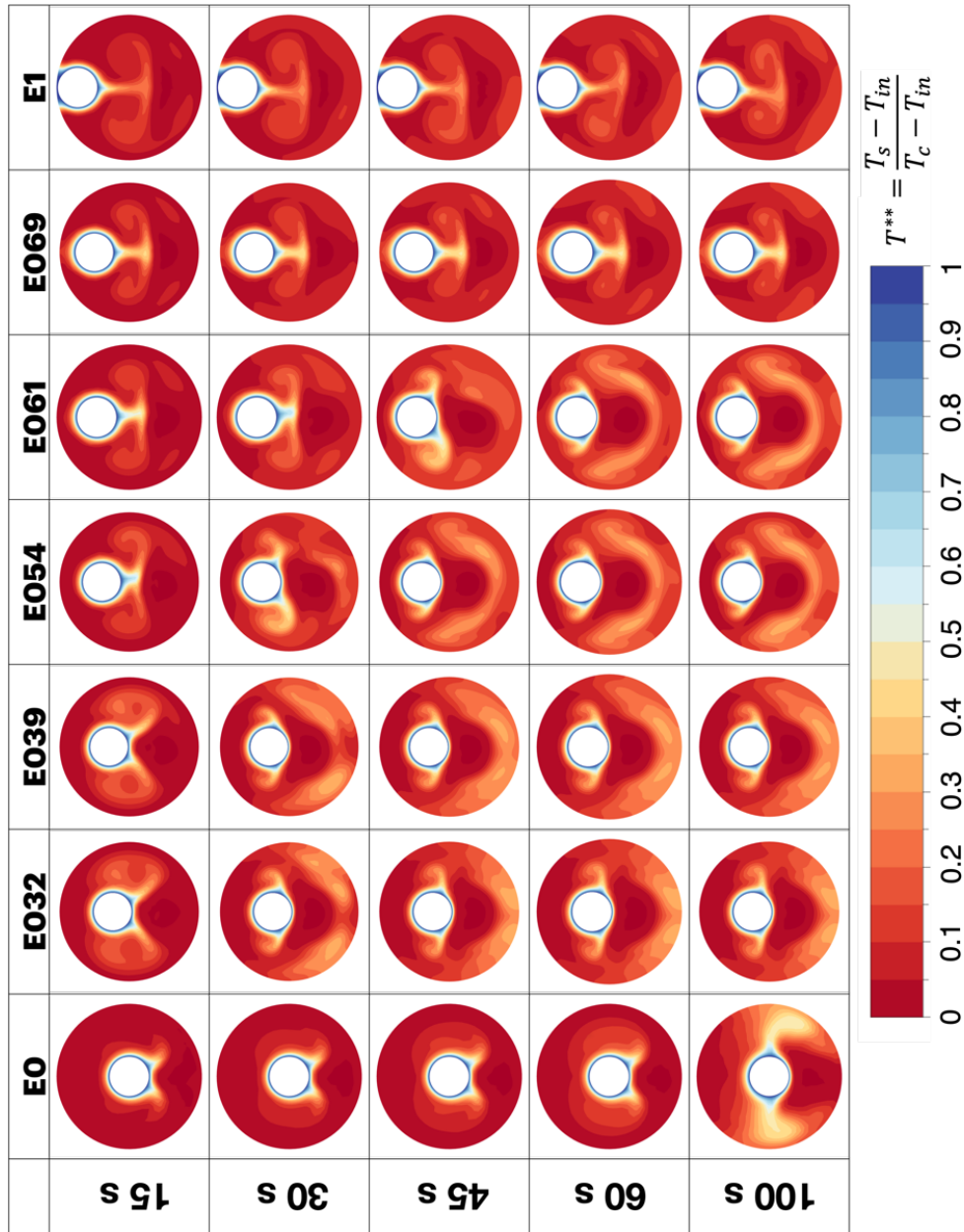


Figure 5.4: T^{**} distribution in middle cross-section (AA) of the DPHX

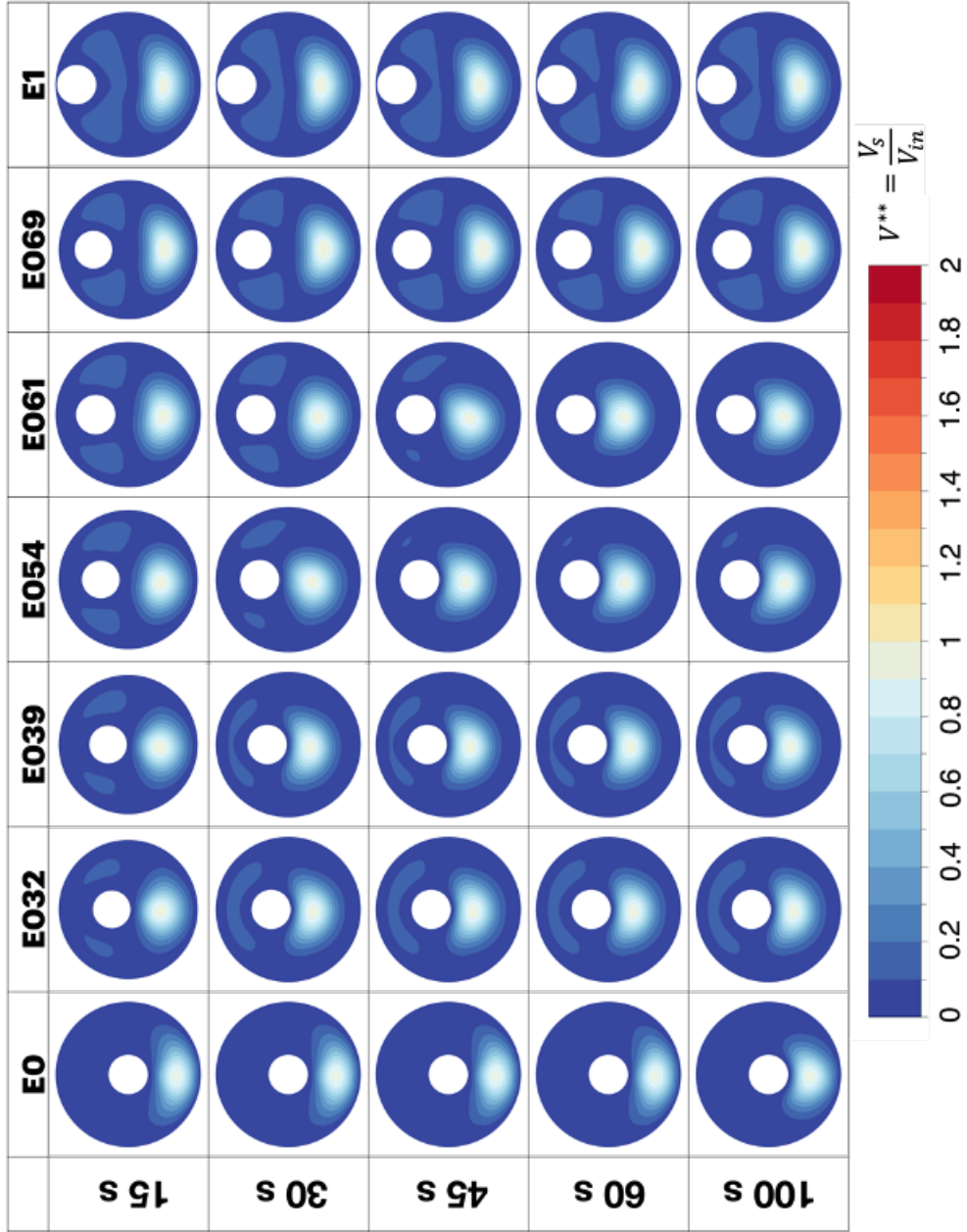


Figure 5.5: V^{**} distribution in middle cross-section (AA) of the DPHX

Figure 5.6 shows that the Nu number (obtained at $t = 200$ s) decreases with increasing e^* . Lower Re numbers were obtained for E032 and E039 in which the higher V^{**} distributions were observed at the narrow section of the annuli. However, the highest Re numbers are obtained for E069 and E1 in which V^{**} distributions with high values below the inner pipe. The values found for all cases are higher compared to the results of Manglik and Fang [5] which has similar boundary conditions (constant temperature at the inner pipe and adiabatic outer wall). Manglik and Fang [5] found that the Nu number varied in the range of 4.769 and 4.998 for the fully developed flow in the annular duct (0.25 of pipe diameter ratio and $e^* = 0.4-0.6$). The neglect of gravitational force, axial conduction and viscous dissipations (as employed in [5]) results in lower Nu numbers compared to neglecting only viscous dissipations (Table 4.2). Moreover, the effect of the partial inlet of the fluid from a tube with a smaller diameter (5.15 mm) through the annular section on Nu numbers can be investigated in future studies.

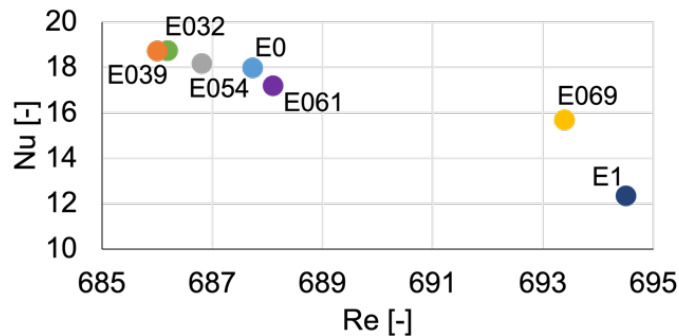


Figure 5.6: The variation of Nu number with Re

5.2.2 Nanofluids

Since the effect of nanofluids on heat transfer performance at the low-pressure side in the refrigeration system is aimed to be investigated in this study, the change of heat transfer with time is evaluated in Figure 5.7. In Figure 5.7 and the following figures, NF001, NF005 and NF01 are expressed as nanofluids having 0.01, 0.05 and 0.1 volumetric concentrations, respectively. The higher temperature difference between the inlet and the inner pipe results in a higher heat transfer value at the beginning, but

as time progress (to 15 s) drastically reduction in heat transfer is obtained for all working fluids. In the time range of 15-65 s, the heat transfer change is unstable, and it can be seen that an increase in nanofluid concentration delays the time required to reach steady-state flow conditions.

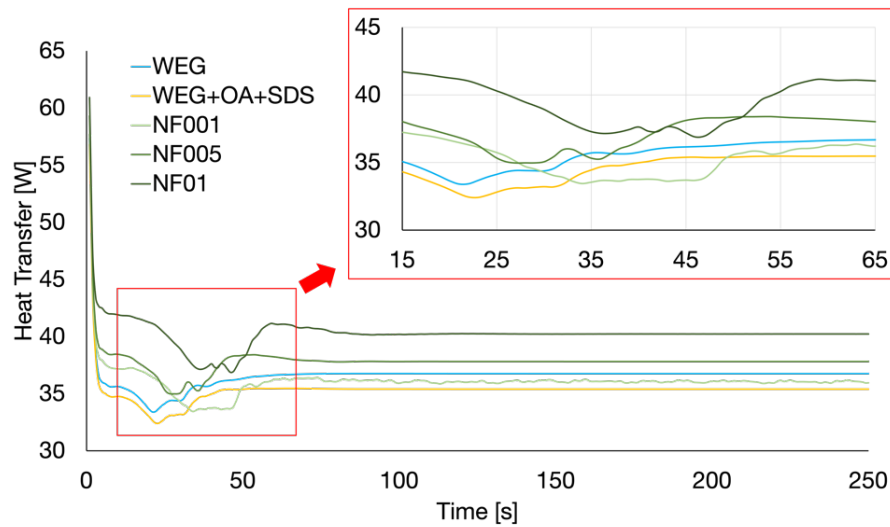
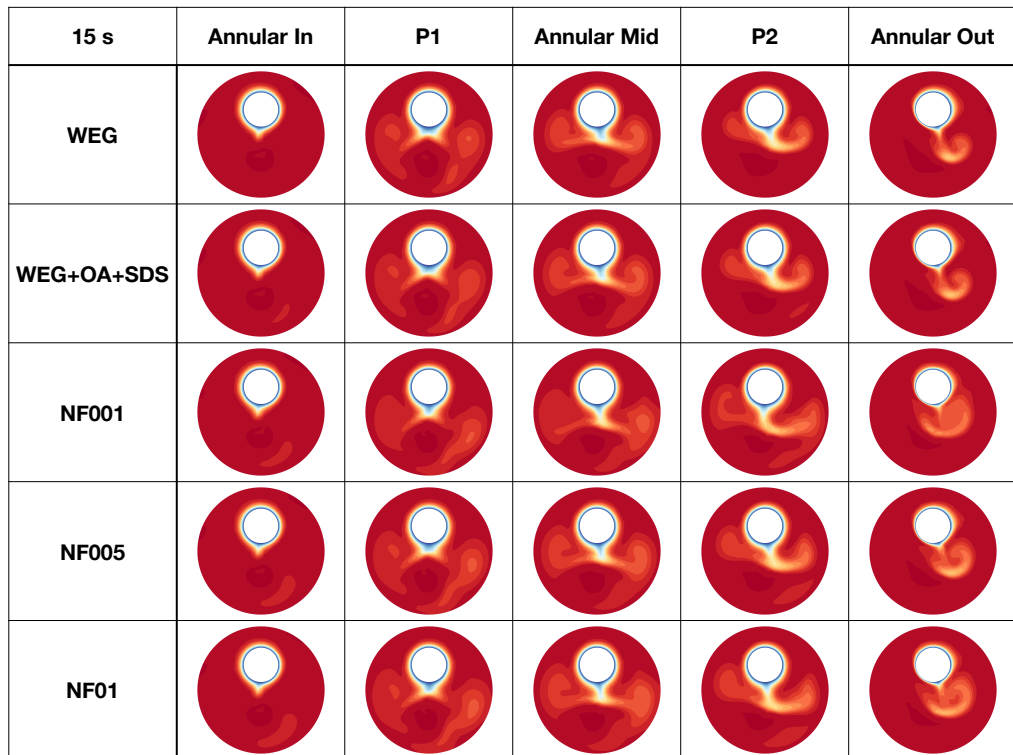
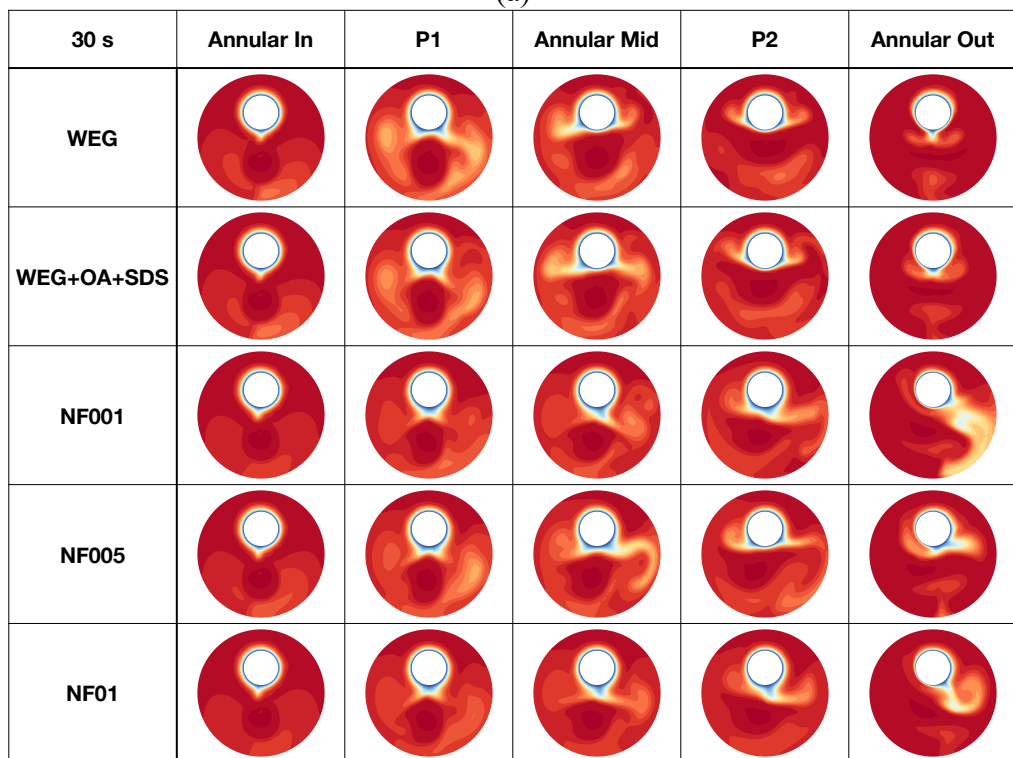


Figure 5.7: Time dependent variation of heat transfer [4]

Focusing on the time range of 15-65 s in which the fluctuations observed before steady-state condition, the heat transfer in the annular duct is evaluated in terms of T^{**} and V^{**} at critical cross-sections (Figures 5.8 and 5.9). The cross-section P1 and P2 are in the middle of the first half and second half, respectively. Hot fluid entering the pipe results in a hot fluid pocket at the wider section of the annular. Cross-sectional distributions of T^{**} (Figure 5.8) and axial distributions of T^{**} and V^{**} (Figure 5.10) this hot pocket region continues through the middle section for all cases. As time progress, the higher T^{**} value distribution, which means cooler fluid, is obtained near the inner pipe and it increases with nanofluid concentration. Additionally, a higher T^{**} area at the narrow section of the annular duct is obtained for the NF01 case (Figure 5.10). V^{**} increases with nanofluid concentration and the velocity of the entering hot fluid decreases along the annulus and the flow is developed through the uppermost region of the annulus (Figure 5.9 and Figure 5.10). This behavior enables the distribution of cold fluid in the wider region of the annulus and thus mixing of warm and cold fluid as shown in the cross-sections of P2 and out presented in Figure 5.8.

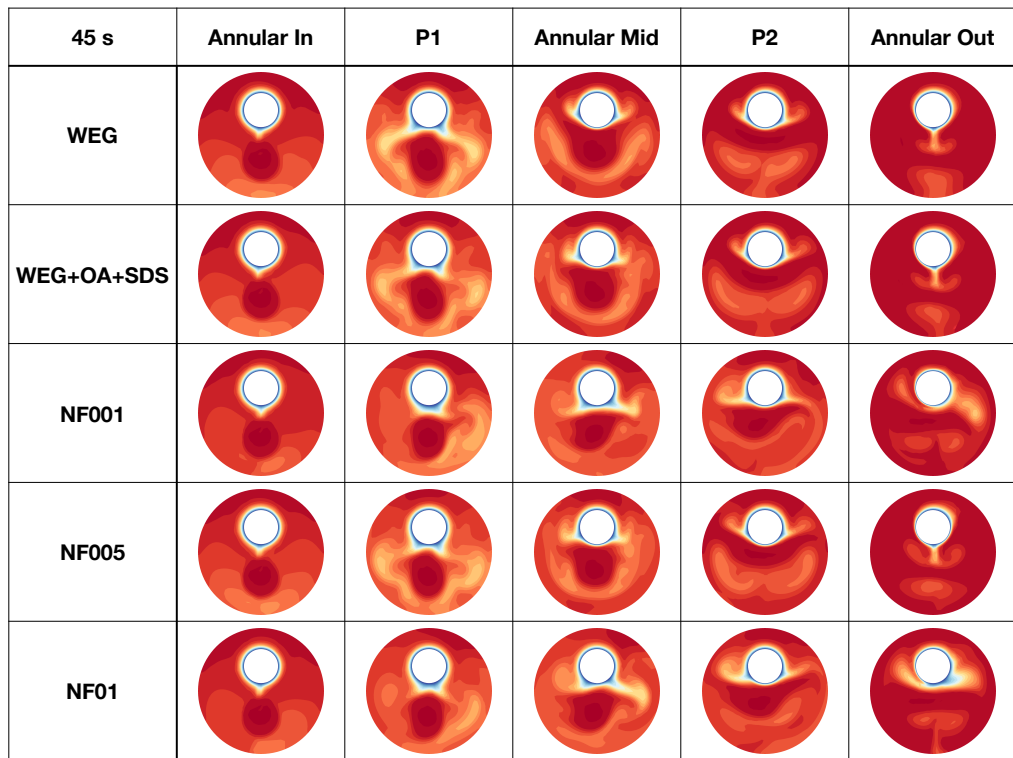


(a)

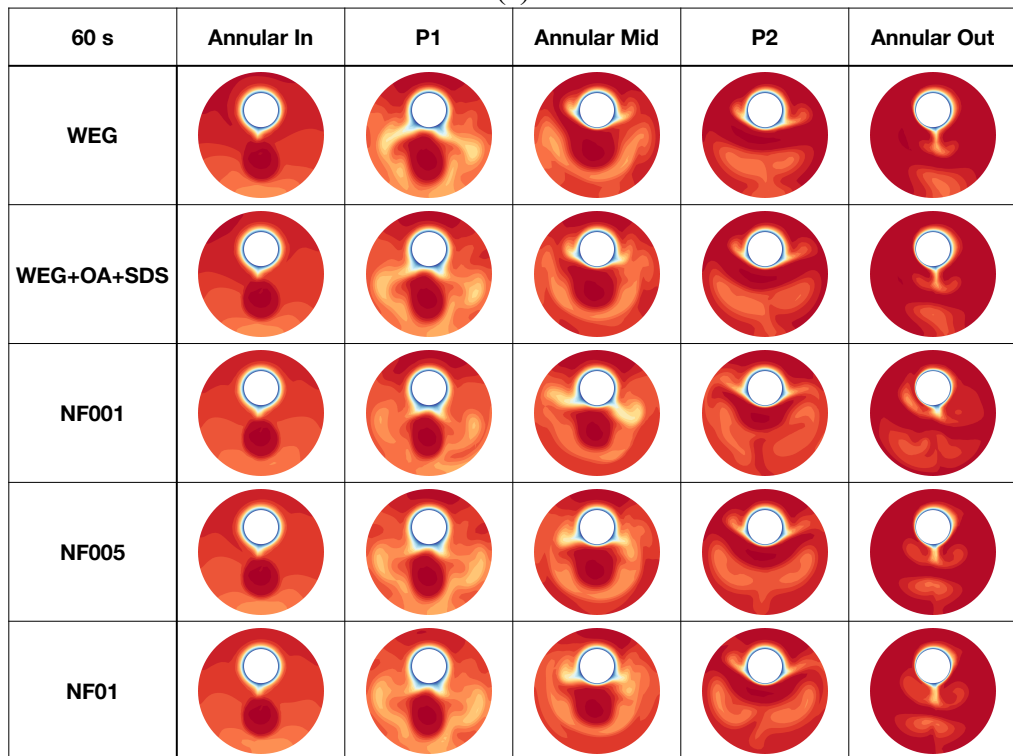


(b)

Figure 5.8: Cross-sectional T^{**} distributions at the times (a) 15 s, (b) 30 s, (c) 45s and (d) 60 s with its (e) legend and the locations

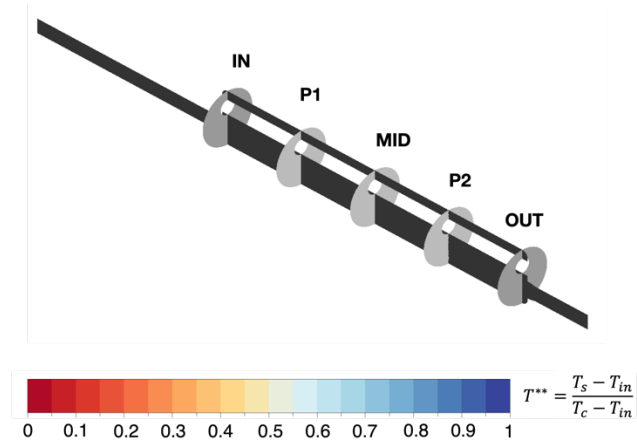


(c)



(d)

Figure 5.8: (continued)



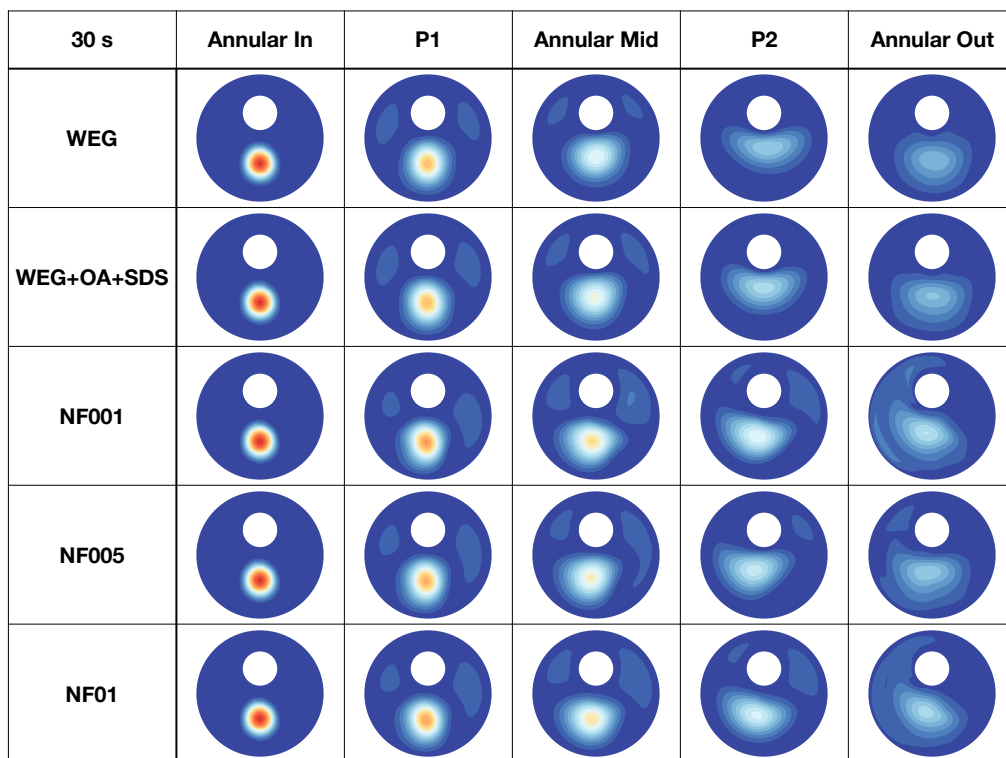
(e)

Figure 5.8: (continued)

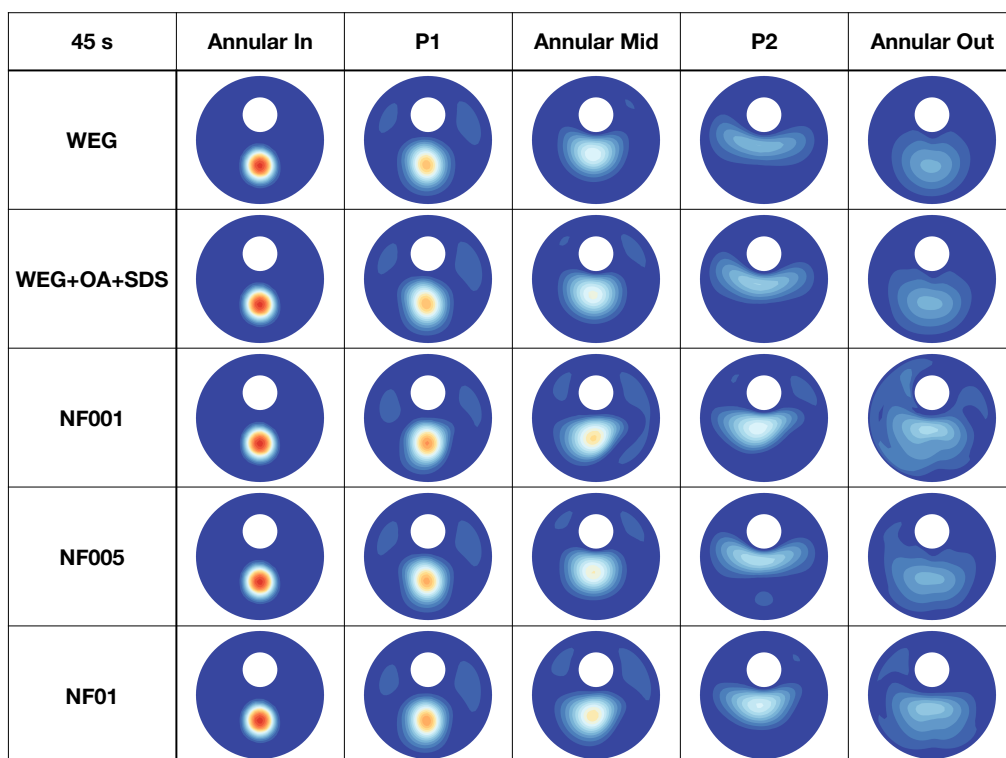
15 s	Annular In	P1	Annular Mid	P2	Annular Out
WEG					
WEG+OA+SDS					
NF001					
NF005					
NF01					

(a)

Figure 5.9: Cross-sectional V^{**} distributions at the times (a) 15 s, (b) 30 s, (c) 45s and (d) 60 s with its (e) legend.

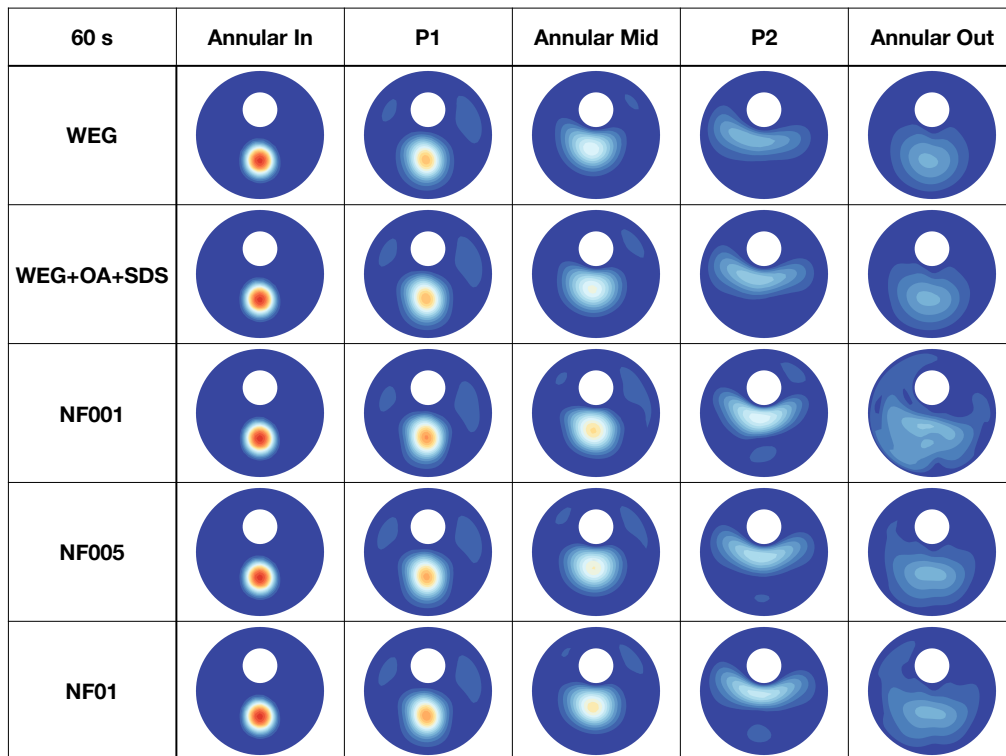


(b)

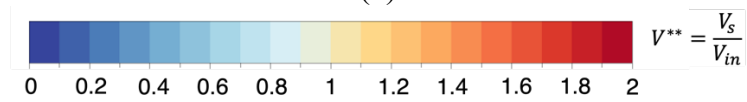


(c)

Figure 5.9: (continued)



(d)



(e)

Figure 5.9: (continued)

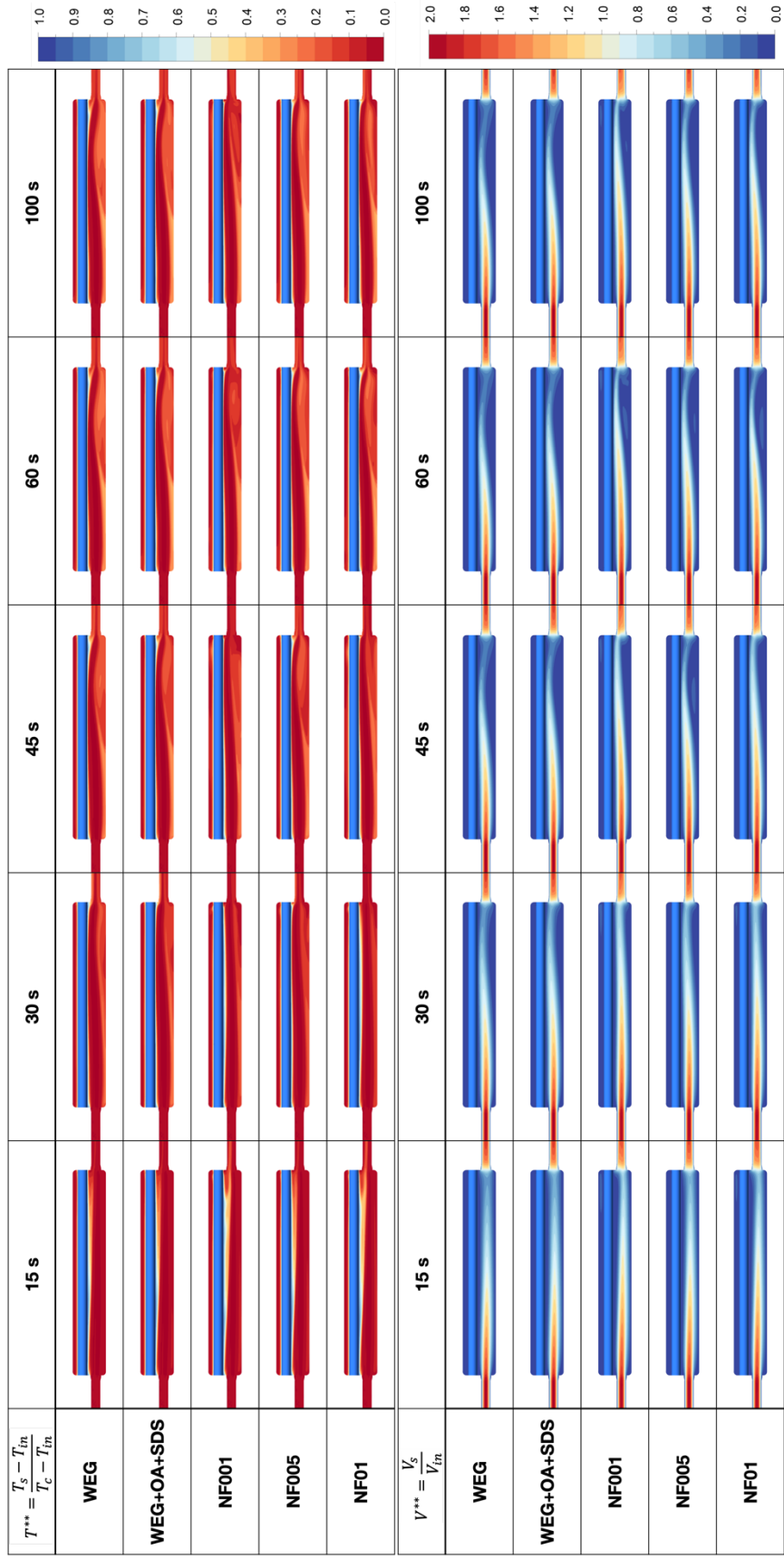


Figure 5.10: Axial distributions of the T^{**} and V^{**} along the annular duct

Additionally, the heat transfer performance is evaluated by variation of Nu number by Re. Figure 5.11 shows that WEG has the highest Nu number, and it decreases slightly for WEG+OA+SDS and nanofluid cases. However, the Re changes independently from the concentration of the nanofluids due to the nonlinear variation of the viscosity values. Manglik and Fang [5] investigated the effects of eccentricity and boundary conditions on the fully developed laminar annular flow for different pipe diameter ratios. Focusing on the similar eccentricity and pipe diameter ratio values in this study, they found that the Nu number varies in the range of 4.769 and 4.998 for the fully developed flow in the annular duct under having the 0.25 of pipe diameter ratio and 0.4-0.6 of eccentricity limits, respectively. This range is valid for constant temperature boundary condition at the inner tube and adiabatic wall of the outer tube. The Nu numbers found in our study are higher than Manglik and Fang [5]. The possible reason behind this could be our geometry. In most of annular duct studies, the working fluid enters the annular duct directly from the annuli region. However, it enters partially from a tube with a smaller diameter (5.15 mm) in our geometry. This affects the flow propagation through the annuli region as shown in Figures 5.8-5.10.

Since the DPHX is aimed to superheat the refrigerant at the low-pressure side of the refrigeration cycle, the transferred heat is investigated for all cases. Although, the addition of the OA and SDS reduces the transferred heat, heat transfer increases (by 13.6% for NF01 compared to WEG+OA+SDS as a base fluid) for the nanofluids (35.53 W, 34.22 W, 34.75 W, 36.55 W and 38.89 W for WEG, WEG+OA+SDS, NF001, NF005 and NF01 respectively). In addition to increased V^{**} values due to the lower viscosity and higher T^{**} values with expanded temperature gradient, improved heat transfer by nanofluids shows that they can be used as secondary heat transfer fluids at the low-pressure side in refrigeration systems.

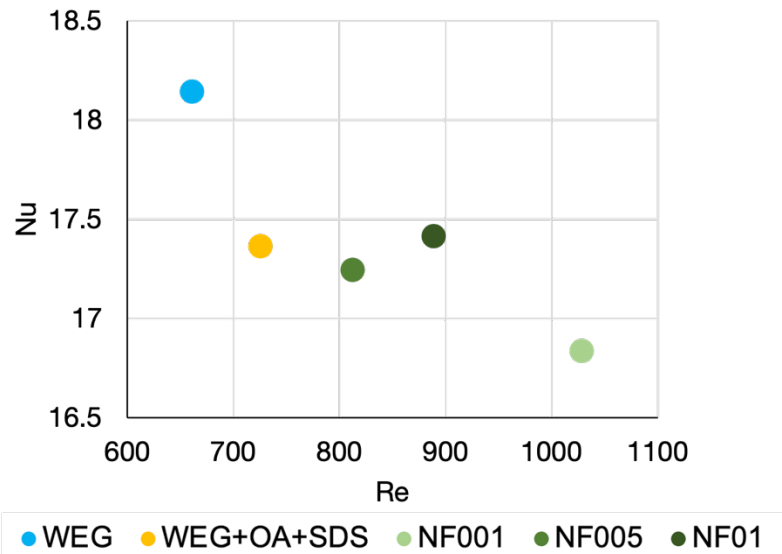


Figure 5.11: Variation of Nu with Re

The Δp decreases with the increasing Reynolds number, and nanofluids have smaller values compared to base fluid because of the lower viscosity of nanofluids. The nonlinearity in the viscosity behavior for the investigated concentrations also affects the Δp values because of its dependency on the friction factor. Additionally, the PEC values of the nanofluids have been determined by assuming the WEG+OA+SDS as base fluid (Figure 5.12). Considering the tiny changes in Nu numbers in Figure 5.11, smaller pressure drops of nanofluids result in $PEC > 1$ for all cases which means that the improvement of heat transfer is larger than the increase in the pressure drop penalty. The nanofluid with the smallest concentration (NF001) has the smallest pressure drop value of 3.88 Pa with $PEC = 1.08$.

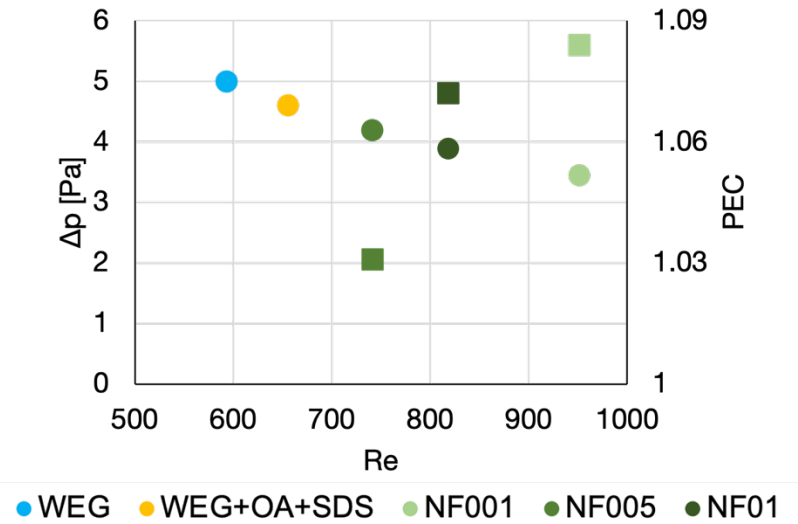
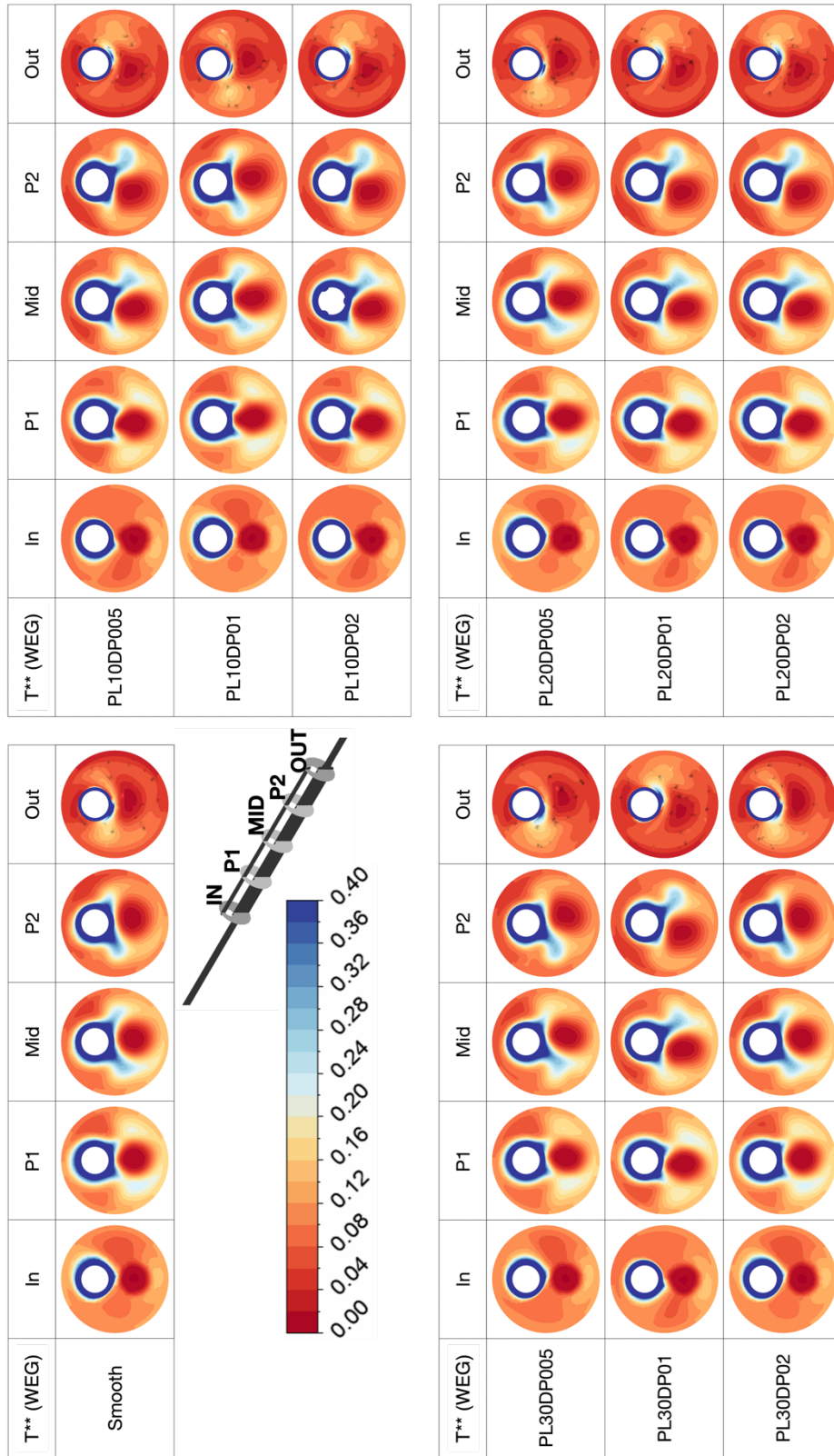


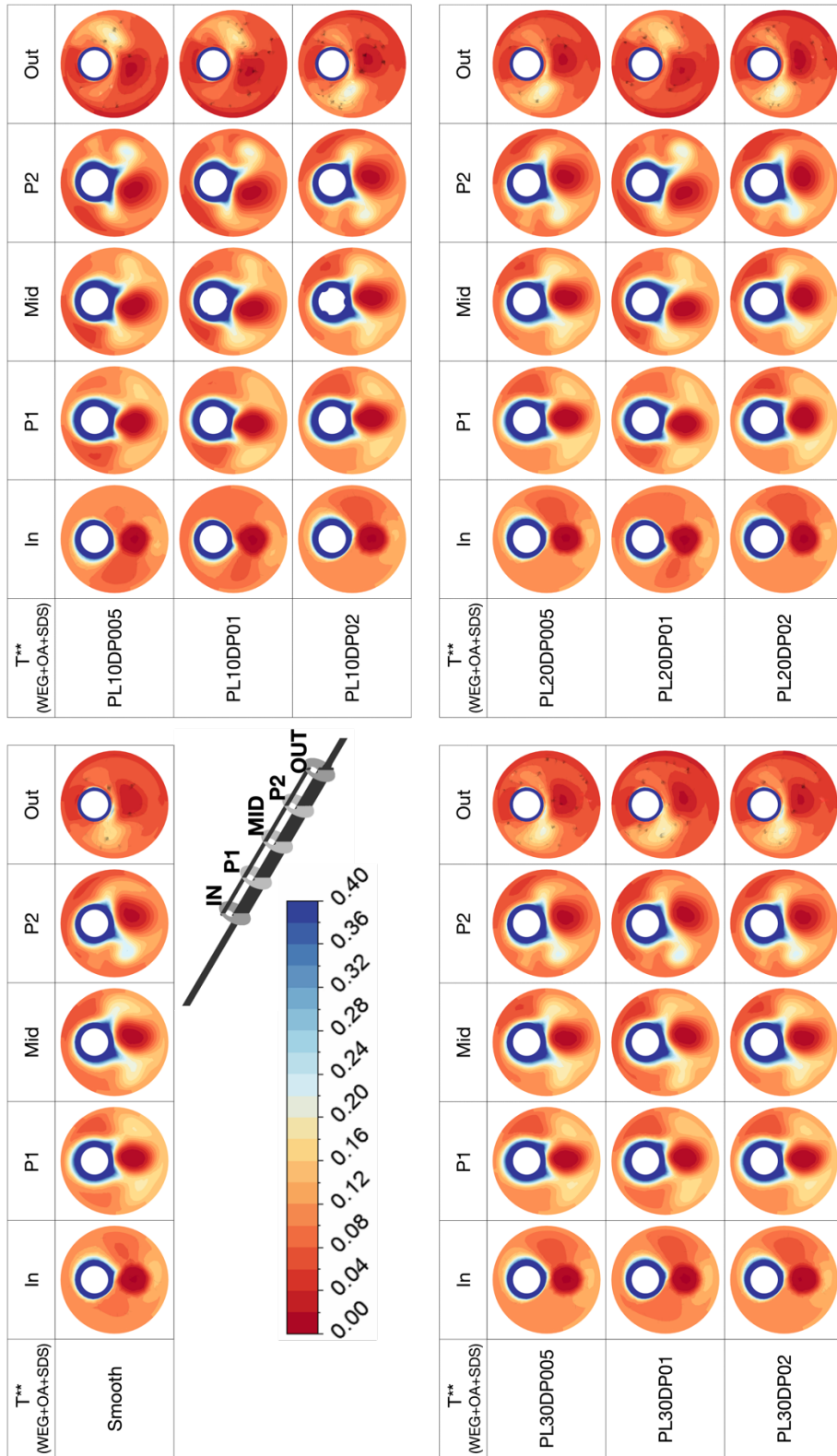
Figure 5.12: Variation of Δp and PEC with Re (circle and square markers indicate the Δp and PEC respectively.)

5.2.3 Combination of dimpled surface technology and nanofluids

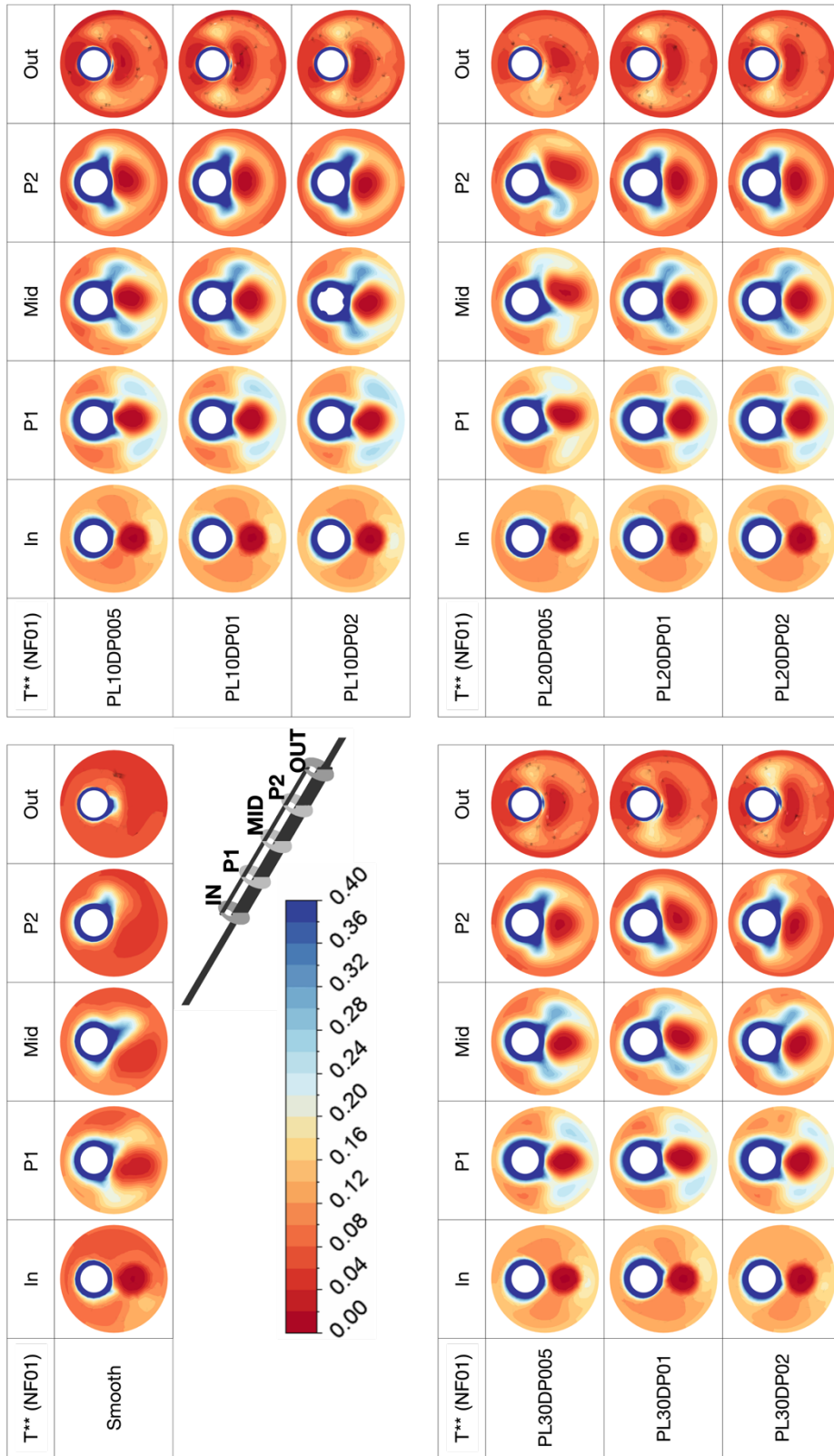
Understanding the effect of the combination of dimpled surface technology and nanofluids on the heat transfer performance of DPHX is one of the aims of this thesis. Therefore, T^* and V^* at the annular section have been investigated to evaluate annular flow propagation. Figures 5.13 and 5.14 show T^* and V^* distributions at the critical cross sections (P_{in} , P_1 , P_{mid} , P_2 and P_{out}). The cross-section P_1 and P_2 are in the middle of the first half and second half of the annulus, respectively. Compared to WEG and WEG+OA+SDS cases, cooler fluid temperature distribution (higher T^*) is wider from P_{in} to P_{mid} at the combination of NF01 and dimples (Figure 5.13.c). The magnitude of the V^* is smaller in the smooth pipe for the NF01 case but utilization of dimples drives the working fluid with high velocity until the cross-section P_{out} of the annulus which can be also seen in Figure 5.15.c. This higher velocity fluid region from cross-sections P_{in} to P_{out} is also seen for WEG and WEG+OA+SDS (Figure 5.15.a and 5.15.b) for all cases.



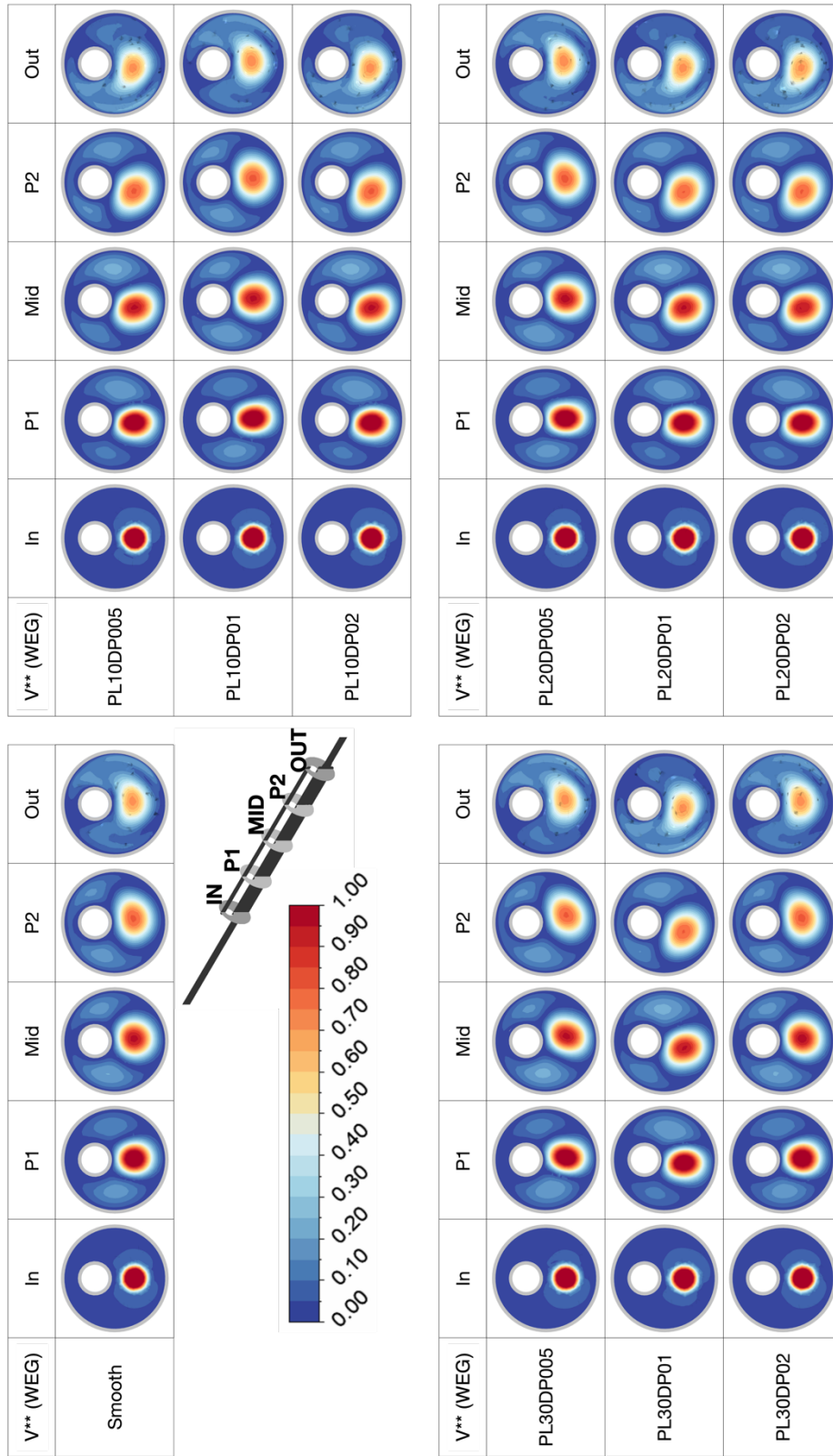
(a) Figure 5.13: T^{**} distributions at the critical cross-sections for (a) WEG, (b) WEG+OA+SDS and (c) NF01



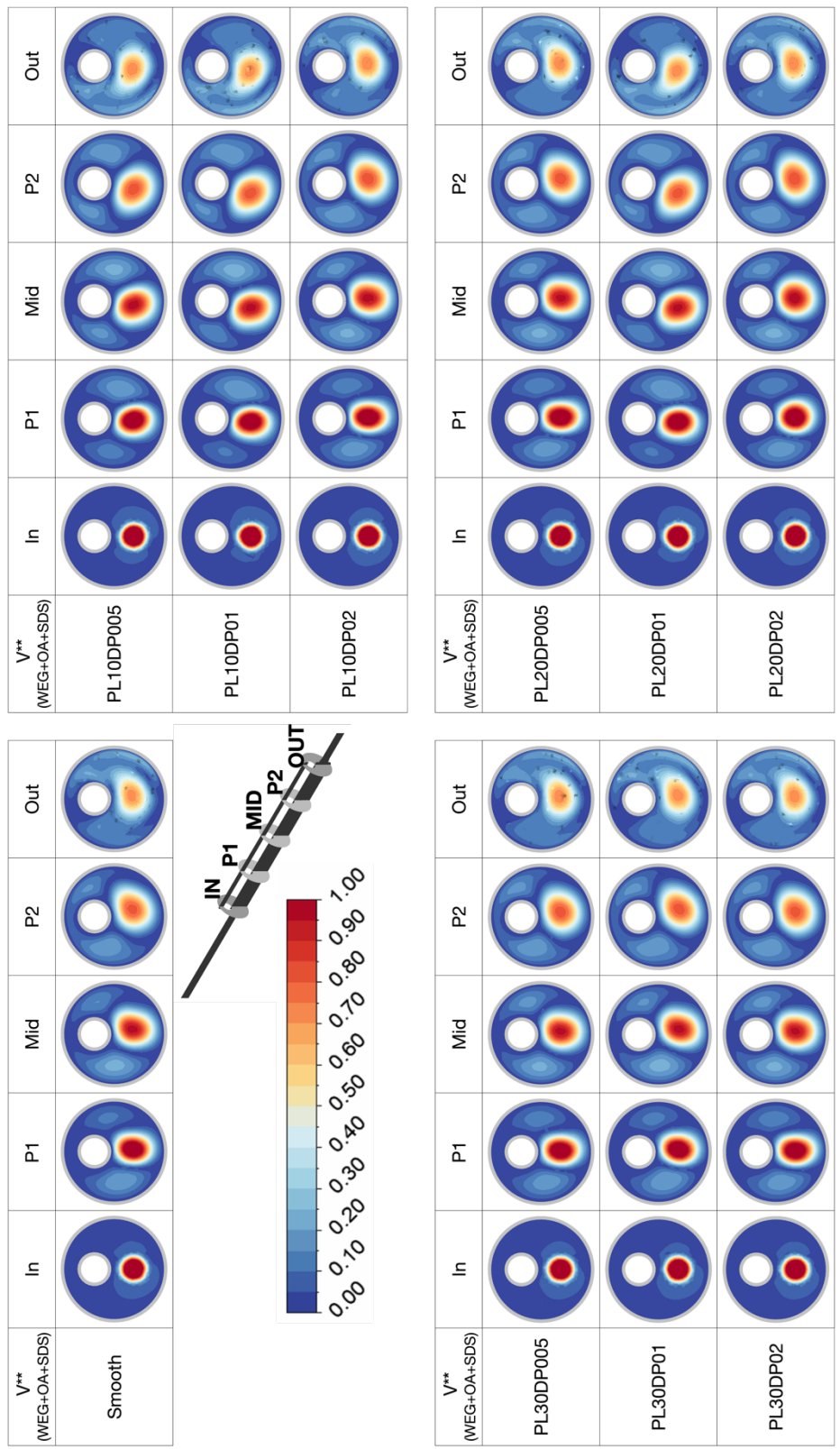
(b) Figure 5.13: (Continued)



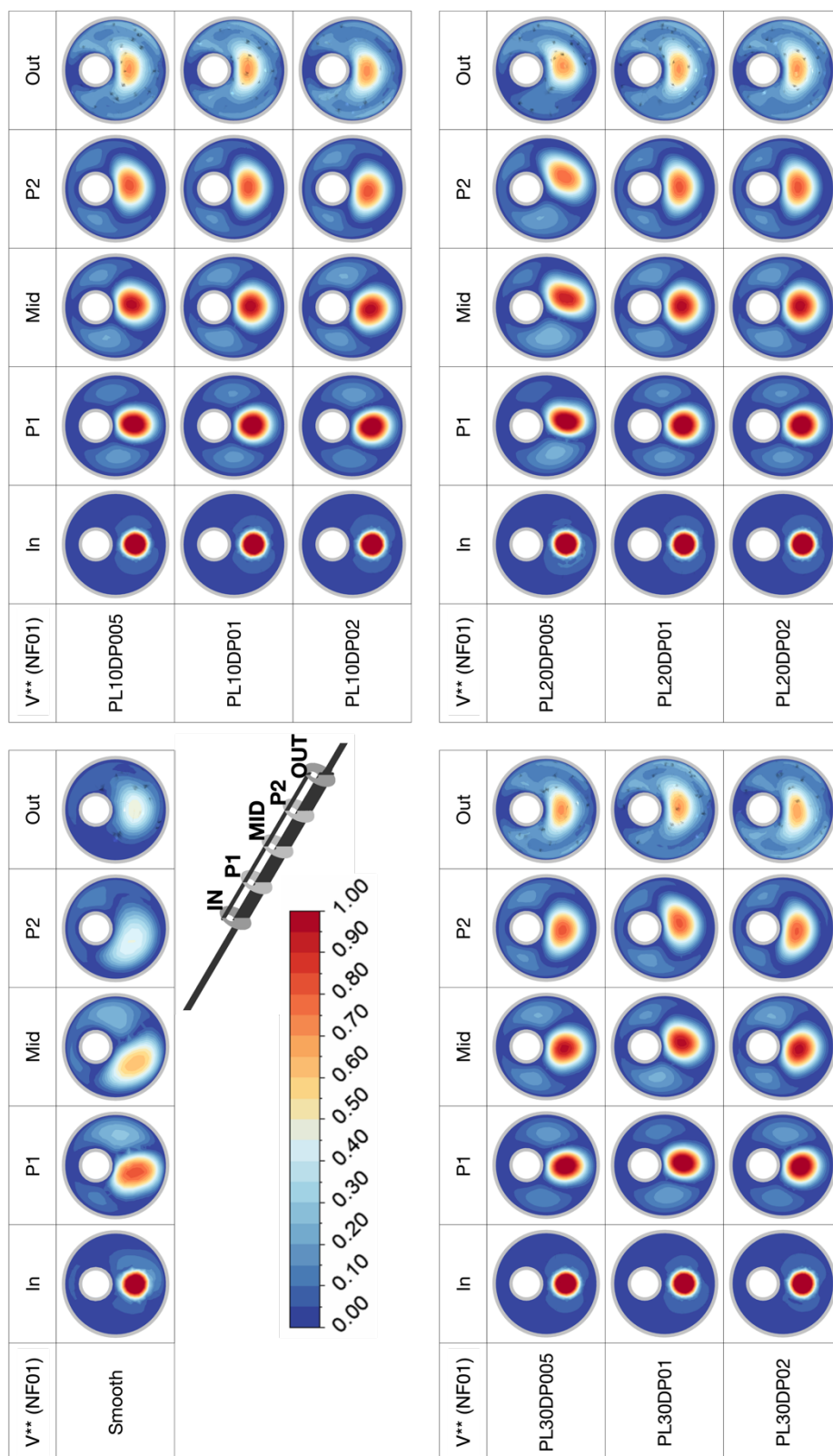
(c)
Figure 5.13: (Continued)



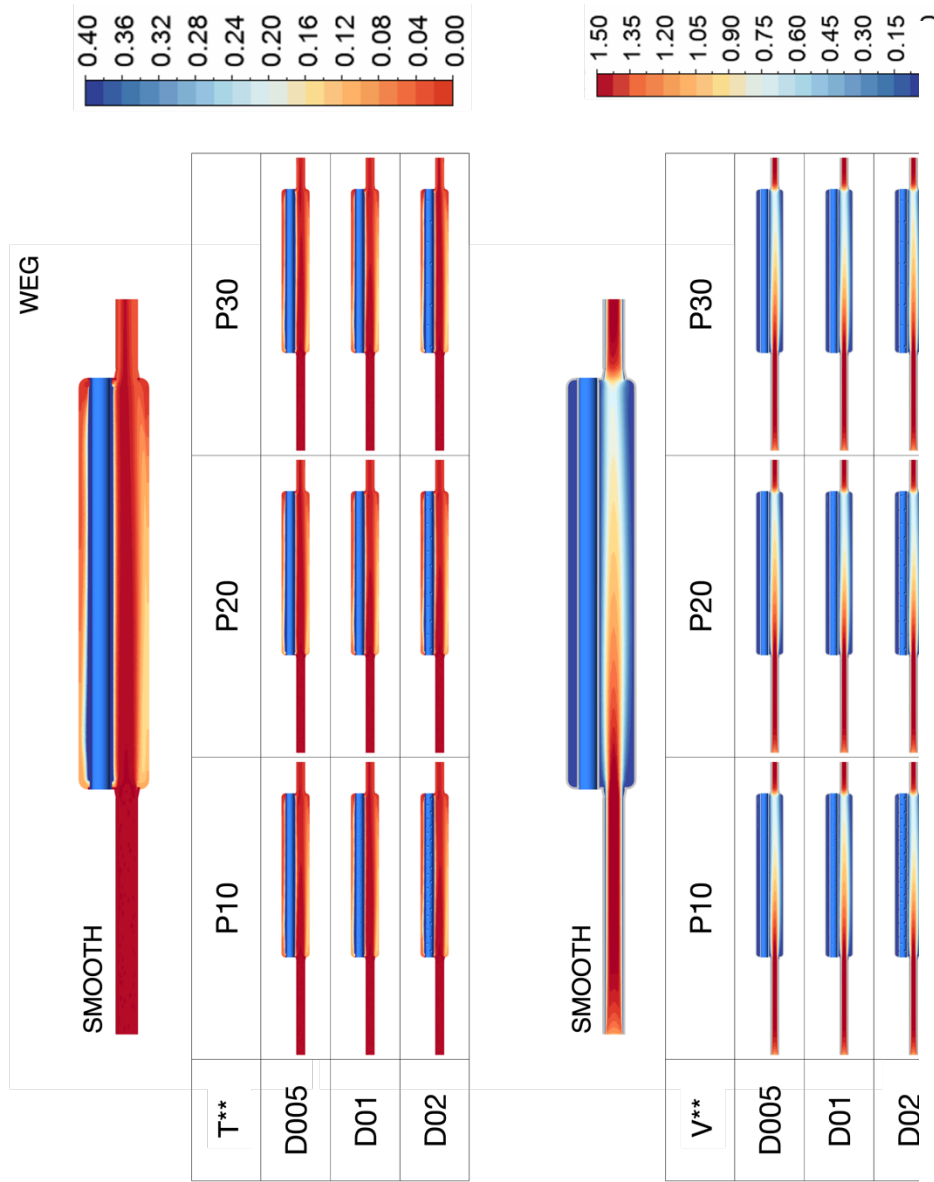
(a) Figure 5.14: V^{**} distributions at the critical cross-sections for (a) WEG, (b) WEG+OA+SDS and (c) NF01



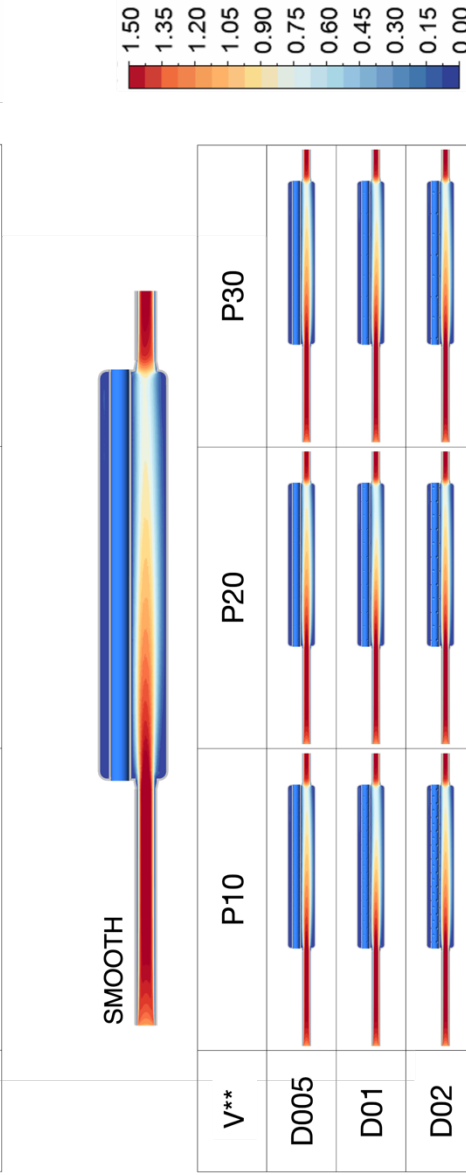
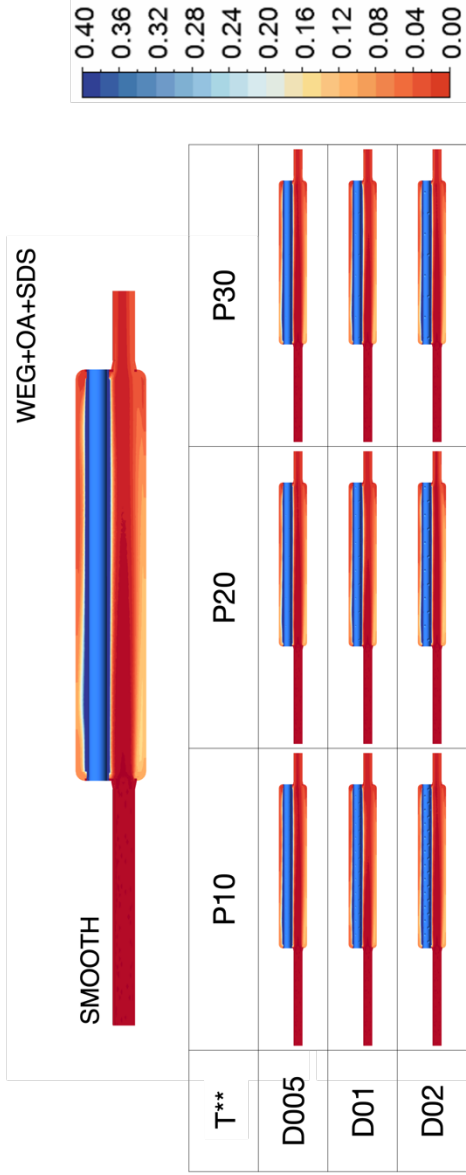
(b)
Figure 5.14: (Continued)

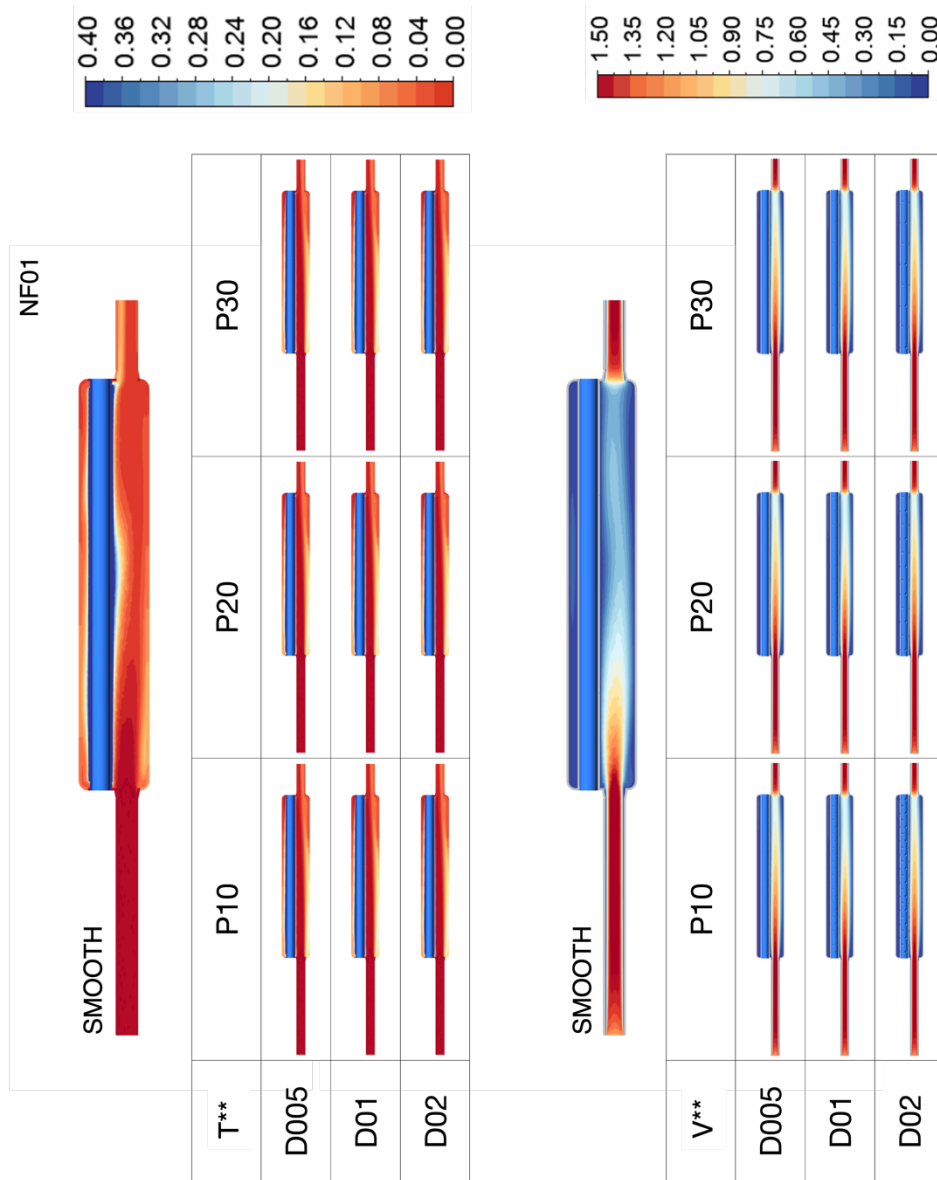


(c)
Figure 5.14: (Continued)



(a) Figure 5.15: Axial T^{**} and V^{**} distributions for (a) WEG, (b) WEG+AS+SDS, (c) NF01





(c)
Figure 5.15: (Continued)

Dimpled inner pipe results in a higher Δp penalty for all working fluids. Regardless of DP or PL, dimples behave as thermohydraulic cells which capture and trap the flowing working fluid. This leads to higher Δp values as shown in Figure 5.16. The addition of the dimples on the inner pipe surface in laminar flow conditions decreases the Nu for WEG+OA+SDS and NF01 up to 10% and 19%, respectively. Nu in the WEG case varies up to the upper and lower limits of 7% and 5%, respectively.

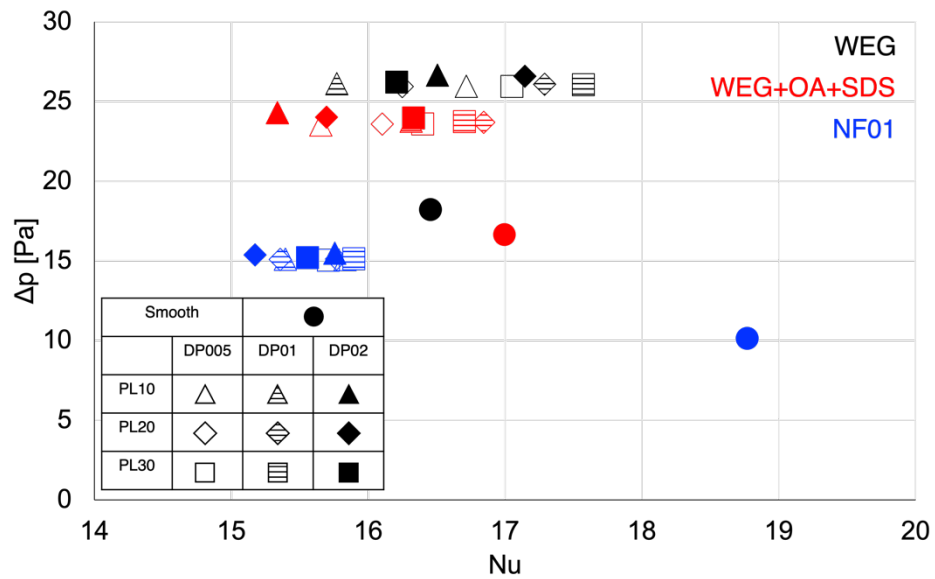


Figure 5.16: Pressure drop (Δp) and heat transfer (Nu) characteristics of DPHX

The effect of both working fluids and dimples on the performance of the DPHX was investigated by evaluating PEC values. PEC_1 defines the performance evaluation of the dimpled surface for each working fluid. In accordance with T^{**} and V^{**} values, ΔP and Nu , the addition of dimples decreases the PEC_1 values for all working fluids. Assuming the WEG+OA+SDS as a base fluid, the combination of nanofluids with dimpled surface technology also gives lower PEC_2 values as shown in Figure 5.17. Increment in Re for the NF01 in dimpled geometry (compared to smooth pipe) is more noticeable than in WEG and WEG+OA+SDS cases which is also shown in Figure 5.15.

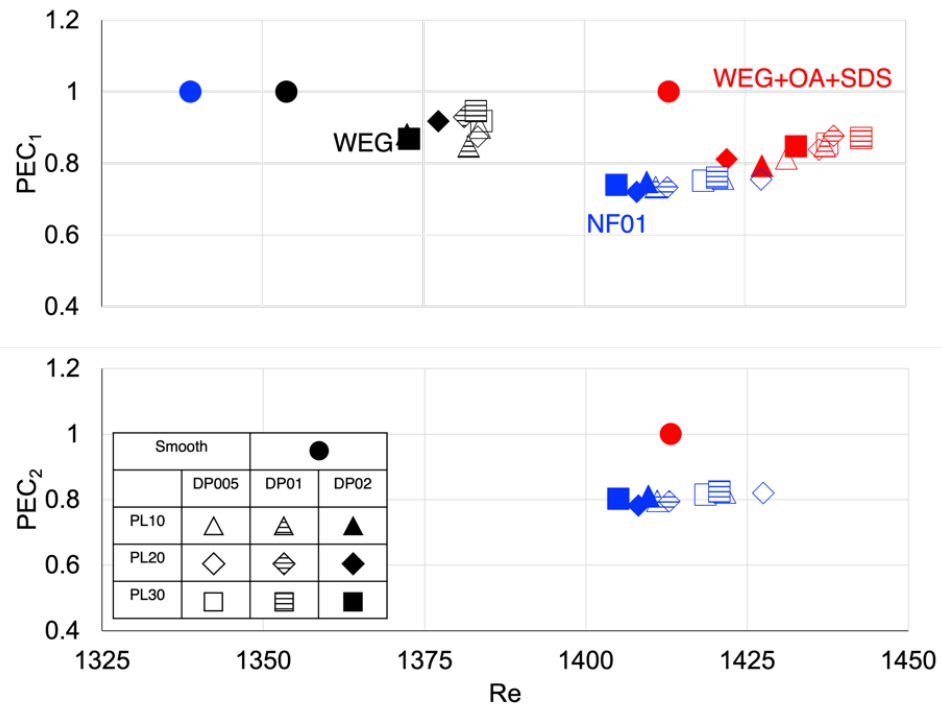


Figure 5.17: PEC_1 and PEC_2 values of DPHX.

5.3 Performance of SPNCmL with dimpled DPHX

5.3.1 The Effect of Eccentricity

Eccentricity is an important parameter affecting flow propagation and heat transfer. Here the eccentricity effect on the SPNCmL performance was investigated for two cases: E032 (the condition where maximum heat transfer was obtained in DPHX) and E054 (the design limitation of the industrial application). Figure 5.18 shows the change of temperatures (T_{\max} and ΔT_{heater}), and (c) effectiveness with a number of dimples which increases the decrease of pitch length. The addition of the dimples results in a decrease in temperatures, and thus effectiveness values in the system for both E032 and E054 cases. However, the eccentricity has no significant effect on the temperatures, unlike the dimpled surface technology.

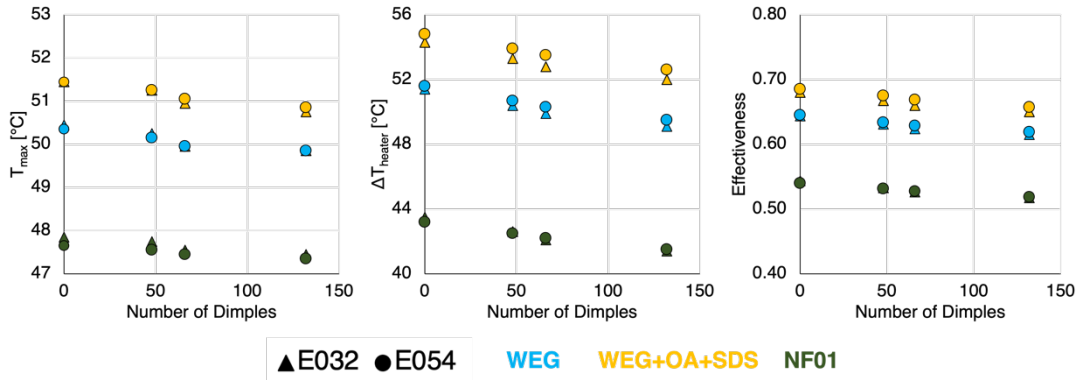


Figure 5.18: The change of temperatures (a) T_{max} and (b) ΔT_{heater} , and (c) effectiveness with number of dimples

Figure 5.19 presents the relationship of Nu for the cooling- and heating-ends with Ra for constant temperature boundary conditions. An increment in Nu and Ra have been seen for the decreasing viscosity values, and NF01 has the highest Nu and Ra for both ends. The addition of the dimples decreases the Nu, but it also results in a slight increase in Ra at the cooling-end. An increase in eccentricity increases the Nu at the cooling-end for WEG+OA+SDS case, which has the highest viscosity values in this temperature range, for both smooth and dimpled tube. The T^* distributions in Figures 20 also shows the reason behind this behaviour by cooler (more blue area) in the cooling-end of E054 case. However, it decreases the Nu of NF01 at the heating-end with no significant difference for dimpled tube. Therefore, higher Nu numbers of NF01 may show its potential in passive heat transfer systems.

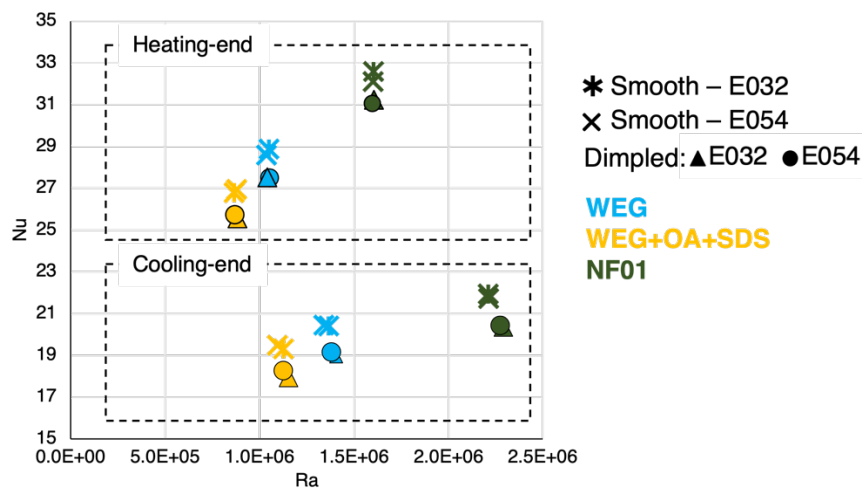
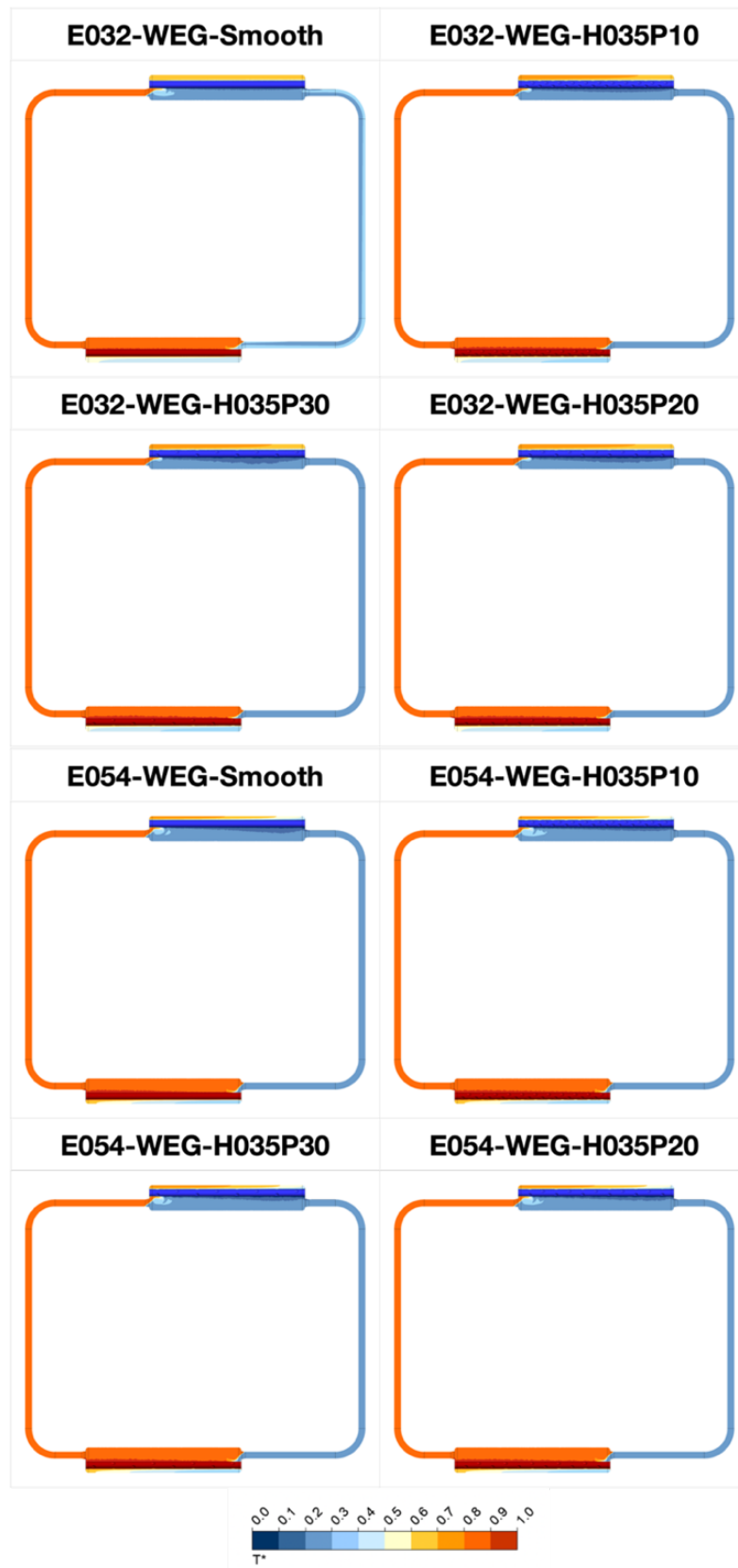


Figure 5.19: The change of Nu with Ra for different eccentricity values for smooth and P10 cases.

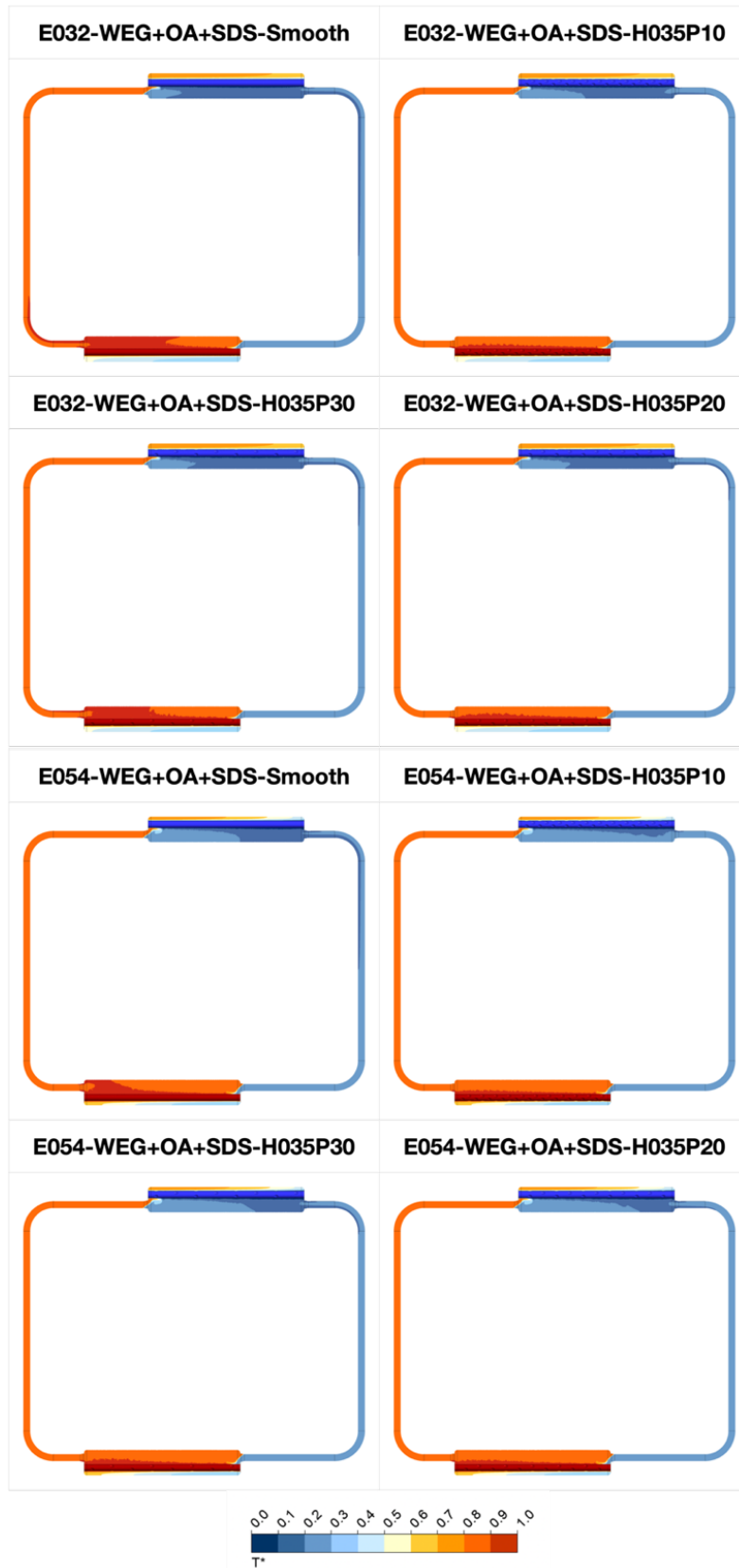
The T^* distributions at the SPNCmL system have been presented in Figure 5.20. The darker blue distribution of T^* indicates the cooler working fluid, and darker red T^* means the hotter working fluid. For the WEG, the addition of the dimples directs the working fluid through the bottom section of the annular section, and this results in a cooler working fluid layer under the inner pipe whereas hotter working fluid goes along the narrow section of the annular. Similar behavior is also observed for the heating-end. The hotter fluid layer is developed at the wider section of the annular pipe. The increase of the eccentricity decreases the fluid temperatures (lower T^* values) at the narrower section of the annular pipe at the cooling-end for both smooth and dimpled tubes. Moreover, the T^* values at the narrower section increase through the outlet of the heating-end. The effect of the viscosity on the T^* values can be seen from the smaller T^* values at the cooling-end and higher T^* values at the heating-end for WEG+OA+SDS compared to NF01 (lowest viscosity values).

Figure 5.21 and 5.22 shows the T^* distributions at the critical cross sections of the annular tube, namely, inlet, C1, C2, middle, C3, C4 and outlet. In order to show the effect of dimples, the T^* distributions are captured at the C1-4. C1 is the cross-section in which the second dimple group of P30 is located. C2, C3 and C4 are for the fourth, fifth and seventh groups of the P30 case. The effect of the dimples which have a pitch length of 20 mm is only visible in the middle section. For the cooling-end presented in Figure 5.20, utilization of the dimples prevents the movement of the cooler working fluid through the wider section of the annular tube with the eccentricity of E032. Although an increase of the eccentricity to 0.54 (E054) results in higher T^* values until the cross-section of C4, the cooler working fluid (smaller T^*) values are obtained at C4 and the outlet of the annular section. Moreover, a higher temperature gradient of T^* is observed for the working fluids with higher viscosity as WEG+OA+SDS and WEG. For the heating-end (Figure 5.22), NF01 has a smaller temperature gradient of T^* . Moreover, the increase in eccentricity increases the T^* values in the wider section of the annular tube.



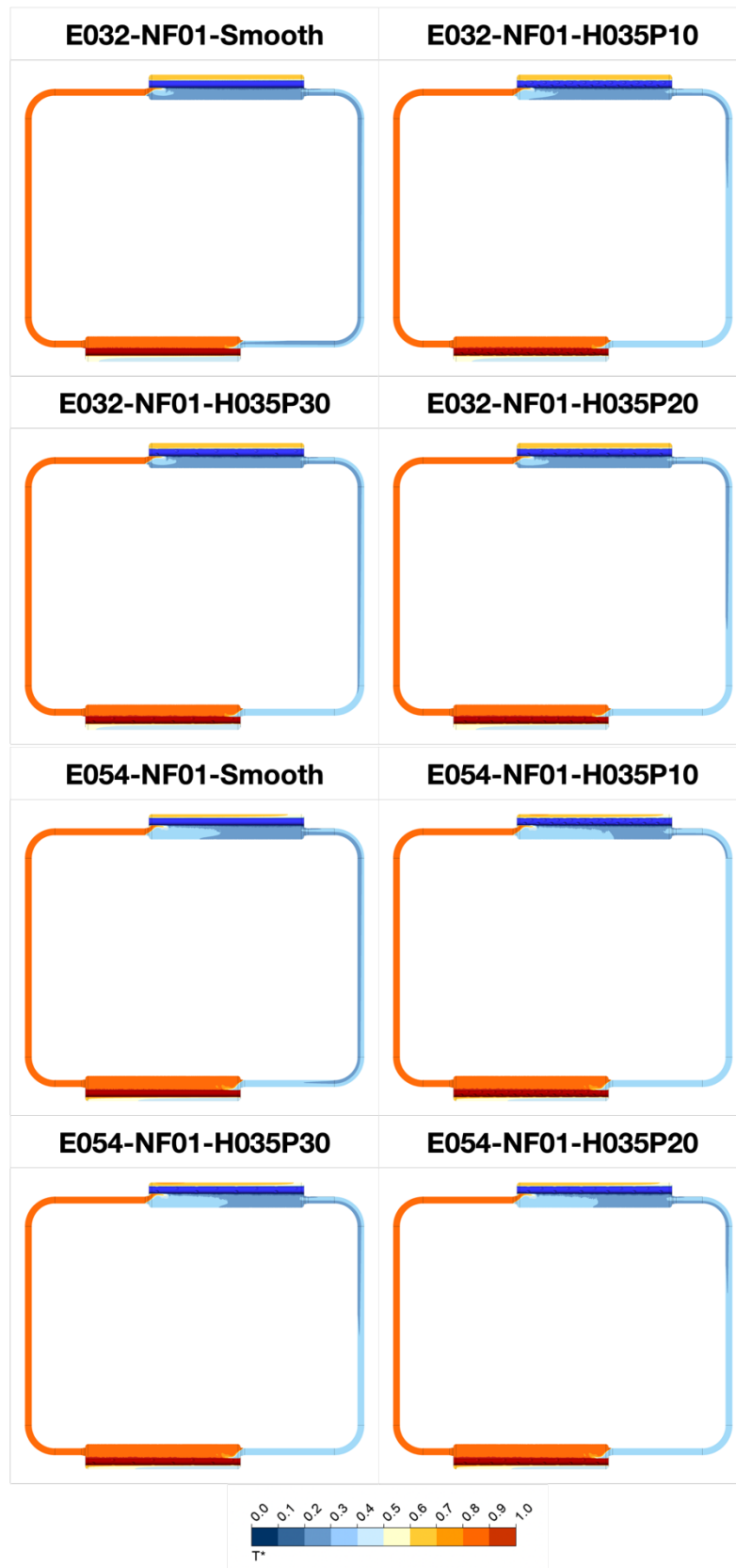
(a)

Figure 5.20: The axial T^* distribution for (a) WEG, (b) WEG+OA+SDS, (c) NF01



(b)

Figure 5.20: (Continued)



(c)

Figure 5.20: (Continued)

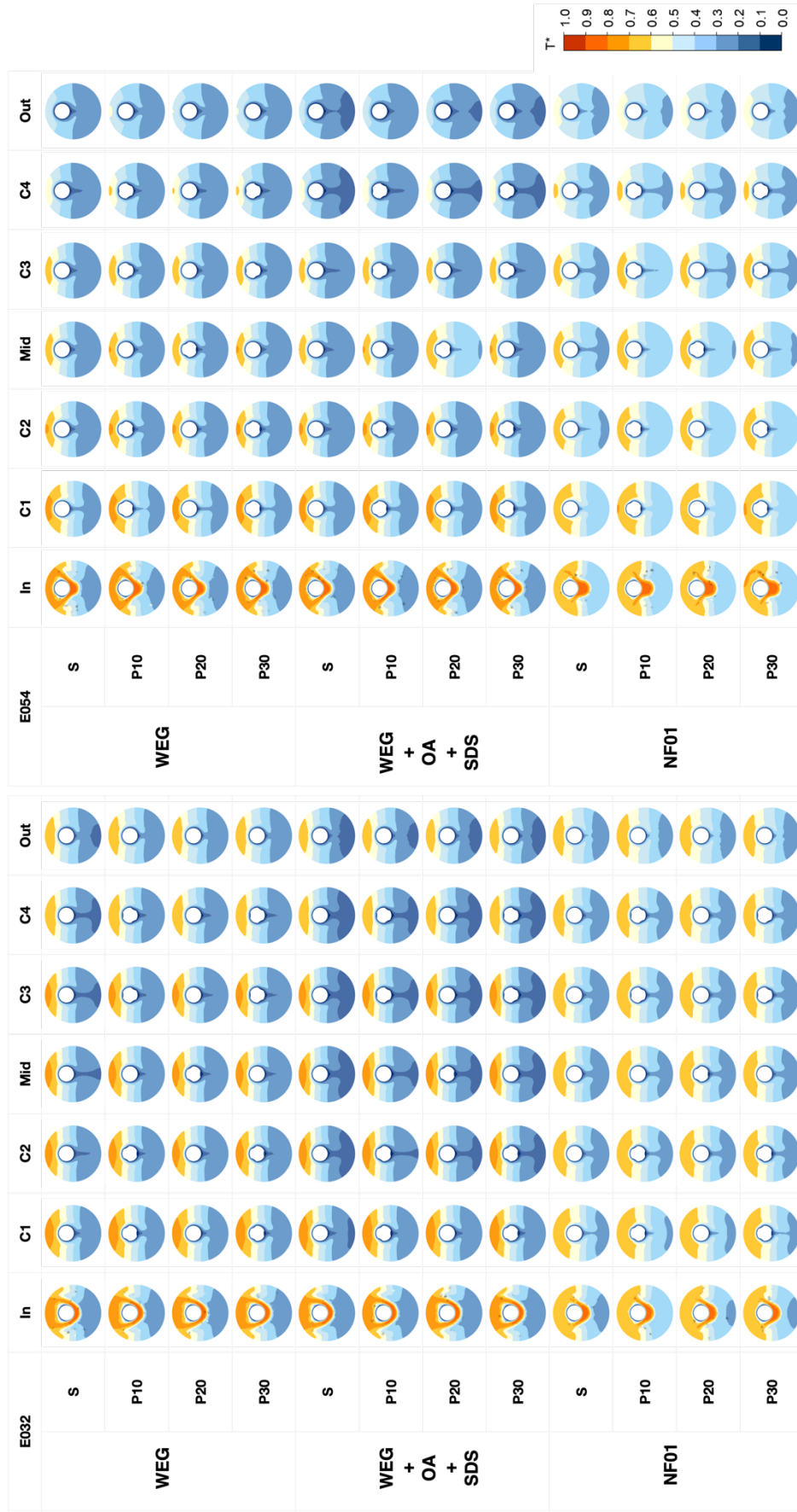


Figure 5.21: The T* distribution at cooling-end for different eccentricity values

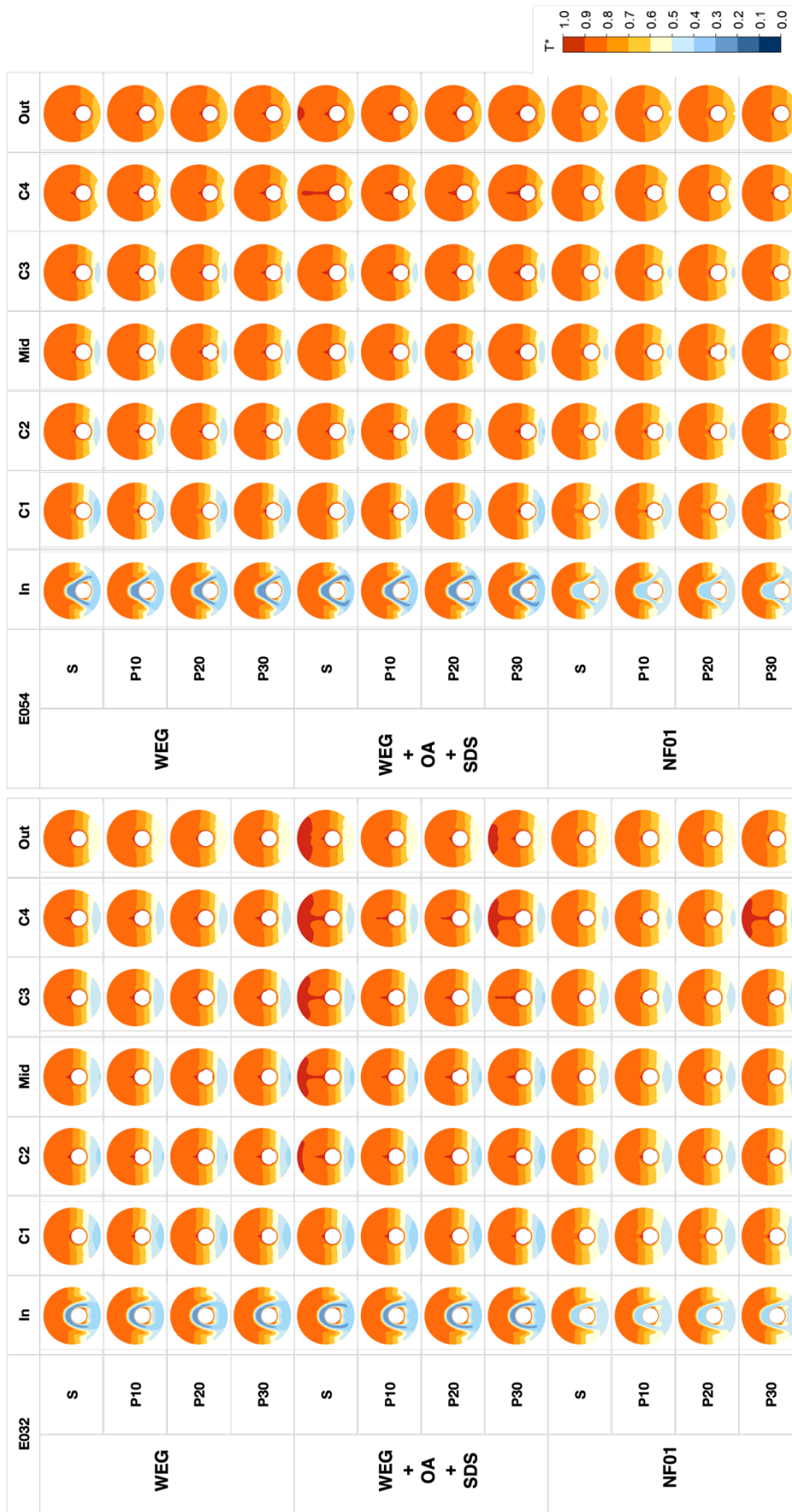


Figure 5.22: The T^* distribution at heating-end for different eccentricity values

Figure 5.23 shows the axial distribution of the V^* for different eccentricity values. Utilization of the dimpled surface technology results in tiny pockets of higher V^* values near the inner pipe and these also disturb the hydrodynamic layer in this region. In the case of WEG as a working fluid, these pockets are not clear at the cooling-end but they become more separated and visible at the heating-end as pitch length decreases. Increase of eccentricity to case of E054 makes the difference V^* layers more clear and increase the V^* in wider section of the smooth pipe. Contrary to E032, the case of E054 has these tiny pockets in also cooling-end. This behavior is observed for also NF01 and WEG+OA+SDS cases. However, as the viscosity decreases in NF01 case, the dimples create those pockets in cooling-end differently from the other cases. Moreover, V^* region with higher values is shifted near the inlet section at the narrow part of cooling-end in E032-NF01-H035P10 case.



(a)

Figure 5.23: The axial V^* distribution for (a) WEG, (b) WEG+OA+SDS, (c) NF01



(b)

Figure 5.23: (Continued)



(c)

Figure 5.23: (Continued)

Figure 5.24 shows that the eccentricity improves the Re at cooling- and heating-ends for all working fluids slightly. Because, as a result of higher eccentricity values, the temperature decreases at the cooling-end, in which the differences in viscosity values is more significant (Figure 3.10), and thus Reynolds number increases. Moreover, Re does not change with the addition of the dimples.

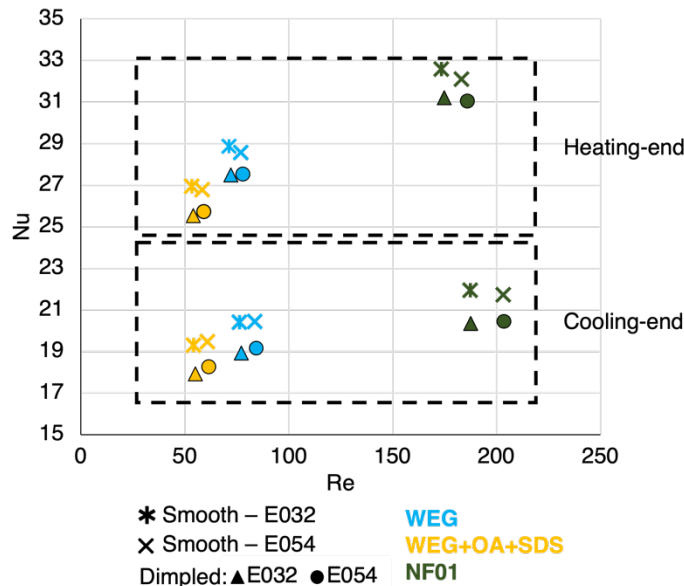


Figure 5.24: The change of Nu with Re for different eccentricity values for smooth and P10 cases.

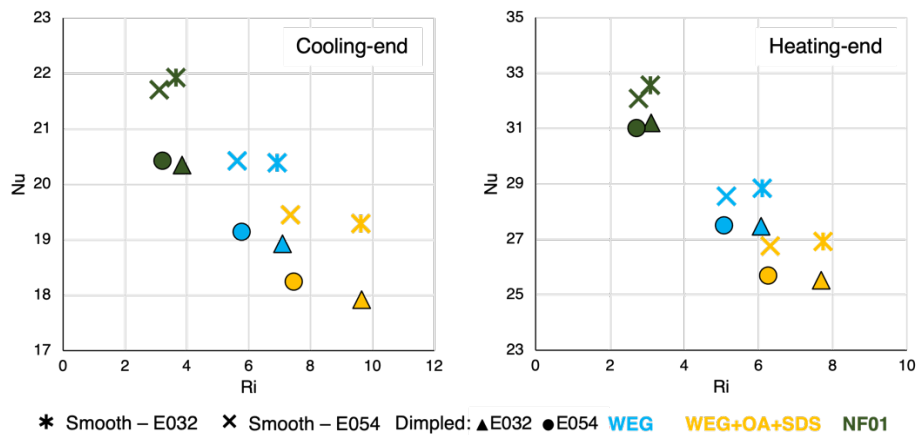


Figure 5.25: The change of Nu with Ri for different eccentricity values for smooth and P10 cases.

The change of the Nu with Ri, which defines the dominance of natural convection on forced convection, is presented in Figure 5.25. Although considerably higher Nu

numbers are observed for the E054, the E035 has higher Ri values. Moreover, the increasing viscosity (WEG+OA+SDS case) boosts the effect of eccentricity on Ri numbers.

5.3.2 The Effect of Dimple Height

Dimpled surface technology provides improved convective heat transfer by flow reattachment, flow impingement, and upwash flow at the downstream region of the dimples, but flow separation and recirculation in the upstream region of the dimples may be also the cause of reduction in heat transfer. Therefore, dimples' height is important to obtain heat transfer performance improvement.

Figure 5.26 presents how temperatures and effectiveness change with dimple height. The pre-defined dimple height by considering the ratio of the dimples' height and pipe diameter in the literature [60] to the present study is 0.35 mm. Although the increment percentage is relatively high (by 42%), the difference in the dimension is still tiny in the present study. So, this results in insignificant changes for both temperatures and effectiveness values. Regardless of the dimples' height, an increase in the number of dimples (reduction of the pitch length) decreases the ΔT_{heater} and thus, effectiveness value.

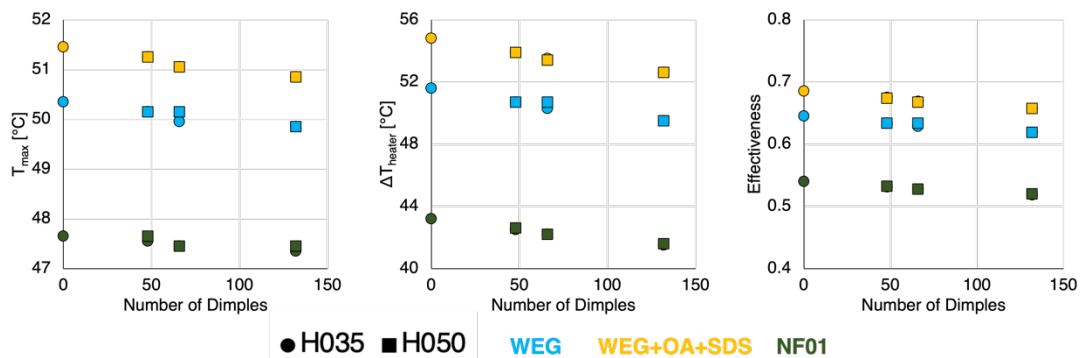


Figure 5.26: The change of temperatures (a) T_{max} and (b) ΔT_{heater} , and (c) effectiveness with number of dimples for different dimple heights

Considering the fact that the addition of the dimples does not affect Ra and decreases the Nu from Figure 5.19, the increasing dimples' height has also no effect on Ra as shown in Figure 5.27 for the heating-end. However, addition of the dimples results in slight increment in Ra for cooling-end because of the sharp reduction of the viscosity values in this temperature range. Moreover, this reduction also influences the Ri at the cooling-end in Figure 5.28. Although Ri does not change with the addition of the dimples, the tiny increase of the dimples' height results in slight reduction of the Ri at the cooling-end.

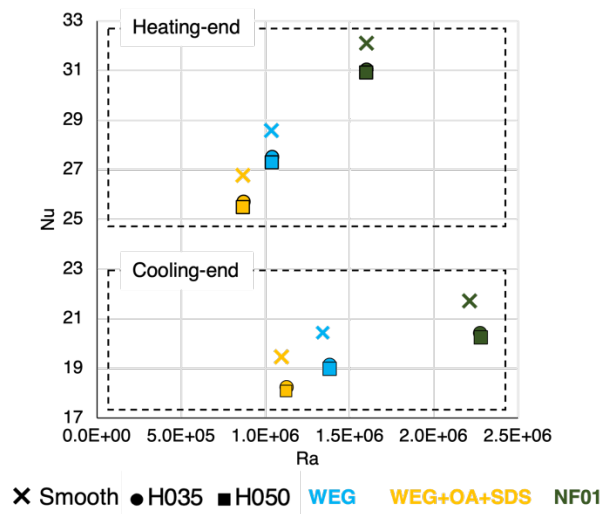


Figure 5.27: The change of Nu with Ra for different dimple heights at E054 for smooth and P10 cases.

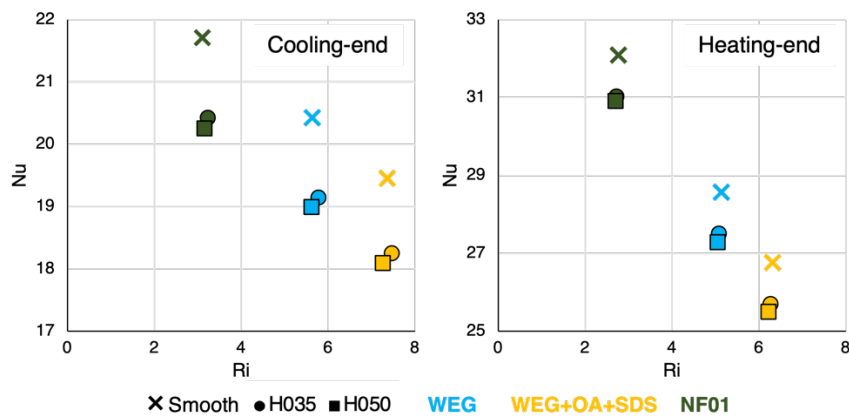


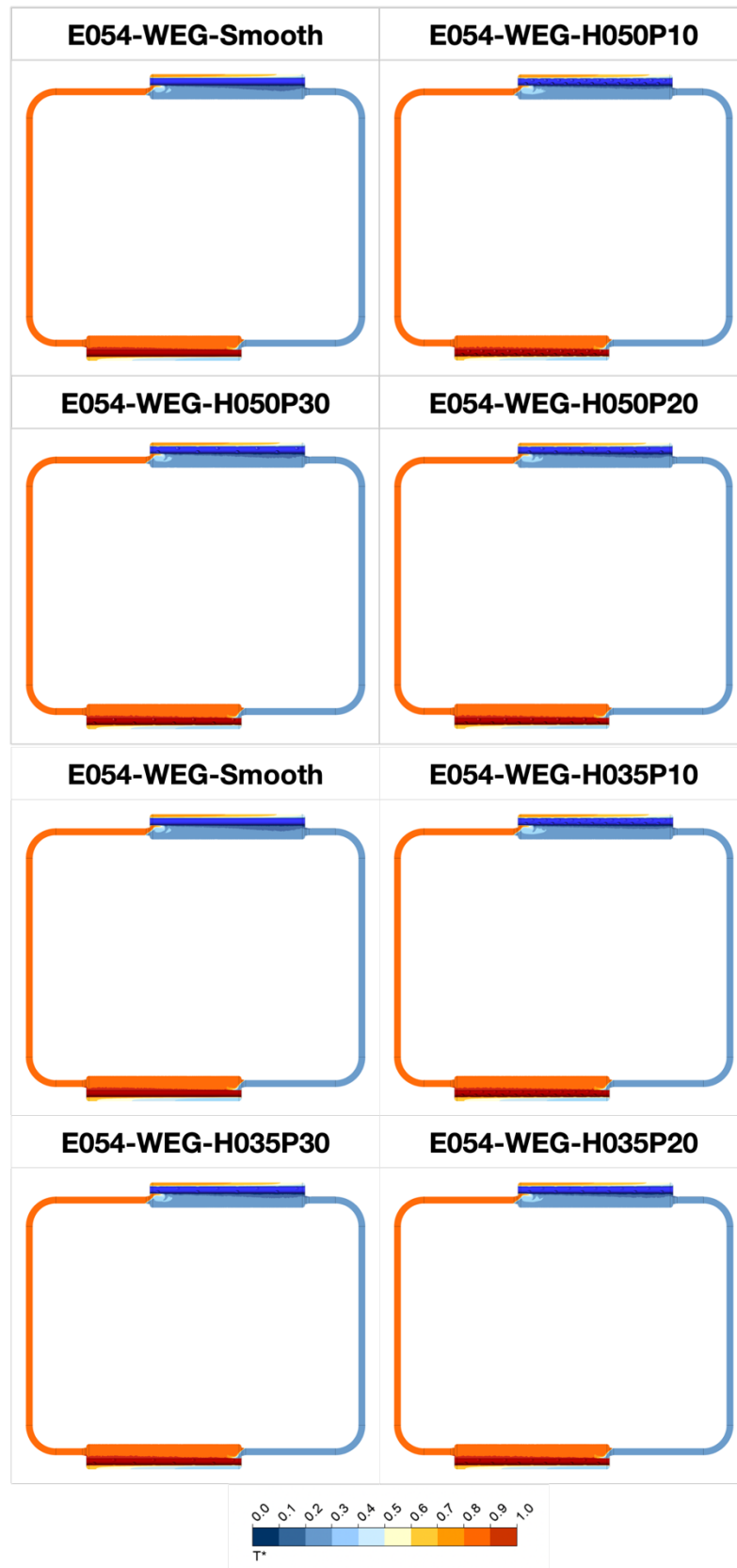
Figure 5.28: The change of Nu with Ri for different dimple heights at E054 for smooth and P10 cases.

Table 5.1 presents the effect of dimples' height the Nu and Re numbers at at cooling- and heating ends. Although addition of the dimples increases the surface area, but the form heat cells which captures the fluid instead creating turbulent boundary layer to improve heat transfer.

Table 5.1: The Nu and Re numbers for different dimples' heights at cooling- and heating ends

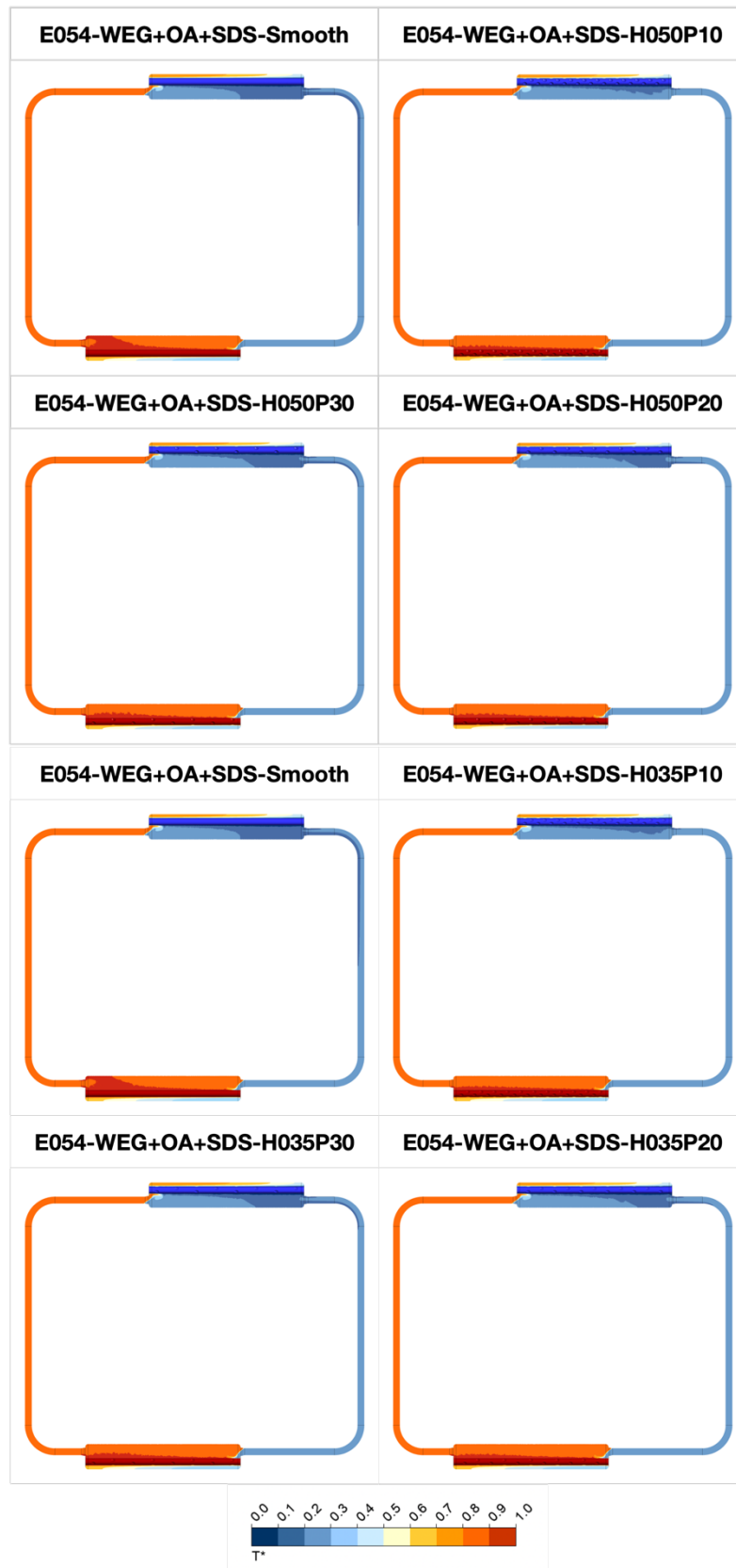
Cases	E054-H035				E054-H050			
	Nu _C	Nu _H	Re _C	Re _H	Nu _C	Nu _H	Re _C	Re _H
WEG-smooth	20.43	28.57	83.69	77.04	20.43	28.57	83.69	77.04
WEG+OA+SDS-smooth	19.46	26.77	60.94	58.47	19.46	26.77	60.94	58.47
NF01-smooth	21.72	32.09	203.25	183.14	21.72	32.09	203.25	183.14
WEG-P10	19.15	27.51	84.46	78.24	19.00	27.29	85.67	78.34
WEG-P20	19.66	27.76	83.58	77.52	19.63	27.80	85.10	77.92
WEG-P30	19.91	28.20	84.95	77.76	19.85	28.11	84.94	77.80
WEG+OA+SDS-P10	18.25	25.71	61.71	59.21	18.10	25.50	62.54	59.31
WEG+OA+SDS-P20	18.74	26.06	60.82	58.70	18.62	25.96	61.60	58.52
WEG+OA+SDS-P30	19.00	26.42	62.01	58.94	18.91	26.35	61.87	58.93
NF01-P10	20.43	31.03	203.75	186.26	20.26	30.92	206.57	186.99
NF01-P20	20.93	31.39	203.37	184.90	20.86	31.28	206.22	184.51
NF01-P30	21.23	31.79	203.86	185.46	21.16	31.81	205.74	185.48

Similar to observations in Figures 5.26-28, there is no significant change is seen for axial distributions of the T^* (Figure 5.29) and V^* (Figure 5.30), and the T^* distributions at the critical cross sections in Figures 5.31 and 5.32 for all working fluids and pitch lengths. Dimples behave as pockets or cells in which the flowing fluid is captured and resulting in a reduction of convective heat transfer. Lower T^* values around the inner pipe and at the dimples, and higher T^* values at the wider section of the annular pipe of the cooling-end depicture this behavior.



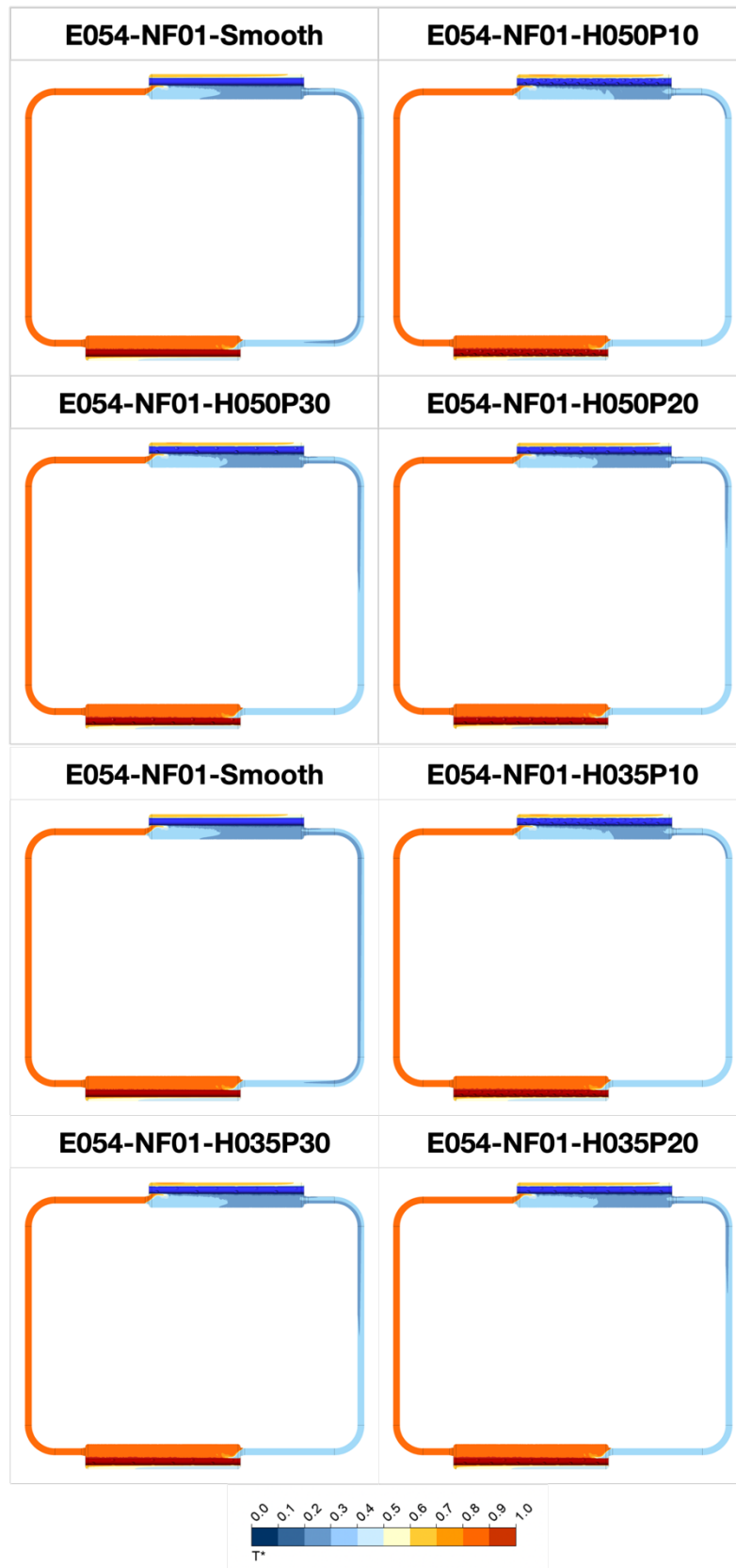
(a)

Figure 5.29: The axial T^* distribution of (a) WEG, (b) WEG+OA+SDS, (c) NF01 for different dimple heights



(b)

Figure 5.29: (Continued)



(c)

Figure 5.29: (Continued)



(a)

Figure 5.30: The axial V^* distribution of (a) WEG, (b) WEG+OA+SDS, (c) NF01 for different dimple heights



(b)

Figure 5.30: (Continued)



(c)

Figure 5.30: (Continued)

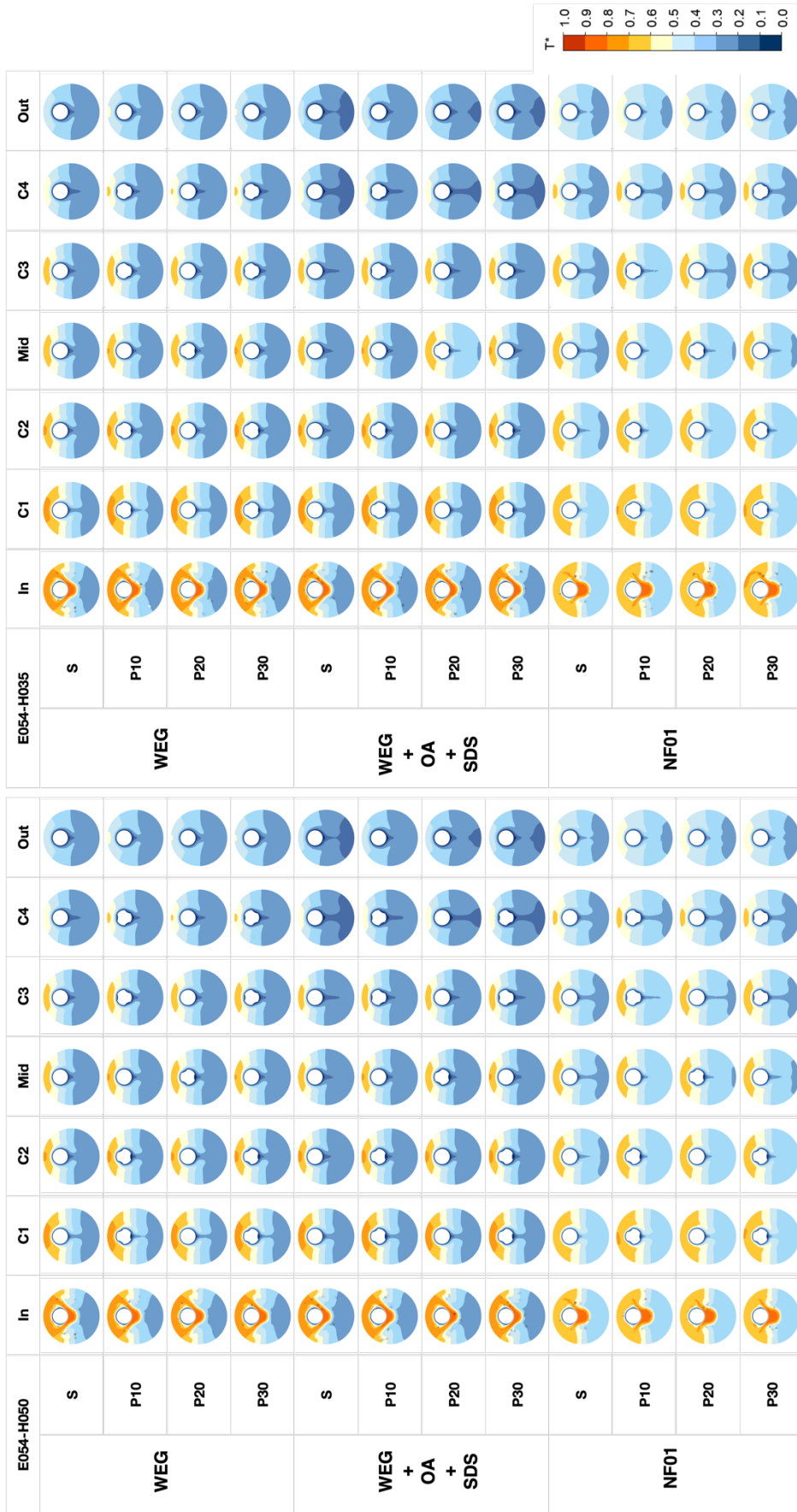


Figure 5.31: The T^* distribution at cooling-end for different dimple heights

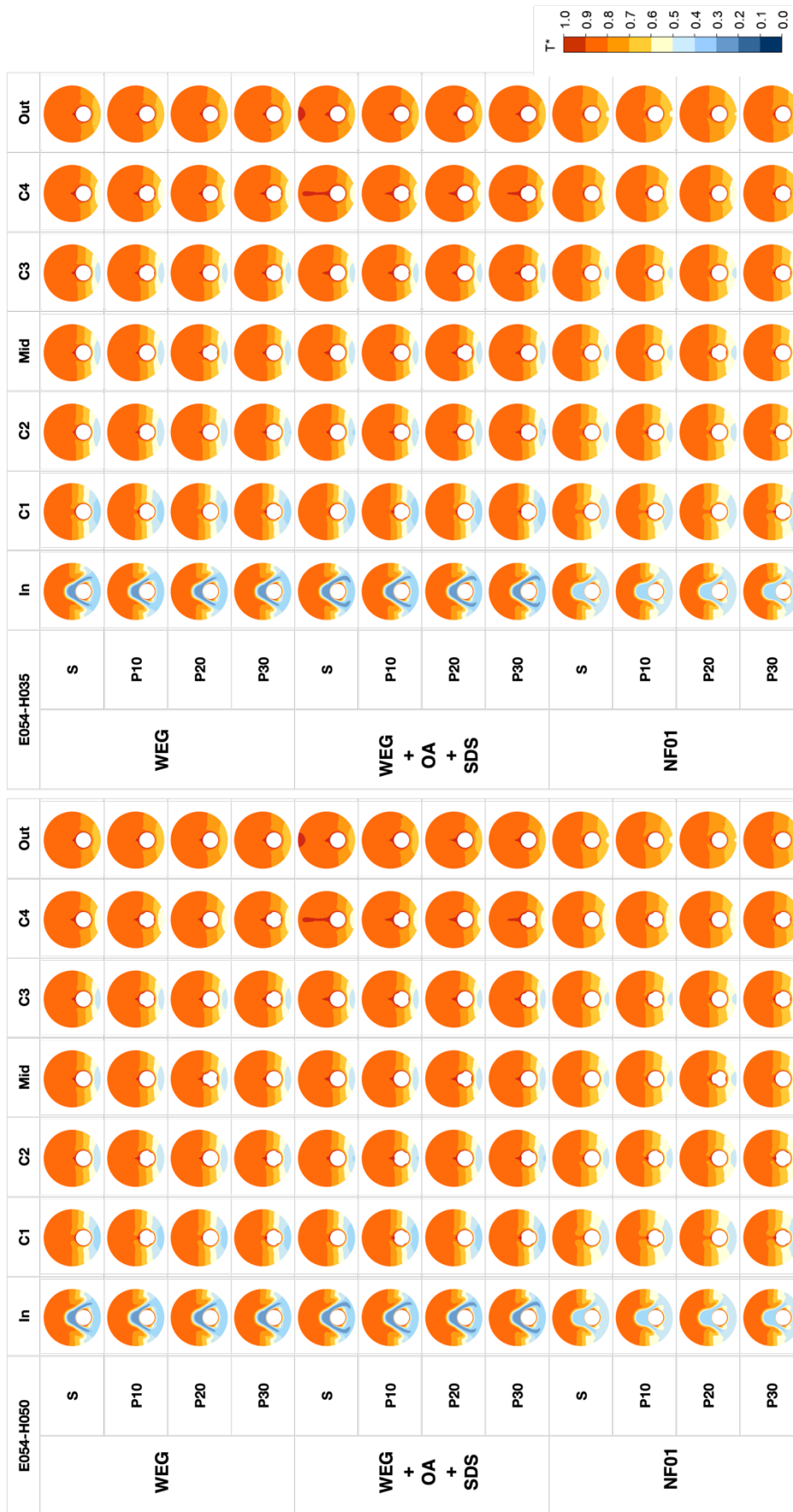


Figure 5.32: The T^* distribution at heating-end for different dimple heights

5.3.3 Local Heat Transfer Performance

Investigation of the local and average heat transfer coefficients for single-phase laminar flow in the SPNCmL's heating- and cooling-ends is important to understand and evaluate heat transfer performance of dimpled surface technology for different working fluids. The change of the local Nu number along the SPNCmL's heating- and cooling-ends (Gz^{-1} considering Reynolds and Prandtl numbers) was investigated for hydrodynamically and thermally developing flow to understand natural convection effects. Here, in Figures 5.33-35, Nu numbers have been found higher at the inlet section of the annular tubes at the cooling-end, and the local variation is considerably higher compared to Meyer and Everts [2] results which were obtained for circular pipe with a 4 mm inner pipe diameter and 8 kW/m² of constant heat flux (further information can be found in section 4.2.). Although the local heat transfer distribution in annulus has been studied widely in the existing literature, the main boundary conditions employed in this thesis (3B according to Feldman et al. [46]) has not been studied for these eccentricity and pipe diameter ratio values. Therefore, conducting a comparison with the literature is highly difficult. Because the entering fluid faces with a sudden reduction of the temperature at the cooling-end, the Nu number is higher at the inlet section. The higher values at the inlet section may be also cause of the partial inlet of the fluid from a tube with a smaller diameter (5.15 mm) through the annular section. However, at the heating-end, Nu numbers increases along the annular tube as temperature increases.

Figure 5.33 shows how the local Nu changes with eccentricity at both ends. Higher Nu numbers were obtained at the inlet section for higher eccentricity (E054) and the reason behind this is higher Gr_m numbers found at the inlet section. As the local T^* decreases along the annular tube, which means the working fluid gets cooler, the Nu number slightly increases, and it has peak values at the outlet because of the partial outlet from the annular section. The T^* and V^* distributions in Figures 5.20.a and 5.23.a support that behavior. In Figure 5.20.a, the lower T^* values at the heating-end inlet results in higher Nu number at Figure 5.33, and then it reduces as flow mixing. After that, as temperature increases, the Nu number increases along the heating-end. After the middle section, the higher temperature gradients in Figure 5.22 results in higher Nu numbers for lower

eccentricity values. Addition of the dimpled surface technology did not affect the local Nu number change significantly.

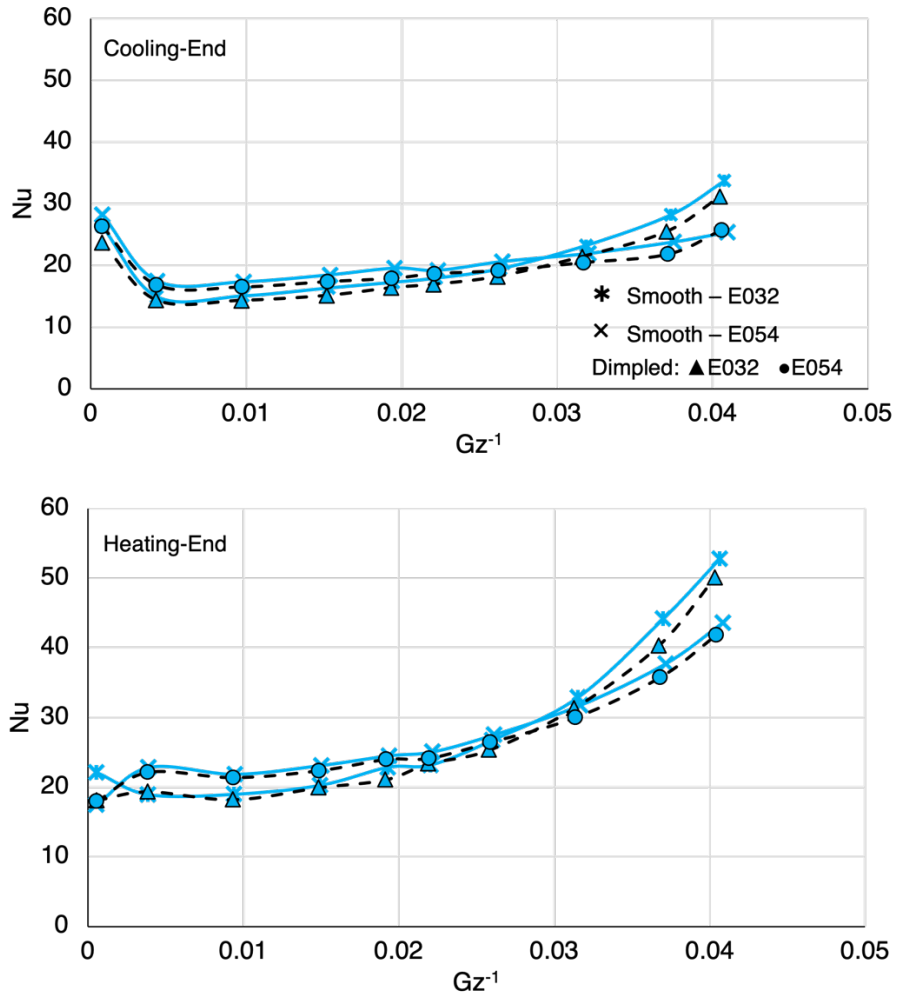


Figure 5.33: Local Nu distribution for different eccentricity values

Similar to overall Nu numbers at both ends (Table 5.1) as well as T^* and V^* distributions in Figures 5.29-32, local Nu numbers and thermal entry length did not change with the dimple heights in Figure 5.34.

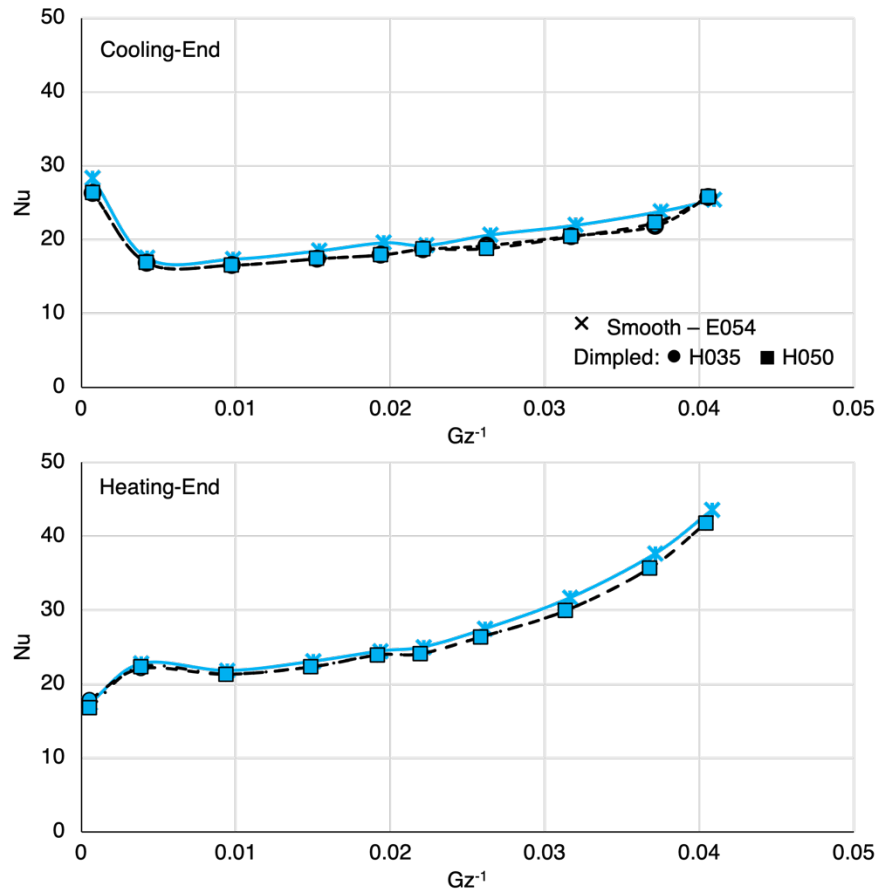


Figure 5.34: Local Nu distribution for different dimple heights

Figure 5.35 shows that nanofluids have higher Nu numbers the inlet section but WEG and WEG+OA+SDS has different trend as sudden increase of Nu numbers. This is a result of lower T^* values as well as smaller V^* values of NF01 case at the inlet of heating-end in Figure 5.29 and Figure 5.30, respectively. Higher Ra numbers associated with natural convection (and Grashof number) obtained for NF01 case results in higher Nu numbers, and this is more clear at the heating-end.

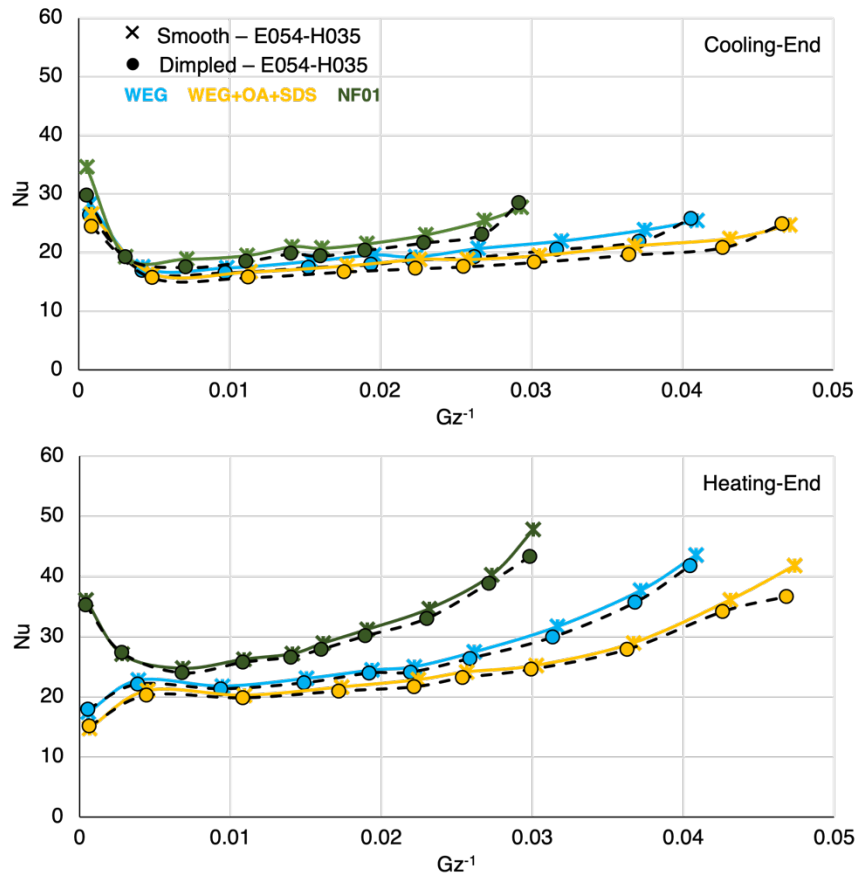


Figure 5.35: Local Nu distribution for different working fluids

5.3.4 The overall system performance

The overall system performance is defined by performance evaluation criteria (PEC) for choosing WEG+OA+SDS as a base fluid at the design parameters as the case of E054-H035-smooth. Figure 5.36 and Table 5.2 define the PEC values and pressure drop for investigated cases. Within the scope of working fluids, utilization of nanofluids decreases the pressure drop for both cooling- and heating-ends as well as increases the PEC value up to 1.75. Having lower viscosity values (Figure 3.10) is the main reason behind the reduction in this pressure drop. Higher Nu numbers and lower friction factors due to lower pressure drops in heating-end result in higher PEC values in this end.

The small pressure drop penalty of the dimpled surface technology has not been observed in this study. Therefore, the decreasing effect of the dimpled surface technology on Nu influences the PEC values directly. However, Table 5.2 shows that the SPNCmL working with the NF01 has still higher PEC values compared to base fluid even with dimpled tube.

Deeper dimples do not have any significant change of pressure drop but it reduces the PEC values slightly because of the Nu numbers. Within the scope of the eccentricity, tiny reduction of the pressure drop is observed with decreasing the eccentricity. The overall effect of smaller Nu number and pressure drops results in up to 8% lower values of PEC (WEG+OA+SDS case).

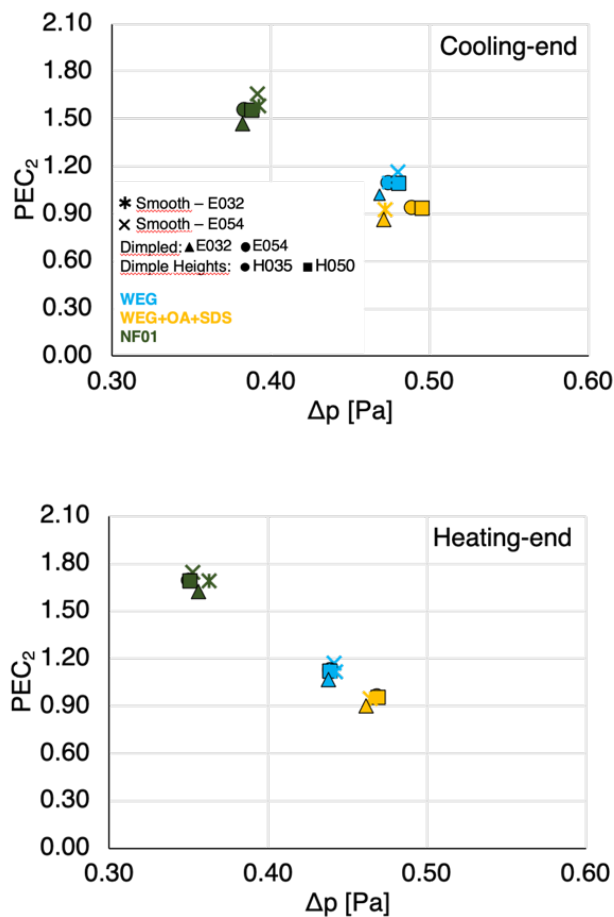


Figure 5.36: PEC_2 values for both ends

Table 5.2: The pressure drop and PEC values of all cases.

	Case	Δp_C	PEC _C	Δp_H	PEC _H
E054	WEG-smooth	0.48	1.17	0.44	1.17
	WEG-H035P30	0.48	1.14	0.44	1.16
	WEG-H035P20	0.47	1.12	0.44	1.14
	WEG-H035P10	0.47	1.10	0.44	1.13
	WEG+OA+SDS-smooth	0.49	1.00	0.47	1.00
	WEG+OA+SDS-H035P30	0.50	0.98	0.47	0.99
	WEG+OA+SDS -H035P20	0.49	0.96	0.47	0.97
	WEG+OA+SDS -H035P10	0.49	0.94	0.47	0.96
	NF01-smooth	0.39	1.66	0.35	1.75
	NF01-H035P30	0.39	1.62	0.35	1.74
	NF01-H035P20	0.39	1.60	0.35	1.71
	NF01-H035P10	0.38	1.56	0.35	1.70
	WEG-H050P30	0.48	1.14	0.44	1.15
	WEG-H050P20	0.48	1.13	0.44	1.14
	WEG-H050P10	0.48	1.09	0.44	1.12
	WEG+OA+SDS -H050P30	0.49	0.98	0.47	0.99
	WEG+OA+SDS -H050P20	0.49	0.96	0.47	0.97
	WEG+OA+SDS -H050P10	0.49	0.94	0.47	0.96
NF01-H050P30	0.39	1.62	0.35	1.74	
NF01-H050P20	0.39	1.60	0.35	1.70	
NF01-H050P10	0.39	1.55	0.35	1.69	
E032	WEG-smooth	0.47	1.10	0.44	1.12
	WEG-H035P30	0.47	1.07	0.44	1.10
	WEG-H035P20	0.47	1.04	0.44	1.07
	WEG-H035P10	0.47	1.02	0.44	1.07
	WEG+OA+SDS smooth	0.47	0.93	0.46	0.95
	WEG+OA+SDS -H035P30	0.47	0.90	0.46	0.94
	WEG+OA+SDS -H035P20	0.47	0.88	0.46	0.91
	WEG+OA+SDS -H035P10	0.47	0.86	0.46	0.90
	NF01-smooth	0.39	1.58	0.36	1.69
	NF01-H035P30	0.39	1.54	0.36	1.67
	NF01-H035P20	0.39	1.51	0.36	1.64
	NF01-H035P10	0.38	1.47	0.36	1.62

Chapter 6

Conclusions

In this thesis, a single-phase natural circulation mini loop (SPNCmL) with double pipe heat exchangers (DPHX) at heating and cooling-ends, has been proposed as an alternative to suction line heat exchangers. As a continuation work of an industrial project, in which the natural circulation loop provides a COP improvement of 8-9% for household chest freezer by itself experimentally, this study aims to numerically investigate the effect of nanofluid-based SPNCmL using dimpled DPHXs on the performance of the refrigeration cycle. The main conclusions of this thesis are given as follows:

- SPNCmL provides a COP improvement of 58% and 98% when its heating-end is located before the condenser or after the condenser at the high-pressure side. The amount of the maximum transferrable heat is found as 38 W for the case for both “C-in” and “C-out” at $T_2 = 70^\circ\text{C}$, $N=4500$ rpm and $LP/HP = 60/600$ kPa.
- Considering the higher effectiveness values for smaller pipe diameters, and insignificant change of effectiveness with AR but an increase of heat transfer capability with AR, the main geometry is decided to be having pipe diameter of 5.15 mm and AR of 0.8 as a result of the preliminary study.
- Although increasing eccentricity causes a reduction of the heat transfer in DPHX located at the suction-line, eccentricity directs the fluid flow at the upper section of the annuli which results in the mixing of the warm and cold fluid pockets after the middle section. Even the movement of the inner pipe 2 mm upper (changing from eccentricity 0.32 to 0.69) has a huge effect on the heat transfer such reduction of 15%. However, the wider T^* distribution with higher values is also observed for cases of E032, E039, E054 and E061 in which heat transfer reduces

by 6% for E061 compared to E032. Moreover, the Nusselt number decreases with increasing eccentricity.

- Utilization of nanofluids requires a longer time to reach steady-state conditions, a heat transfer improvement of up to 13.6% WEG+OA+SDS as a base fluid has been observed. Although the highest transferred heat was observed for the NF01 case, NF001 has the smallest pressure drop value with the highest PEC value. The results show that nanofluids improved the heat transfer at the suction-line of the refrigeration system.
- For the DPHX in the suction-line, the dimpled inner pipe of the annular flow results in a higher Δp penalty for all working fluids. Regardless of dimple diameter and pitch length, dimples behave as thermohydraulic cells which capture and trap the flowing working fluid. Moreover, dimpled surface technology on the inner pipe surface in laminar flow conditions decreases the Nu for WEG+OA+SDS and NF01 up to 10% and 19%, respectively.
- For the overall SPNCmL analysis, an increasing number of the dimples with decreasing pitch length results in lower Nusselt numbers for both cooling- and heating-ends. Moreover, a reduction in eccentricity also decreases the PEC values with tiny reduction in pressure drops. The dimples' height has no significant effect on the pressure drop in SPNCmL but decreases the PEC values slightly.
- Because of the temperature-dependent viscosity values of WEG-based working fluids, Nusselt numbers in the cooling-end has lower viscosity values compared to the heating-end. Utilization of nanofluids decreases the pressure drop for both cooling- and heating-ends as well as increases the PEC value up to 1.75.

References

- [1] Çobanoğlu N, Koca HD, Genç AM, Karadeniz ZH, Ekren O. Investigation of performance improvement of a household freezer by using natural circulation loop. *Science and Technology for the Built Environment*. 2021;27(1):85–97. doi.org:10.1080/23744731.2020.1798710
- [2] Meyer JP, Everts M. Single-phase mixed convection of developing and fully developed flow in smooth horizontal circular tubes in the laminar and transitional flow regimes. *International Journal of Heat and Mass Transfer*. 2018;117:1251–73. doi.org: 0.1016/j.ijheatmasstransfer.2017.10.070
- [3] Bozkır SC, Çobanoğlu N, Doğanay S, Karadeniz ZH, Elçioğlu EB, Turgut A. Investigation of external magnetic field effect on the performance of ferrofluid-based single-phase natural circulation loops. *Thermal Science and Engineering Progress*. 2023; 42: 101921. doi.org:10.1016/j.tsep.2023.101921
- [4] Çobanoğlu N, Banisharif A, Estellé P, Karadeniz ZH. The Developing Flow Characteristics of Water - Ethylene Glycol Mixture based Fe₃O₄ Nanofluids in Eccentric Annular Ducts in Low Temperature Applications. *International Journal of Thermofluids*. 2022; 100149. doi.org:10.1016/j.ijft.2022.100149
- [5] Manglik R, Fang P. Effect of eccentricity and thermal boundary conditions on laminar fully developed flow in annular ducts. *International journal of heat and fluid flow*. 1995;16(4):298–306. doi.org:10.1016/0142-727X(95)00030-T
- [6] International Energy Agency. *World Energy Outlook 2022* [Internet]. Paris; 2022 [date accessed 13.06.2023]. <https://www.iea.org/reports/world-energy-outlook-2022>.
- [7] International Energy Agency. *Appliances and Equipment*. Paris; 2022 [date accessed 13.06.2023]. <https://www.iea.org/reports/appliances-and-equipment>.
- [8] Belman-Flores JM, Barroso-Maldonado JM, Rodríguez-Muñoz AP, Camacho-Vázquez G. Enhancements in domestic refrigeration, approaching a sustainable

- refrigerator—a review. *Renewable and Sustainable Energy Reviews*. 2015; 51: 955–68. doi.org:10.1016/j.rser.2015.07.003
- [9] Kemna R, van Holsteijn F, Lee P, Sims E. Preparatory/review study on Commission Regulation (EC) No. 643/2009 and Commission Delegated Regulation (EU) No. 1060/2010 – complementary research on optimal food storage conditions in refrigeration appliances. 2017.
- [10] International Energy Agency. Final energy use for residential refrigerators and freezers covered by mandatory minimum energy performance standards. Paris; 2021 [date accessed 13.06.2023]. <https://prod.iea.org/data-and-statistics/charts/final-energy-use-for-residential-refrigerators-and-freezers-covered-by-mandatory-minimum-energy-performance-standards-2000-2021>
- [11] Ekren O. Refrigeration System: Capacity Modulation Methods. Ed.: Ekren O. Refrigeration. IntechOpen; 2017. 119–43. doi.org:10.5772/intechopen.70433
- [12] Thiessen S, Knabben FT, Melo C, Gonçalves JM. A study on the effectiveness of applying vacuum insulation panels in domestic refrigerators. *International Journal of Refrigeration*. 2018; 96: 10–16. doi.org:10.1016/j.ijrefrig.2018.09.006
- [13] Joybari MM, Haghghat F, Moffat J, Sra P. Heat and cold storage using phase change materials in domestic refrigeration systems: The state-of-the-art review. *Energy and Buildings*. 2015;1 06: 111–124. doi.org:10.1016/j.enbuild.2015.06.016
- [14] Patil N, Pathak D, Sahasrabudhe S. A novel refrigerator for smart city. 2018 International Conference on Smart City and Emerging Technology (ICSCET); 2018 Jan 5; India. IEEE; 2018. 1–4. doi.org:10.1109/ICSCET.2018.8537379.
- [15] Klein SA, Reindl DT, Brownell K. Refrigeration system performance using liquid-suction heat exchangers. *International Journal of Refrigeration*. 2000; 23(8): 588–96. doi.org: 10.1016/S0140-7007(00)00008-6
- [16] Martínez-Ballester S, Bardoulet L, Pisano A, Corberán JM. Visualization of refrigerant flow at the capillary tube inlet of a high-efficiency household

- refrigerator. *International Journal of Refrigeration*. 2017; 73: 200–8. doi.org:10.1016/j.ijrefrig.2016.09.019
- [17] Aprea C, Greco A, Maiorino A, Masselli C. The drop-in of HFC134a with HFO1234ze in a household refrigerator. *International Journal of Thermal Sciences*. 2018; 127: 117–25. doi.org:10.1016/j.ijthermalsci.2018.01.026
- [18] Rai SK, Dutta G. A Review of Recent Applications of Supercritical Fluid in Natural Circulation Loops For Nuclear Reactor. *International Journal of Applied Engineering Research*. 2018; 23(9): 195–204.
- [19] Basu DN, Bhattacharyya S, Das PK. A review of modern advances in analyses and applications of single-phase natural circulation loop in nuclear thermal hydraulics. *Nuclear Engineering and Design*. 2014; 280: 326–348. doi.org:10.1016/j.nucengdes.2014.09.011
- [20] Çobanoğlu N, Karadeniz ZH, Turgut A. Nanofluid-Based Single-Phase Natural Circulation Loops. Ed.: Subramanian K, Rao T, Balakrishnan A. *Nanofluids and Their Engineering Applications*. CRC Press; 2019. 59–76. doi.org:10.1201/9780429468223-4
- [21] Misale M, Garibaldi P, Passos JC, De Bitencourt GG. Experiments in a single-phase natural circulation mini-loop. *Experimental Thermal and Fluid Science*. 2007; 31(8): 1111–1120. doi.org:10.1016/j.expthermflusci.2006.11.004
- [22] Choi SUS, Eastman JA. Enhancing thermal conductivity of fluids with nanoparticles. *ASME International Mechanical Engineering Congress & Exposition*; 1995 Nov 12-17.
- [23] Nayak AK, Gartia MR, Vijayan PK. An experimental investigation of single-phase natural circulation behavior in a rectangular loop with Al₂O₃ nanofluids. *Experimental Thermal and Fluid Science*. 2008; 33(1): 184–9. doi.org:10.1016/j.expthermflusci.2008.07.017
- [24] Thomas S, Sobhan CB. Stability and Transient Performance of Vertical Heater Vertical Cooler Natural Circulation Loops with Metal Oxide Nanoparticle

- Suspensions. *Heat Transfer Engineering*. 2018; 39(10): 861–73. doi.org:10.1080/01457632.2017.1338859
- [25] Bejjam RB, Kumar K, Balasubramanian K. Experimental Studies on Nanofluid-Based Rectangular Natural Circulation Loop. *Journal of Thermal Science and Engineering Applications*. 2019; 11(4): 41006. doi.org:10.1115/1.4043760
- [26] Tlili I, Seyyedi SM, Dogonchi A, Hashemi-Tilehnoee M, Ganji D. Analysis of a single-phase natural circulation loop with hybrid-nanofluid. *International Communications in Heat and Mass Transfer*. 2020; 112: 104498. doi.org:10.1016/j.icheatmasstransfer.2020.104498
- [27] Nayak AK, Gartia MR, Vijayan PK. Thermal–hydraulic characteristics of a single-phase natural circulation loop with water and Al₂O₃ nanofluids. *Nuclear Engineering and Design*. 2009; 239(3): 526–40. doi.org:10.1016/j.nucengdes.2008.11.014
- [28] Misale M, Devia F, Garibaldi P. Experiments with Al₂O₃ nanofluid in a single-phase natural circulation mini-loop: Preliminary results. *Applied Thermal Engineering*. 2012; 40: 64–70. doi.org:10.1016/j.applthermaleng.2012.01.053
- [29] Turgut A, Doganay S. Thermal performance of a single phase natural circulation mini loop working with nanofluid. *High Temperatures–High Pressures*. 2014;43(4).
- [30] Doganay S, Turgut A. Enhanced effectiveness of nanofluid based natural circulation mini loop. *Applied Thermal Engineering*. 2015; 75: 669–76. doi.org:10.1016/j.applthermaleng.2014.10.083
- [31] Karadeniz ZH, Doganay S, Turgut A. Numerical Study On Nanofluid Based Single Phase Natural Circulation Mini Loops. In: *Proceedings of CONV-14: International Symposium on Convective Heat and Mass Transfer*; 2014 June 8-13; Turkey. Begel House Inc.; 2014. 575-584 doi.org:10.1615/ICHMT.2014.IntSympConvHeatMassTransf

- [32] Karadeniz ZH, Doganay S, Turgut A. Numerical study on nanofluid based single phase natural circulation mini loops: A steady 3D approach. *High Temperatures–High Pressures*. 2016; 45(4): 321-335.
- [33] Koca HD, Doganay S, Turgut A. Thermal characteristics and performance of Ag-water nanofluid: Application to natural circulation loops. *Energy Conversion and Management*. 2017; 135: 9–20. doi.org:10.1016/j.enconman.2016.12.058
- [34] Mohammad AR, Nagaraju D, Kolla NK, Santhosi BVSRN. Effective utilization of CuO/water nanofluid potential in the natural circulation loop. *International Journal of Environmental Science and Technology*. 2022;19(5): 3513–3528. doi.org:10.1007/s13762-021-03257-7
- [35] Çobanoğlu N, Karadeniz ZH. Effect of Nanofluid Thermophysical Properties on the Performance Prediction of Single-Phase Natural Circulation Loops. *Energies*. 2020; 13(10): 2523. doi.org:10.3390/en13102523
- [36] Çobanoğlu N, Alaboud M, Karadeniz ZH. Effect of geometrical parameters on the performance of nanofluid-based single phase natural circulation mini loops. *High Temperatures-High Pressures*. 2021; 50(6): 415–36.
- [37] Ho CJ, Chung YN, Lai CM. Thermal performance of Al₂O₃/water nanofluid in a natural circulation loop with a mini-channel heat sink and heat source. *Energy Conversion and Management*. 2014; 87: 848–58. doi.org:10.1016/j.enconman.2014.07.079
- [38] Mohan M, Thomas S, Taha-Tijerina J, Narayanan TN, Sobhan CB, Ajayan PM. Heat transfer studies in thermally conducting and electrically insulating nano-oils in a natural circulation loop. In: *ASME 2013 International Mechanical Engineering Congress and Exposition*. USA. ASME; 2013. V06BT07A040-V06BT07A040. doi.org:10.1115/IMECE2013-64285
- [39] Bocanegra JA, Marchitto A, Misale M. Thermal performance investigation of a mini natural circulation loop for solar PV panel or electronic cooling simulated by lattice Boltzmann method. *International Journal of Energy Production and Management*. 2022; 7(1): 1–12. doi.org:10.2495/EQ-V7-N1-1-12

- [40] Hirano A, Kaga S, Seki K. Cooling Device. Google Patents; 2011.
- [41] Kaga S, Nomura T, Seki K, Hirano A. Development of compact inverter refrigerating system using R600a/CO₂ by Thermo-siphon. Proceedings of the Eighth IIR-Gustav Lorentzen Conference on Natural Working Fluids, Denmark. 2008. 1011–1018.
- [42] He T, Mei C, Longtin JP. Thermosyphon-assisted cooling system for refrigeration applications. *International Journal of Refrigeration*. 2017; 74: 165–176. doi.org:10.1016/j.ijrefrig.2016.10.012
- [43] Sunfrost. Cold Weather Passive Assist Refrigeration [Internet]. [date accessed 28.05.2019]. http://www.sunfrost.com/passive_refrigerator.html
- [44] Garber-Slaght R. Passive Refrigeration [Internet]. Alaska; 2013 [date accessed 15.06.2023]. <http://cchrc.org/media/passiverefrigeration.pdf>
- [45] Omid M, Farhadi M, Jafari M. A comprehensive review on double pipe heat exchangers. *Applied Thermal Engineering*. 2017; 110: 1075–1090. doi.org:10.1016/j.applthermaleng.2016.09.027
- [46] Feldman EE, Hornbeck RW, Osterle JF. A numerical solution of developing temperature for laminar developing flow in eccentric annular ducts. *International Journal of Heat and Mass Transfer*. 1982; 25(2): 243–253. doi.org:10.1016/0017-9310(82)90010-2
- [47] Feldman EE, Hornbeck RW, Osterle JF. A numerical solution of laminar developing flow in eccentric annular ducts. *International Journal of Heat and Mass Transfer*. 1982; 25(2): 231–41. doi.org:10.1016/0017-9310(82)90009-6
- [48] Togun H, Abdulrazzaq T, Kazi S, Badarudin A, Kadhum A, Sadeghinezhad E. A review of studies on forced, natural and mixed heat transfer to fluid and nanofluid flow in an annular passage. *Renewable and Sustainable Energy Reviews*. 2014; 39: 835–56. doi.org:10.1016/j.rser.2014.07.008
- [49] Subramanian R, Kumar AS, Vinayagar K, Muthusamy C. Experimental analyses on heat transfer performance of TiO₂-water nanofluid in double-pipe counter-

- flow heat exchanger for various flow regimes. *Journal of Thermal Analysis and Calorimetry*. 2020; 140: 603-612. doi.org:10.1007/s10973-019-08887-1
- [50] Khanlari A, Yılmaz Aydın D, Sözen A, Gürü M, Variyenli Hİ. Investigation of the influences of kaolin-deionized water nanofluid on the thermal behavior of concentric type heat exchanger. *Heat and Mass Transfer*. 2020; 56(5): 1453–1462. doi.org:10.1007/s00231-019-02764-1
- [51] Arya H, Sarafraz M, Pourmehran O, Arjomandi M. Heat transfer and pressure drop characteristics of MgO nanofluid in a double pipe heat exchanger. *Heat and Mass Transfer*. 2019; 55(6): 1769–1781. doi.org:10.1007/s00231-018-02554-1
- [52] Shahsavari A, Godini A, Sardari PT, Toghraie D, Salehipour H. Impact of variable fluid properties on forced convection of Fe₃O₄/CNT/water hybrid nanofluid in a double-pipe mini-channel heat exchanger. *Journal of Thermal Analysis and Calorimetry*. 2019; 137(3): 1031–1043. doi.org:10.1007/s10973-018-07997-6
- [53] Shahsavari A, Rahimi Z, Salehipour H. Nanoparticle shape effects on thermal-hydraulic performance of boehmite alumina nanofluid in a horizontal double-pipe minichannel heat exchanger. *Heat and Mass Transfer*. 2019; 55(6): 1741–1751. doi.org:10.1007/s00231-018-02558-x
- [54] Jassim EI, Ahmed F. Experimental assessment of Al₂O₃ and Cu nanofluids on the performance and heat leak of double pipe heat exchanger. *Heat and Mass Transfer*. 2020; 56(6): 1845–1858. doi.org:10.1007/s00231-020-02826-9
- [55] Liu S, Sakr M. A comprehensive review on passive heat transfer enhancements in pipe exchangers. *Renewable and Sustainable Energy Reviews*. 2013; 19: 64–81. doi.org:10.1016/j.rser.2012.11.021
- [56] Mousavi Ajarostaghi SS, Zaboli M, Javadi H, Badenes B, Urchueguia JF. A Review of Recent Passive Heat Transfer Enhancement Methods. *Energies*. 2022;15(3):986. doi.org:10.3390/en15030986
- [57] Rashidi S, Hormozi F, Sundén B, Mahian O. Energy saving in thermal energy systems using dimpled surface technology – A review on mechanisms and

- applications. *Applied Energy*. 2019; 250: 1491–1547. doi.org:10.1016/j.apenergy.2019.04.168
- [58] Ting L. Some additional CFD flow field solutions showing the effect of teardrop shaped dimple design on the golf ball aerodynamic performance. *Journal of Visualization*. 2005; 8(1): 4. doi.org:10.1007/BF03181593
- [59] García A, Solano J, Vicente P, Viedma A. The influence of artificial roughness shape on heat transfer enhancement: Corrugated tubes, dimpled tubes and wire coils. *Applied Thermal Engineering*. 2012; 35: 196–201. doi.org:10.1016/j.applthermaleng.2011.10.030
- [60] Li M, Khan TS, Al-Hajri E, Ayub ZH. Single phase heat transfer and pressure drop analysis of a dimpled enhanced tube. *Applied Thermal Engineering*. 2016; 101: 38–46. doi.org:10.1016/j.applthermaleng.2016.03.042
- [61] European Commission. Regulation (EU) No 517/2014 of the European Parliament and of the Council of 16th April 2014 on Fluorinated Greenhouse Gases and Repealing Regulation (EC) No 842/2006. 2014. [date accessed 13.06.2023]. <https://www.eea.europa.eu/policy-documents/regulation-eu-no-517-2014>
- [62] Bolaji BO, Huan Z. Ozone depletion and global warming: Case for the use of natural refrigerant – a review. *Renewable and Sustainable Energy Reviews*. 2013; 18: 49–54. doi.org:10.1016/j.rser.2012.10.008
- [63] Klein SA, Alvarda SF. *Engineering equation solver (EES). F-chart software*, WI. 2007.
- [64] Oruç V, Devocioğlu AG, Ender S. Improvement of energy parameters using R442A and R453A in a refrigeration system operating with R404A. *Applied Thermal Engineering*. 2018; 129: 243–249. doi.org/10.1016/j.applthermaleng.2017.10.035
- [65] ANSYS, Inc. C. *ANSYS CFX-Solver Theory Guide, Release 19.1*. 2019;25-26;39.

- [66] ASHRAE. ASHRAE Handbook: Refrigeration. ASHRAE Publishing House: Atlanta, GA, USA; 2018.
- [67] Banisharif A, Aghajani M, Van Vaerenbergh S, Estellé P, Rashidi A. Thermophysical properties of water ethylene glycol (WEG) mixture-based Fe₃O₄ nanofluids at low concentration and temperature. *Journal of Molecular Liquids*. 2020; 302: 112606. doi.org:10.1016/j.molliq.2020.112606
- [68] Brzóška K, Józwiak B, Golba A, Dzida M, Boncel S. Thermophysical Properties of Nanofluids Composed of Ethylene Glycol and Long Multi-Walled Carbon Nanotubes. *Fluids*. 2020; 5(4): 241. doi.org:10.3390/fluids5040241
- [69] Çengel YA, Cimbala JM. *Fluid Mechanics: Fundamentals and Applications*. 3rd ed. McGraw-Hill; 2013.
- [70] Holcomb GR. A review of the thermal expansion of magnetite. *Materials at High Temperatures*. 2019; 36(3): 232–239. doi.org:10.1080/09603409.2018.1520953
- [71] Muzychka Y, Yovanovich M. Pressure drop in laminar developing flow in noncircular ducts: A scaling and modeling approach. *Journal of Fluids Engineering*. 2009; 131(11): 111105. doi.org:10.1115/1.4000377
- [72] Çobanoğlu N, Karadeniz ZH. Stability And Flow Propagation in Single Phase Natural Circulation mini Loops During The Developing Flow Phase. ULIBTK2021: Proceedings of 23rd Congress on Thermal Science And Technology With International Participation; 2021 Sep 8-10; Gaziantep, Türkiye; 2021. 1777–1785.
- [73] Turgut A, Saglanmak S, Doganay S. Experimental investigation on thermal conductivity and viscosity of nanofluids: particle size effect. *Journal of the Faculty of Engineering and Architecture of Gazi University*. 2016; 31(1): 95–103.
- [74] Anderson JD. *Computational fluid dynamics: the basics with applications*. Science/Engineering/Math McGraw-Hill Science. 1995.

- [75] Boz Z, Erdogdu F, Tutar M. Effects of mesh refinement, time step size and numerical scheme on the computational modeling of temperature evolution during natural-convection heating. *Journal of Food Engineering*. 2014; 123: 8–16. doi.org:10.1016/j.jfoodeng.2013.09.008
- [76] Croy DE, Dougherty DA. *Handbook of Thermal Insulation Applications*. USA; 1983.
- [77] Cheng H, Lei H, Zeng L, Dai C. Experimental investigation of single-phase natural circulation in a mini-loop driven by heating and cooling fluids. *Experimental Thermal and Fluid Science*. 2019; 103: 182–90. doi.org:10.1016/j.expthermflusci.2019.01.003
- [78] Shah R, London A. *Laminar flow forced convection in ducts*. Academic Press; 1978.
- [79] Shah RK. Thermal entry length solutions for the circular tube and parallel plates. In *Proceedings of 3rd national heat and mass transfer conference*; 1975 Dec 11-13, India. HMT 11-75.
- [80] Siegel R, Sparrow E, Hallman T. Steady laminar heat transfer in a circular tube with prescribed wall heat flux. *Applied Scientific Research, Section A*. 1958;7(5):386–92. doi.org:10.1007/BF03184999

Appendix

Appendix A

Publications from the Thesis

Conference Papers

1. Çobanoğlu N, Karadeniz ZH. Stability And Flow Propagation in Single Phase Natural Circulation mini Loops During The Developing Flow Phase. ULIBTK2021: Proceedings of 23rd Congress on Thermal Science And Technology With International Participation; 2021 Sep 8-10; Gaziantep, Türkiye; 2021. 1777–1785.
2. Çobanoğlu N, Karadeniz ZH.). On the Correct Modeling of Flow Characteristics in Double Pipe Heat Exchangers with Inner Dimpled Tube. CONV-22: Proceedings of 5th International Symposium on Convective Heat and Mass Transfer; 2022 June 5-10; İzmir, Türkiye; Begell House:2022. 407-414.

Journal Articles

1. Çobanoğlu N, Koca HD, Genç AM, Karadeniz ZH, Ekren O. Investigation of performance improvement of a household freezer by using natural circulation loop. Science and Technology for the Built Environment. 2021;27(1):85–97. doi.org:10.1080/23744731.2020.1798710
2. Çobanoğlu N, Banisharif A, Estellé P, Karadeniz ZH. The Developing Flow Characteristics of Water - Ethylene Glycol Mixture based Fe₃O₄ Nanofluids in Eccentric Annular Ducts in Low Temperature Applications. International Journal of Thermofluids. 2022; 100149. doi.org:10.1016/j.ijft.2022.100149

Projects

1. Design and Production of Highly Efficient Household Deep Freezer Using a Secondary Cycle with Natural Circulation, TUBİTAK-1505 Project (No: 5180042), Scholar, 01.03.2019 - 01.02.2020.

Curriculum Vitae

Name Surname : Nur Çobanoğlu

Education:

2011–2016 Ege University, Dept. of Mechanical Engineering, B.Sc. Degree

2016–2018 İzmir Kâtip Çelebi University, Dept. of Nanoscience and Nanotechnology, M.Sc. Degree

2018–2023 İzmir Kâtip Çelebi University, Dept. of Mechanical Engineering, Ph.D. Degree

Work Experience:

June 2013-July 2013 Intern - Dirinler Machinery Industry and Commerce Inc.

June 2015-July 2015 Intern - ATAER Energy Electricity Generation Inc.

Aug 2018-Sep 2018 Visiting researcher - ILK Dresden | Institut für Luft- und Kältetechnik gGmbH

Sep 2018 Trainee - Rzeszow University of Technology

Jan 2019-Feb 2019 Visiting researcher - ILK Dresden | Institut für Luft- und Kältetechnik gGmbH

Projects

1. Nanofluids Modeling Strategies Evaluation based on Natural Circulation Mini-Loops, Bilateral Cooperation Project between TÜBİTAK and ARRS (No: 122N346), Scholar, 01.01.2023 - Present.
2. Particulate Matter Levels, Semi-Volatile Organic Matter Content, Toxicity, and Improvability with Mechanical Ventilation in School Indoor Air, TUBİTAK-1001 Project (No: 120R040), Scholar, 02.09.2022 - Present.
3. Design and Production of Highly Efficient Household Deep Freezer Using a Secondary Cycle with Natural Circulation, TUBİTAK-1505 Project (No: 5180042), Scholar, 01.03.2019 - 01.02.2020.

Publications:

International Journal Articles (SCI&SCI-exp.):

1. Bozkır, S. C., **Çobanoğlu, N.**, Doğanay, S., Karadeniz, Z. H., Elçioğlu, E. B., & Turgut, A. (2023). Investigation of external magnetic field effect on the performance of ferrofluid-based single-phase natural circulation loops. *Thermal Science and Engineering Progress*, 42, 101921.
2. **Çobanoğlu, N.**, Genç, A. M., Korkut, S. Ö., Karadeniz, Z. H., & Buschmann, M. H. (2021). Volume-independent contact angle prediction. *High Temperatures-High Pressures*, 50(6), 437–450.
3. **Çobanoğlu, N.**, Alaboud, M., & Karadeniz, Z. H. (2021). Effect of geometrical parameters on the performance of nanofluid-based single phase natural circulation mini loops. *High Temperatures-High Pressures*, 50(6), 415–436.
4. **Çobanoğlu, N.**, Koca, H. D., Genç, A. M., Karadeniz, Z. H., & Ekren, O. (2020). Investigation of performance improvement of a household freezer by using natural circulation loop. *Science and Technology for the Built Environment*, 27(1), 85-97.
5. **Çobanoğlu, N.**, & Karadeniz, Z. H. (2020). Effect of Nanofluid Thermophysical Properties on the Performance Prediction of Single-Phase Natural Circulation Loops. *Energies*, 13(10), 2523.
6. **Çobanoğlu, N.**, Karadeniz, Z. H., Estellé, P., Martínez-Cuenca, R., & Buschmann, M. H. (2019). Prediction of Contact Angle of Nanofluids by Single-Phase Approaches. *Energies*, 12(23), 4558.
7. Hernaiz, M., Alonso, V., Estellé, P., Wu, Z., Sundén, B., Doretto, L., Mancin, S., **Çobanoğlu, N.**, Karadeniz, Z.H., ... & Buschmann, M. H. (2019). The contact angle of nanofluids as thermophysical property. *Journal of colloid and interface science*, 547, 393-406.

Other Journal Articles:

1. **Çobanoğlu, N.**, Karadeniz, Z.H., Sofuoğlu, S.C., & Toksoy, M. (2023). Doğal Havalandırmalı Sınıflarda Sınır Koşulu Tanımının Sayısal Benzetim Sonuçları Üzerine Etkisi. *TTMD Dergisi*, 137, 53-56.

2. **Çobanoğlu, N.**, Banisharif, A., Estellé, P., & Karadeniz, Z. H. (2022). The developing flow characteristics of water- ethylene glycol mixture based Fe₃O₄ nanofluids in eccentric annular ducts in low temperature applications. *International Journal of Thermofluids*, 14, 100149.
3. Aytekin, C. A., Çobanoğlu, C., & **Çobanoğlu, N.** (2021). HESAPLAMALI AKIŞKANLAR DİNAMİĞİ İLE YENİ MEDYA SANATININ BULUŞMASI: DİJİTAL DÖNGÜ. *Uluslararası İletişim ve Sanat Dergisi*, 2, 64–74.

Book Chapters:

1. **Çobanoğlu, N.**, & Karadeniz, Z. H. (2021). Uyku Ortamında İç Çevre Kalitesinin HAD Analizi İle İncelenmesi Üzerine Bir Derleme. In Z. H. Karadeniz & M. Toksoy (Eds.), *İç Çevre Kalitesi ve Uyku* (pp. 62-71). İstanbul: Doğa Yayın.
2. **Çobanoğlu, N.**, Karadeniz, Z. H., Sofuoğlu, S.C. & Toksoy, M (2021). Kaliteli Bir Uyku İçin Havalandırmanın Önemi ve Tasarımı. In Z. H. Karadeniz & M. Toksoy (Eds.), *İç Çevre Kalitesi ve Uyku* (pp. 72-84). İstanbul: Doğa Yayın.
3. **Çobanoğlu, N.**, Karadeniz, Z. H., & Turgut, A. (2019). Nanofluid-Based Single-Phase Natural Circulation Loops. In K. Subramanian, T. Rao, & A. Balakrishnan (Eds.), *Nanofluids and Their Engineering Applications* (pp. 59–76). Florida FL: CRC Press.

International Conference Proceedings:

1. **Çobanoğlu, N.**, and Karadeniz, Z.H. (2022, June). *On the Correct Modeling of Flow Characteristics in Double Pipe Heat Exchangers with Inner Dimpled Tube*. Paper presented at 5th International Symposium on Convective Heat and Mass Transfer (CONV-22), İzmir, Türkiye.
2. Bozkır S.C., **Çobanoğlu N.**, Doğanay S., Karadeniz Z.H., & Turgut A. (2022, June). *The Effect of Permanent Magnet Location on the Performance of Ferrofluid Based SPNCmL*. Paper presented at 5th International Symposium on Convective Heat and Mass Transfer (CONV-22), İzmir, Türkiye.

3. **Çobanoğlu, N.**, Karadeniz, Z.H., Sofuoğlu, S.C., & Toksoy, M. (2022, May). *Importance And Design of Ventilation For An Improved Sleep Quality*. Paper presented at CLIMA 2022 Conference, Rotterdam, The Netherlands.
4. **Çobanoğlu, N.**, Karadeniz, Z.H. (2021, September). *Stability and Flow Propagation In Single Phase Natural Circulation Mini Loops During The Developing Flow Phase*. Paper presented virtually at 23. Congress on Thermal Science and Technology (ULIBTK 2019), Gaziantep, Türkiye.
5. **Çobanoğlu, N.**, Koca, H.D., Genç, A.M., Karadeniz, Z. H., Ekren O. (2019, September). *Doğal Taşınım Döngüsü İle Bir Ev Tipi Dondurucunun Etkinliğinin İyileştirilmesi*. Paper presented at 22. Congress on Thermal Science and Technology (ULIBTK 2019), Kocaeli, Türkiye.
6. **Çobanoğlu, N.**, Karadeniz, Z.H., Turgut A. (2019, May). *Carbon-based Nanofluid Applications in Solar Thermal Energy*. Paper presented at CLIMA 2019, Bucharest, Romania.

National Conference Proceedings:

1. **Çobanoğlu, N.**, Şahin Ç., Karadeniz, Z.H., Sofuoğlu, S.C., & Sofuoğlu, A. (2023, May). *Mekanik Havalandırmalı Sınıflarda Havalandırma Debisinin İç Hava Kalitesi Üzerindeki Etkisinin Sayısal Olarak İncelenmesi*. Paper presented at TESKON2023 Indoor Air Quality Symposium, İzmir, Türkiye.

International Conference Abstracts and Extended Abstracts:

1. **Çobanoğlu, N.**, Banisharif A., Estellé, P., Karadeniz, Z.H. (2021, October). *The Developing Natural Convection Visualization of Water - Ethylene Glycol Mixture based Fe₃O₄ Nanofluids in Eccentric Annular Ducts in Low Temperature Applications*. Paper presented virtually at NANOBOSTON Conference 2021, Boston, MA, USA.
2. Bozkır, S. C., Turgut A., Doğanay, S., **Çobanoğlu, N.**, Karadeniz, Z.H. (2021, September). *Multiphysical Modelling of a Ferrofluid Based Single – Phase Natural Circulation Mini Loop*. Paper presented virtually at THERMAM2021, Rostock, Germany.
3. Aytekin, C. A., Çobanoğlu, C., **Çobanoğlu, N.** (2021, September). *Hesaplmalı Akışkanlar Dinamiği İle Yeni Medya Sanatının Buluşması: Dijital*

- Döngü*. Paper presented virtually at The International Communication and Art Symposium (ILSANS), Online.
4. **Çobanoğlu, N.**, Karadeniz, Z. H. (2020, September). *Developing flow characteristics of nanofluid based single phase natural circulation mini loop*. Paper presented virtually at THERMAM2020, Rostock, Germany.
 5. **Çobanoğlu, N.**, Alaboud, M., Karadeniz, Z. H. (2019, September). *On the Validity of Mass Flow Rate Equation for Nanofluid Based Single Phase Natural Circulation Mini Loops*. Paper presented at 6th Int. Conf.: Thermophysical and Mechanical Properties of Advanced Materials (THERMAM) & 8th Rostocker Int. Conf.: Thermophysical Properties for Technical Thermodynamics, İzmir, Türkiye.
 6. **Çobanoğlu, N.**, Genç, A.M., Korkut Uysal, S.Ö., Karadeniz, Z. H., Buschmann, M.H. (2019, September). *Theoretical Prediction of the Contact Angle Independent from the Volume Effect*. Paper presented at 6th Int. Conf.: Thermophysical and Mechanical Properties of Advanced Materials (THERMAM) & 8th Rostocker Int. Conf.: Thermophysical Properties for Technical Thermodynamics, İzmir, Türkiye.
 7. Koca, H.D., **Çobanoğlu, N.**, Genç, A.M., Karadeniz, Z. H., Ekren O. (2019, September). *Recent Technologies on Refrigeration Systems: a Novel Design to Enhance the Performance of the Vapor Compression System*. Poster presented at 6th Int. Conf.: Thermophysical and Mechanical Properties of Advanced Materials (THERMAM) & 8th Rostocker Int. Conf.: Thermophysical Properties for Technical Thermodynamics, İzmir, Türkiye.
 8. **Çobanoğlu, N.**, Karadeniz, Z.H., Estellé, P., Martínez-Cuenca, R., Buschmann, M.H. (2019, June). *On the Contact Angle of Nanofluids*. Paper presented at 1st International Conference on Nanofluids (ICNf2019) & 2nd European Symposium on Nanofluids (ESNf2019), Castellon, Spain.
 9. **Çobanoğlu, N.**, Karadeniz, Z.H., Turgut A. (2018, May). *Wettability of Nanofluids*. Paper presented at 4th Working Group Meetings, Workshop on Nanofluids in Energy Systems, Strategic Workshop: Naples, Italy.
 10. **Çobanoğlu, N.**, Kolkıran, A. (2018, May). *A Double-Laser-Trap Custom Designed Optical Tweezer*. Poster session presented at the 1st Light and Light-based Technologies Workshop, Ankara, Turkey.

International Conference Presentations:

1. **Çobanoğlu, N.**, Karadeniz, Z.H., Sofuoğlu, S.C., & Toksoy, M. (2022, September). *Numerical Investigation on The Airborne Transmission in Naturally Ventilated Classrooms: Effect of Boundary Conditions*. Paper presented at XV INTERNATIONAL HVAC&R TECHNOLOGIES SYMPOSIUM 2022, Online.
2. **Çobanoğlu, N.**, Banisharif A., Estellé, P., Karadeniz, Z.H. (2021, September). *The Developing Flow Characteristics of Water - Ethylene Glycol Mixture based Fe₃O₄ Nanofluids in Eccentric Annular Ducts in Low Temperature Applications*. Paper presented virtually at 3rd European Symposium on Nanofluids, Iasi, Romania.
3. Bozkır, S. C., **Çobanoğlu, N.**, Doğanay, S., Karadeniz, Z.H., Turgut A. (2021, September). *The Numerical Investigation on Natural Convection Effects in Single-Phase Natural Circulation Mini Loops*. Paper presented virtually at 3rd European Symposium on Nanofluids, Iasi, Romania.
4. **Çobanoğlu, N.**, Koca, H.D., Ekren O., Karadeniz, Z. H. (2021, May). *A New Type of Suction Line Heat Exchangers in Household Freezer: Natural Circulation Loops*. Paper presented virtually at 10th Mediterranean Congress of Climatization, Lisbon, Portugal.

International Collaborations:

2020-2023 TUBITAK BİDEB 2211/A National PhD Scholarship Program

2019-2023 YÖK 100/2000 PhD Scholarship Program

International Collaborations:

2018-2020 COST Action CA15119: Nanouptake - Overcoming Barriers to Nanofluids Market Uptake

2020-2021 COST CIG NANOConVEX IG15119.